

TRANSITION METAL AND NITROGEN CO-DOPED GRAPHDIYNE
AS A CATHODE MATERIAL OF LITHIUM-SULFUR
BATTERIES: A FIRST-PRINCIPLES STUDY



A Thesis Submitted in Partial Fulfillment of the Requirements for the
Degree of Master of Science in Physics
Suranaree University of Technology
Academic Year 2022

โลหะทรานซิชันและไนโตรเจนร่วมเจือปนวัสดุกราฟไดอายนน์
เพื่อเป็นวัสดุแคโทดในลิเทียม-ซัลเฟอร์แบตเตอรี่
การศึกษาโดยวิธีเฟิร์สพริ้นซิเพิล



นายศิริศักดิ์ สิงห์เสน

วิทยานิพนธ์นี้เป็นส่วนหนึ่งของการศึกษาตามหลักสูตรปริญญาวิทยาศาสตรมหาบัณฑิต
สาขาวิชาฟิสิกส์
มหาวิทยาลัยเทคโนโลยีสุรนารี
ปีการศึกษา 2565

**TRANSITION METAL AND NITROGEN CO-DOPED GRAPHDIYNE
AS A CATHODE MATERIAL OF LITHIUM-SULFUR
BATTERIES: A FIRST-PRINCIPLES STUDY**

Suranaree University of Technology has approved this thesis submitted in partial fulfillment of the requirements for a Master's Degree.

Thesis Examining Committee



(Assoc. Prof. Dr. Panomsak Meemon)

Chairperson



(Asst. Prof. Dr. Suwit Suthirakun)

Member (Thesis Advisor)



(Dr. Ittipon Fongkaew)

Member (Thesis Co-Advisor)



(Assoc. Prof. Dr. Sirichok Jungthawan)

Member



(Dr. Anchalee Junkaew)

Member



(Prof. Dr. Santi Maensiri)

Dean of the Institute of Science



(Assoc. Prof. Dr. Chatchai Jothityangkoon)

Vice-Rector for Academic Affairs

and Quality Assurance

ศิริศักดิ์ สิงห์เสน : โลหะทรานซิชันและไนโตรเจนร่วมเจือปนวัสดุกราฟไดอาซีนเพื่อเป็นวัสดุแคโทดในลิเทียม-ซัลเฟอร์แบตเตอรี่ การศึกษาโดยวิธีเฟิร์สพริન્ซิเพิล (TRANSITION METAL AND NITROGEN CO-DOPED GRAPHDIYNE AS A CATHODE MATERIAL OF LITHIUM-SULFUR BATTERIES: A FIRST-PRINCIPLES STUDY)

อาจารย์ที่ปรึกษา : ผู้ช่วยศาสตราจารย์ ดร.สุวิทย์ สุธีรากุล, 113 หน้า.

คำสำคัญ: ลิเทียม-ซัลเฟอร์แบตเตอรี่ กราฟไดอาซีน ทฤษฎีฟังก์ชันนอลความหนาแน่น เฟิร์สพริન્ซิเพิล ลิเทียมพอลิซัลไฟด์

วิทยานิพนธ์นี้ใช้การคำนวณบนพื้นฐานด้วยระเบียบวิธีฟังก์ชันนอลความหนาแน่น และการจำลองพลศาสตร์เชิงควอนตัม เพื่อศึกษาบทบาทของโลหะทรานซิชันและไนโตรเจนอะตอมร่วมเจือปนวัสดุกราฟไดอาซีน เพื่อเป็นวัสดุแคโทดสำหรับลิเทียม-ซัลเฟอร์แบตเตอรี่ โดยพิจารณาสมบัติที่สำคัญ ได้แก่ การก่อเกิดของการเจือ ความสามารถในการดูดซับ สมบัติเชิงอิเล็กทรอนิกส์ การลดผลกระทบชัลเทิล (Shuttle effect) ความสามารถในการละลาย และการย่อยสลายของโมเลกุล จากผลการคำนวณแสดงให้เห็นว่ากราฟไดอาซีนที่เจือโลหะทรานซิชันร่วมกับไนโตรเจนเป็นสารตัวนำไฟฟ้า ที่มีความเสถียรเชิงอุณหพลศาสตร์ ซึ่งสนับสนุนการเกิดของปฏิกิริยาระหว่างการอัดและการคายประจุได้ การดูดซับของโมเลกุลซัลเฟอร์และลิเทียมพอลิซัลไฟด์บนกราฟไดอาซีนเป็นแรงวนเตอร์วาลส์อย่างอ่อน ก่อให้เกิดผลกระทบชัลเทิลได้ ในขณะที่การดูดซับของโมเลกุลดังกล่าวบนแผ่นเจือปนเป็นการดูดซับทางเคมีที่แข็งแรง ซึ่งช่วยลดการเกิดผลกระทบชัลเทิลได้เป็นอย่างดี เพราะมีแรงดูดซับระหว่างโมเลกุลกับแผ่นมากกว่าแรงดึงดูดกับโมเลกุลอิเล็กโทรไลต์ โดยโมเลกุลพอลิซัลไฟต์ในสายละลายอิเล็กโทรไลต์มีความสามารถในการละลายสูง โดยเฉพาะในสารละลายไดเมทอกซีอีเทน (Dimethoxy ethane) นอกจากนี้การสลายตัวของโมเลกุลพอลิซัลไฟต์บนแผ่นเจือปนเกิดขึ้นได้ดีกว่าบนแผ่นกราฟไดอาซีนบริสุทธิ์ โดยการลดลงของพลังงานก่อกัมมันต์ ส่งผลให้สนับสนุนการเร่งปฏิกิริยารีดอกซ์ในกระบวนการอัดและคายประจุ ดังนั้น วิทยานิพนธ์ฉบับนี้อาจพูดเป็นนัยได้ว่าโลหะทรานซิชันและไนโตรเจนอะตอมร่วมเจือปนวัสดุกราฟไดอาซีนเหมาะสมสำหรับประยุกต์ใช้เพื่อเป็นวัสดุแคโทดชนิดใหม่ในลิเทียม-ซัลเฟอร์แบตเตอรี่

สาขาวิชาฟิสิกส์
ปีการศึกษา 2565

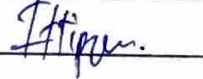
ลายมือชื่อนักศึกษา ศิริศักดิ์
ลายมือชื่ออาจารย์ที่ปรึกษา สุวิทย์ สุธีรากุล
ลายมือชื่ออาจารย์ที่ปรึกษาร่วม พริมา

SIRISAK SINGSEN : TRANSITION METAL AND NITROGEN CO-DOPED GRAPHDIYNE
AS A CATHODE MATERIAL OF LITHIUM-SULFUR BATTERIES : A FIRST-PRINCIPLES
STUDY. THESIS ADVISOR : ASST. PROF. SUWIT SUTHIRAKUN, Ph.D. 113 PP.

Keywords: lithium-sulfur batteries, graphdiyne material, density functional theory, first principles method, polysulfide

In this thesis, we carried out first-principles calculations to study the synergetic role of a transition metal and N co-doped graphdiyne ($TMN_x@GDY$, $TM = Fe$ or Co) as a host cathode material in lithium-sulfur (Li-S) batteries. The fundamental properties were explored, including the formation of doping, adsorbability, electronic properties, suppression and solvation of lithium polysulfide (Li_2S_x), and catalytic Li_2S_x decomposition. Our computations reveal that a doped substrate is thermodynamically stable. Their metallic structures promote redox activities during the charge/discharge process. The adsorption strengths between S_8/Li_2S_x molecules and pristine GDY are weak as Van der Waals interactions, leading to Li_2S_x shuttling easily. The adsorbability is substantially improved upon adsorption on the doped substrates where the molecules prefer to form $TM-S$ and $Li-N$ bonding. Moreover, the adsorption strength between Li_2S_x and the doped substrates is stronger than the binding interaction toward electrolyte molecules, suggesting a good suppression of the shuttle effect. The Li_2S_x molecules show high solubility in the presence of an electrolyte environment, especially DME solvent, leading to promote Li_2S_x dissolution. In addition, the energy barriers of the Li_2S_x decomposition on the doped substrates are reduced when compared to those on pristine GDY, resulting in accelerated phase transformation. Our thesis may suggest that the doped substrate is a promising candidate as a novel host cathode material in Li-S batteries.

School of Physics
Academic Year 2022

Student's Signature 
Advisor's Signature 
Co-Advisor's Signature 

ACKNOWLEDGEMENTS

I would like to express appreciation to my thesis advisor Asst. Prof. Dr. Suwit Suthirakun, Dr. Pussana Hirunsit, and co-advisor Dr. Ittipon Fongkaew for their patience, kind support, guidance, discussion, and encouragement throughout my thesis. I would like to acknowledge Assoc. Prof. Dr. Panomsak Meemon, Assoc. Prof. Dr. Sirichok Jungthawan, and Dr. Anchalee Junkaew contributed to the thesis-examining committees. I would like to thank the Development and Promotion of Science and Technology Talents Project (DPST, THAILAND) for the scholarship during my master's degree program. This research and innovation activity is funded by the National Research Council of Thailand (NRCT) and Suranaree University of Technology (SUT) for financial support. I acknowledge the NSTDA Supercomputer Center (ThaiSC) and Institute of Science, Suranaree University of Technology, for computational resources. I thank people from the School of Physics, Institute of Science, Suranaree University of Technology, for their guidance and friendship. I appreciate Lappawat Ngamwongwan and Apinya Ngoipala for their valuable time in teaching and suggesting computational techniques. I am also grateful to my friends in Computational Materials Science and Catalysis (COMSCAT) Group for their assistance and friendship. Finally, I would like to express thanks to my family and my girlfriend for their love, kind support, and encouragement.

Sirisak Singsen

CONTENTS

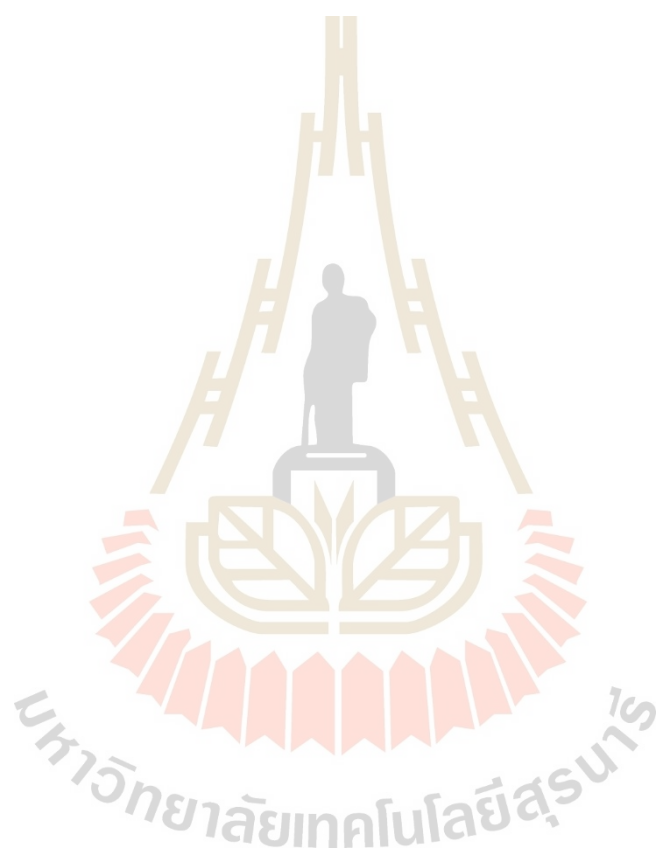
	Page
ABSTRACT IN THAI.....	I
ABSTRACT IN ENGLISH.....	II
ACKNOWLEDGEMENTS	III
CONTENTS.....	IV
LIST OF TABLES	VII
LIST OF FIGURES	VIII
LIST OF ABBREVIATIONS	XII
CHAPTER	
I INTRODUCTION.....	1
1.1 Lithium-sulfur (Li-S) batteries and cathode materials.....	1
1.2 Two-dimensional graphdiyne (GDY) material	4
1.3 Transition metal and nitrogen co-doping.....	8
1.4 Research objectives	11
1.5 Scope and limitations.....	12
1.6 References	13
II FIRST-PRINCIPLES METHODS	19
2.1 Many-body Schrödinger equation.....	19
2.2 Hartree-Fock approximation.....	21
2.3 Density functional theory	22
2.3.1 Electron density.....	23
2.3.2 The Hohenberg-Kohn theorems.....	23
2.3.3 The Kohn-Sham equation.....	23
2.3.4 Exchange-correlation functional.....	25
2.3.5 Wavefunction and pseudopotential.....	26
2.3.6 Self-Consistent Field approach.....	28
2.4 Climbing image nudged elastic band (CI-NEB) method.....	30

CONTENTS (Continued)

		Page
2.5	Ab initio molecular dynamic simulation.....	30
2.5.1	Born-Oppenheimer molecular dynamics (BOMD).....	30
2.5.2	Car-Parinello molecular dynamics (CPMD).....	31
2.6	Summary of computational details.....	33
2.7	References	33
III	STRUCTURAL AND ELECTRONIC PROPERTIES.....	36
3.1	Pristine graphdiyne monolayer.....	36
3.1.1	Geometric structure	36
3.1.2	Electronic properties	37
3.2	Transition metal and nitrogen co-doped graphdiyne.....	39
3.1.1	Geometric structure	39
3.1.2	Electronic properties	42
3.3	References	44
IV	ADSORPTIVITY AND SUPPRESSION OF POLYSULFIDE SHUTTLING	46
4.1	Sulfur and lithium polysulfide molecules.....	46
4.2	Adsorptivity on pristine and doped substrates.....	48
4.3	Electronic properties upon adsorption.....	54
4.4	Suppression of shuttle effect	56
4.5	References.....	62
V	SOLUBILITY AND DISSOCIATION OF POLYSULFIDES	65
5.1	Solubility of the soluble LiPS in an electrolyte solution.....	65
5.2	Dissociation and diffusion of Li ions on LiPS	69
5.3	Reference	75
VI	CONCLUSIONS.....	77
	APPENDICES.....	79
	APPENDIX A THE DOS WITH DFT+U AND BADER CHARGE DIFFERENCE.....	80

CONTENTS (Continued)

	Page
APPENDIX B PUBLICATION AND PRESENTATIONS	82
CURRICULUM VITAE.....	97



LIST OF TABLES

Table	Page
3.1	Formation energy (E_f), Adsorption energy of M atom (E_{ads}), a bond distance of M-C bond (L_{M-C}), a bond distance of M-N bond (L_{M-N}), charge transfer (Q_M) of M atom to N-GDY..... 41
4.1	Geometric parameters of optimized LiPS species 47
4.2	Geometric parameters of S_8 and LiPS after adsorption on $MN_2@GDY$ 52
A.1	The Bader charge distribution after adsorption..... 81



LIST OF FIGURES

Figure		Page
1.1	(a) The general geometry of Li-S cell with its charge/discharge process. (b) Voltage profiles of Li-S cell.....	3
1.2	Summary of the effect on electrodes, including the lithium polysulfide shuttle, polysulfide dissolution, and insoluble phase SEI formation on the anode side.....	4
1.3	(a) chemical Lewis's structure of graphdiyne (GDY). (b) Full atomistic model of GDY depicting the triangular pore	6
1.4	(a) The schematic of the preparation process of sulfide graphdiyne (SGDY). (b) SEM image of GDY. (c) TEM image of GDY. (d) HRTEM of GDY. (e) HRTEM image of GDY. (f) SEM image SGDY. (g) TEM image of SGDY. (h) SEM image of SGDY. (i) TEM image of SGDY. (j) TEM image of SGDY. (k) HRTEM image of SGDY	7
1.5	(a) The 2 nd and 3 rd charge/discharge of SGDY cathode at 0.1 C (1 C = 1672 mA g ⁻¹). (b) CV curve at a scan rate of 0.1 mV s ⁻¹ . (c) Rate performance. (d) Cycling performance of SGDY cathode at current densities of 0.5 and 1 C.....	8
1.6	(a) HAADF-STEM image of Co-N doped graphene. (b) CV of symmetric cell with Co and N doping, N doping, and Co doping on graphene for Li-S battery. (c) Evolution of the intensities of peak B and peak D. (d) Energy profiles for LiPS on N-doped and Co-N-doped graphene.....	10
1.7	Schematic illustration of the synthetic procedure of (a) Co-N doped GDY and (b) Fe-N doped GDY from experimental views	11
2.1	Schematic of the pseudo wavefunction and the corresponding potential compared with those of all electron wavefunctions and their potential.....	28

LIST OF FIGURES (Continued)

Figure	Page
2.2	The scheme of self-consistency iteration for solving the Kohn-Sham equation and obtaining the calculated total energy and other properties 29
3.1	Geometric structure of 2 × 2 GDY supercell with its lattice constant and C-C bond distances 37
3.2	(a) Projected density of state (PDOS) of pristine GDY and (b) corresponding electronic band structure..... 38
3.3	The possible configuration of the transition metal and nitrogen co-doped GDY. Note that the corresponding formation energy of each configuration is shown in parentheses. C, N, Co, and Fe atoms are represented by brown, grey, blue, and gold, respectively 40
3.4	The variation of total energy as a function of time along the AIMD simulation at 300 K and corresponding initial and final configurations of CoN ₂ @GDY and (b) FeN ₂ @GDY 42
3.5	Geometric structure of (a) CoN ₂ @GDY and (b) FeN ₂ @GDY. (c-d) the corresponding projected density of state (PDOS) and band structures of (a) CoN ₂ @GDY and (b) FeN ₂ @GDY, respectively. Color code: brown; C, white; N, blue; Co, and yellow; Fe 43
3.6	The Bader charge distribution of CoN ₂ @GDY and FeN ₂ @GDY..... 44
4.1	The relaxed molecular structures of S ₈ and LiPS species. Li and S atoms are represented by green and yellow spheres, respectively 48
4.2	Correlation between S ₈ /LiPSs adsorption energy and degree of charge transfer to substrate. The adsorbate species are represented as a color gradient where these adsorbates are adsorbed on pristine GDY (green color), CoN ₂ @GDY (blue color), and FeN ₂ @GDY (orange color) 49
4.3	Top and side views of the most stable adsorption configurations of S ₈ and LiPSs on (a) pristine GDY, (b) CoN ₂ @GDY, (c) FeN ₂ @GDY. Brown, C; light blue, N; yellow, S; green, Li; blue, Co; gold, Fe. Charges of each Li atom,

LIST OF FIGURES (Continued)

Figure	Page
<p>all S atoms and the substrate are labeled in green, yellow, and brown numbers, respectively.....</p>	51
<p>4.4 Projected density of state (PDOS) of S_8/LiPSs adsorption on (a) pristine (a) pristine GDY, (b) $CoN_2@GDY$, and (c) $FeN_2@GDY$. The Fermi level (E_F) is adjusted to 0 eV</p>	55
<p>4.5 Bader charge distribution upon adsorption (left panel) and corresponding partial density of state (right panel) of Li and N for (a) Li_2S_8 and (b) Li_2S adsorbed $CoN_2@GDY$, and (c) Li_2S_8 and (d) Li_2S adsorbed $FeN_2@GDY$</p>	56
<p>4.6 The co-adsorption configurations of 1 to 4 DME(s)/DOL(s) in the system of Li_2S_6 adsorbed on (a) GDY, (b) $CoN_2@GDY$, and (c) $FeN_2@GDY$. Color code: gray, GDY; brown, C; light blue, N; yellow, S; green, Li; white, H; blue, Co; gold, Fe; red, O</p>	58
<p>4.7 Schematic illustration of a) the computations of adsorption energy ($E_{ads, single}$) and binding energy ($E_{b, single}$), b) the comparison between $E_{ads, single}$ and $E_{b, single}$ to predict the suppression of shuttle effect and dissolution of LiPS. Co-adsorbed configuration of Li_2S_6 on $CoN_2@GDY$ in the presence of (c) DME or (d) DOL molecules. The labeled distances identify the vertical distance from the substrate to the topmost of the electrolyte molecules. Gray, GDY; brown, C; light blue, N; yellow, S; green, Li; white, H; blue, Co; gold, Fe; red, O.....</p>	61
<p>4.8 The difference in binding energies between Li_2S_6 and DME molecule(s) in the co-adsorption systems of $CoN_2@GDY$ (blue line) and $FeN_2@GDY$ (brown line)</p>	62
<p>5.1 Low-energy configurations of a-c) DME- and d-f) DOL-solvated LiPSs obtained from AIMD simulations. Illustrations in the ball-and-stick model represent electrolyte molecules in the first solvation shell, whereas the wireframe models are the outer solvation shell.....</p>	67

LIST OF FIGURES (Continued)

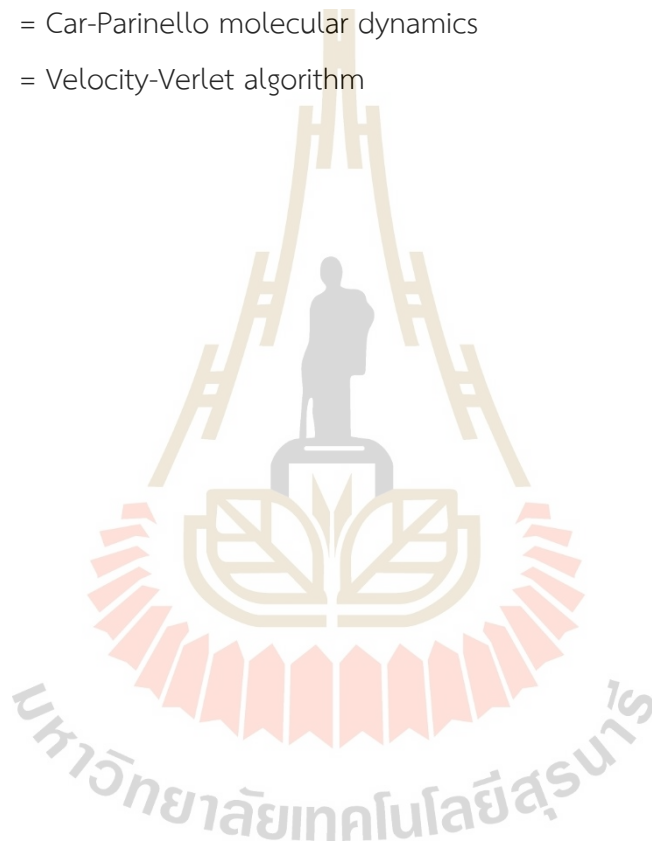
Figure	Page
5.2	The corresponding radial distribution functions (RDFs) of Li and S bonding to elements on electrolyte molecules in (c) DME and (d) DOL systems. (g) their corresponding solvation energies 68
5.3	Potential energy profiles of (a) Li_2S_2 and (b) Li_2S decompositions on GDY (green line), $\text{CoN}_2@GDY$ (blue line), and $\text{FeN}_2@GDY$ (yellow line), and their corresponding intermediates for (c) Li_2S_2 and (d) Li_2S decompositions. The labeled numbers at the intermediate states indicate their relative energies, whereas the numbers in parentheses denote the energy barriers..... 72
5.4	Top and side views for dissociation of Li-S bond of Li_2S_2 on (a) $\text{CoN}_2@GDY$ and (b) $\text{FeN}_2@GDY$. These configurations are the same as site B in Figure 5.3c. Brown, C; light blue, N; yellow, S; green, Li; blue, Co; gold, Fe 73
5.5	Another reaction path of catalytic decomposition of (a) Li_2S_2 and (b) Li_2S , and corresponding energy profile of (c) Li_2S_2 and (d) Li_2S , respectively, on $\text{CoN}_2@GDY$ (blue line) and $\text{FeN}_2@GDY$. Color code: gray, C; light blue, N; yellow, S; green, Li; blue, Co; gold, Fe 74
5.6	Diffusion of Li-ion along the path a (red dash line) and path b (blue dash line), left panel. The corresponding energy profile along path a (red solid line) and path b (solid blue line), right panel. Color code: brown, C; green, Li 75

LIST OF ABBREVIATIONS

Li-S	= Lithium-sulfur
EV	= Electric vehicle
LiPS	= Lithium polysulfide
GDY	= Graphdiyne
SGDY	= Sulfur graphdiyne
CV	= Current-voltage
D	= Dimension
HAADF	= High-angle annular dark-field
STEM	= scanning transmission electron microscopy
ORR	= Oxygen reduction reaction
HER	= Hydrogen evolution reaction
DFT	= Density functional theory
AIMD	= Ab-initio molecular dynamics
VASP	= Vienna ab initio simulation package
GGA	= Generalized gradient approximation
PDOS	= Projected density of states
XPS	= X-ray photoelectron spectra
LDA	= Local density approximation
PAW	= Projector-augmented wave
PBE	= Perdew-Burke-Ernzerhof
CI-NEB	= Climbing image-nudged elastic band
MEP	= Minimum energy pathway
MEP	= Minimum energy path
TS	= Transition state
XC	= Exchange-correlation
PP	= Pseudopotential
TMN _x @GDY	= Transition metal and nitrogen co-doped graphdiyne

LIST OF ABBREVIATIONS (Continued)

VBM	= Valence band maximum
CBM	= Conduction band minimum
NEB	= Nudged elastic band
BOMD	= Born-Oppenheimer molecular dynamics
CMD	= classical molecular dynamics
CPMD	= Car-Parinello molecular dynamics
VVA	= Velocity-Verlet algorithm



CHAPTER I

INTRODUCTION

1.1 Lithium-sulfur (Li-S) batteries and cathode materials

Nowadays, energy consumption has substantially increased due to the demand for human activities, such as agriculture, logistic transportation, industries, and communications (Boundy, 2019; Bradford, 2018; Kutscher *et al.*, 2018). However, energy production is a critical problem because of low productivity and poor reusability. Developing energy storage technologies has been challenging to improve the lack of energy and enhance energy capacity. Various solid-state chemistries are commercially used to store electric power, including fuel cells (Smith, 2000), pumped hydroelectricity (Lu *et al.*, 2017), capacitors (Hall *et al.*, 2010), flywheel (Faraji *et al.*, 2017), and batteries (C. Zhang *et al.*, 2018). Among them, the battery cells are applied as an electric device for large-scale utilization because they are lightweight, more stable, and have a higher capacity than other chemistries. In addition, rechargeable batteries are widely used for several applications such as hybrid-electric vehicles (EVs), portable electronic devices, power plants, and mobile phones (Liang *et al.*, 2019; Placke *et al.*, 2017), which they can be reusable and sustainable, leading to saving budget and fast re-productivity.

Regarding rechargeable batteries, lithium-ion (Li-ion) batteries have attracted attention for the past decades (Armand *et al.*, 2008; Whittingham, 1976). These batteries show remarkable potential with high energy capacity and power densities. However, further development of Li-ion batteries is restricted due to the ability and engineering-designed limitations (Goodenough *et al.*, 2013). Various emerging alternative energy storage is currently proposed for next-generation battery systems to substitute the conventional Li-ion cells, such as sodium-ion (Na-ion) batteries (Ni *et al.*, 2017), sodium-sulfur (Na-S) batteries (Wang *et al.*, 2017), Na-air batteries (Khan *et al.*, 2020), lithium-air batteries (Aurbach *et al.*, 2016), and vanadium redox batteries (He *et al.*, 2022). Nevertheless, most of them are still under development

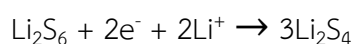
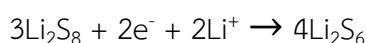
because some critical battery issues have not been improved. Thus, a comprehensive understanding of the behaviors and phenomena in the battery cell is significant for further developing and obtaining better battery performance for the commercial community.

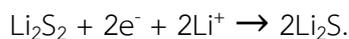
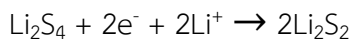
Rechargeable Li-S batteries have been one of the promising next-generation energy storage for a decade (X. Liu *et al.*, 2018). The theoretical specific capacity and energy density are as high as 2600 Wh kg⁻¹ and 1672 mA h g⁻¹, respectively (Ji *et al.*, 2009; Yin *et al.*, 2013). Such potentials are higher than those of other commercial batteries, including Ni-H batteries (80 Wh kg⁻¹, 100 mA h g⁻¹), Zn-air batteries (1086 Wh kg⁻¹, 820 mA h g⁻¹), and Li-ion batteries (387 Wh kg⁻¹, 155 mA h g⁻¹) (Barghamadi *et al.*, 2013; Ma *et al.*, 2015). Moreover, sulfur material as the component of the cathode side is commonly found in natural resources with its environmentally friendly, leading to low cost and non-toxicity (Canfield, 2001). A lithium-metal anode is also lightweight, with a highly negative redox potential of -3.04 V vs. standard hydrogen electrode (SHE). These advantages bring Li-S batteries to stand out, attracting most of the attention as a new promising battery in the future.

Li-S batteries are electrochemical cell with high gravimetric energy. The redox mechanism involves the reaction between lithium ions (Li⁺) and sulfur molecules (S₈), where S₈ is an allotrope of sulfur crystals with the highest stability in nature. The schematic diagram and corresponding voltage profiles of the Li-S cell are shown in Figure 1.1. The complete redox reaction is shown in following



where Li₂S is lithium sulfide molecules as the final product during the discharge process. The reduction reaction involves Li⁺ extracted from the lithium metal anode to diffuse through an electrolyte solvent to react with S₈ on the cathode side. The complex forms of this interaction are lithium polysulfide (LiPS) with an empirical form of Li₂S_x where x = 1, 2, 4, 6, and 8. The elementary reactions of this reduction mechanism can be shown below (Barchasz *et al.*, 2012; Moy *et al.*, 2014),





The physical properties of LiPS species are basically separated into two groups regarding their molecular size, including the long-chain LiPSs (Li_2S_8 , Li_2S_6 , and Li_2S_4) and the short-chain LiPSs (Li_2S_2 and Li_2S). The long-chain molecules possess high solubility in an electrolyte solvent and high conductivity, whereas the short-chain molecules show a solid phase with high resistivity and low solubility (Mikhaylik *et al.*, 2004).

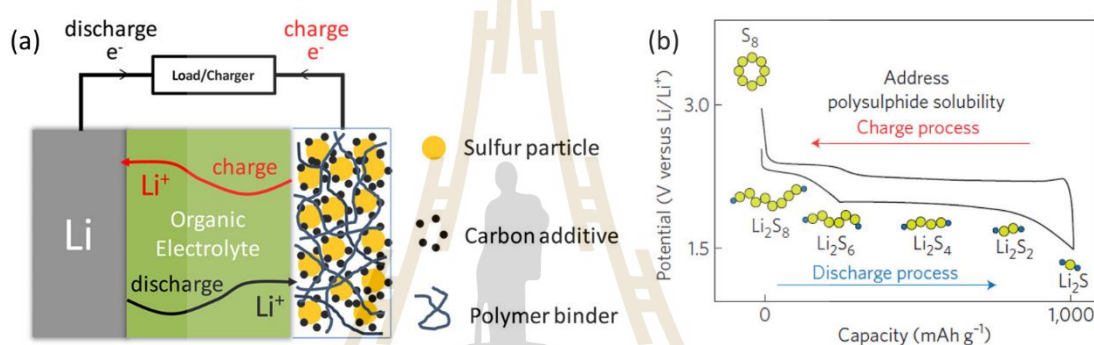


Figure 1.1 (a) The general geometry of Li-S cell with its charge/discharge process. (b) Voltage profiles of Li-S cells (Manthiram *et al.*, 2014).

The significant problems in Li-S batteries consist of low Coulombic efficiency, short-term cycle utilization, and sluggish redox reactions, as shown in Figure 1.2 (Wild *et al.*, 2015). When long-chain LiPSs (Li_2S_8 , Li_2S_6 , and Li_2S_4) dissolve in a solvent, they can diffuse to move nearby the electron-rich lithium anode surface with the help of gradient concentration and an internal electric field between electrodes. This phenomenon of polysulfide transport is called the “Shuttle effect.” Such soluble molecules can react with lithium atoms at the surface, receiving additional electrons directly, to undergo the decomposition reactions to form smaller LiPSs (Li_2S_2 and Li_2S), leading to the growth of Li_2S film formation at the anode surface, resulting in low Coulombic efficiency (Bresser *et al.*, 2013; Huang *et al.*, 2015; Mikhaylik *et al.*, 2004). For the cathode side, the Li_2S phase provides high-volume expansion within the electrode. This may cause the battery to swell. The electronic resistivity of Li_2S is higher than 10^{14} ohm-m, resulting in the problematic Li-ion diffusion with a low

diffusivity of $10^{-15} \text{ cm}^2 \text{ s}^{-1}$. It leads to an increase the internal resistance and prohibits further redox reactions. During the change process, the Li_2S conversion requires enormous activation energy to overcome an energy barrier for phase transformation with sluggish redox activities (Assary *et al.*, 2014). Another problem is also presented on the anode side, such as lithium dendrite, which can destroy a separator, leading to a short circuit (Pang *et al.*, 2018). These critical problems inhibit Li-S batteries to exposes to commercialization. Therefore, several research has attempted to improve these issuers by searching for a novel promising host cathode material for Li-S batteries.

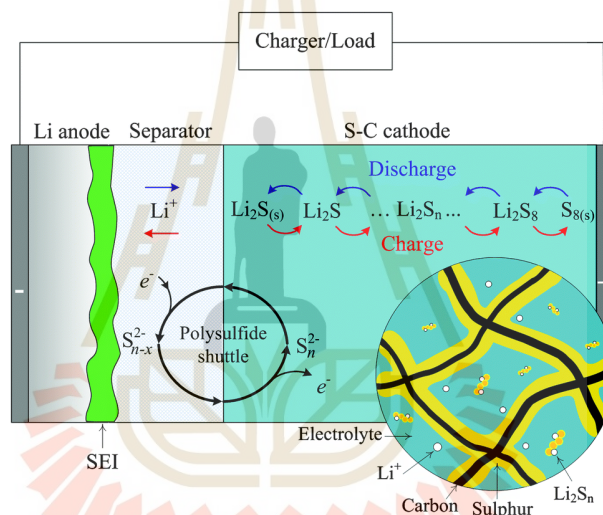


Figure 1.2 Summary of the effect on electrodes, including the lithium polysulfide shuttle, polysulfide dissolution, and insoluble phase SEI formation on the anode side (Wild *et al.*, 2015).

1.2 Two-dimensional graphdiyne (GDY) material

A suitable cathode material can improve to suppress the LiPSs shuttling and promote phase transformation. One of the essential features of host cathode materials is a good conductor because the sulfur material (S_8) is an insulator with poor electron accessibility on the cathode side, which a host cathode can be able to distribute electrons to S_8 for the redox activities (Eftekhari *et al.*, 2017). Furthermore, the preliminary properties of cathode material should have at least three features (Eftekhari *et al.*, 2017): (i) high surface area for the accommodation of sulfur

molecules and good electronic mobility, (ii) high chemical interaction of S_8 and the products of LiPSs, which is able to confine the LiPSs within the cathode to suppress the shuttle effect, and (iii) good catalytic material to help the acceleration of the redox reaction during charge and discharge process. According to this consideration, there are several promising host cathode materials for this battery, including carbon nanomaterials (Lee *et al.*, 2017), Inorganic compounds, e.g., metal sulfides and metal oxides (Xia *et al.*, 2016), organic-based materials, e.g., conductive polymers and covalent organic frameworks (Zhao *et al.*, 2016), and selenium sulfides (Eftekhari, 2017).

Most of the host cathodes for Li-S batteries are somehow based-carbon materials because of simple preparation by carbonization, low cost, and generality. Various common forms have been applied to the host cathode material, such as spheres (Zhu *et al.*, 2015), porous (Deng *et al.*, 2016), nanofibers (Z. Zhang *et al.*, 2016), nanotubes (Wu *et al.*, 2014), aerogels (X. Li *et al.*, 2016), and three-dimensional interconnected (Rehman *et al.*, 2016). Such carbon allotropes-based cathodes provide different battery performances for Li-S batteries. For instance, porous carbon exhibits a specific capacity of 675 mA h g^{-1} at a 0.1 C rate (Ghazi *et al.*, 2016). Multiwalled carbon nanotubes provide 1450 mA h g^{-1} at a 0.2 C rate. Meanwhile, carbon microgels show 1132 mA h g^{-1} at a 0.1 C rate (Mentbayeva *et al.*, 2016). Although the development of the cathode shows growing interest in the Li-S batteries, it is still to be further ordered to obtain better performance.

One of the new low-dimensional carbon materials for the cathode is graphdiyne (GDY) which is one of the 2D-carbon allotropes built by the combination of sp - and sp^2 -hybridized carbon atoms (G. Li *et al.*, 2010). It is the repeating network of diacetylenic linkage connected to the benzene rings. Such planar provides a porous region with uniformly distributed pores of 5.42 \AA and a sizeable empty area of 6.30 \AA^2 , as illustrated in Figure 1.3 (Cranford *et al.*, 2012). This allotrope was first proposed by Haley, Brand, and Pak in 1987 (Baughman *et al.*, 1987). Afterward, experiments have been successfully synthesized since 2010, which offer the lattice parameter of the GDY unit cell with 9.458 \AA , and many fundamental properties have been explored (G. Li *et al.*, 2010).

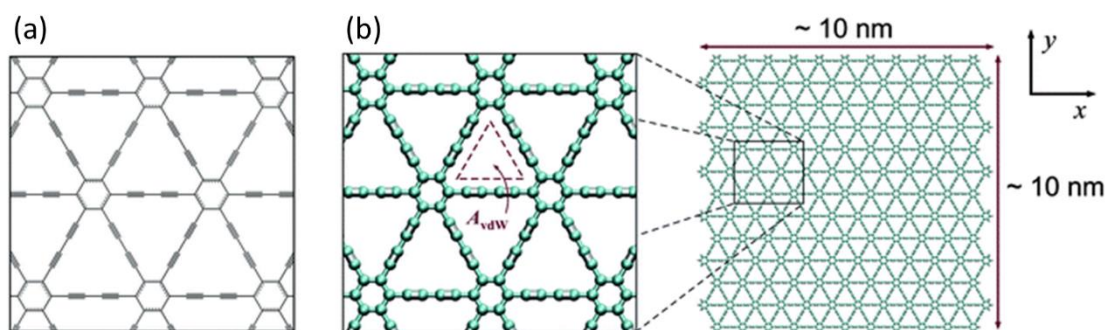


Figure 1.3 (a) chemical Lewis's structure of graphdiyne (GDY). (b) Full atomistic model of GDY depicting the triangular pore (Cranford *et al.*, 2012).

The investigation of electronic properties shows that GDY is a semiconductor with a small direct band gap of 0.46 eV at the gamma point. GDY has an intrinsic electron mobility of $20.81 \times 10^4 \text{ cm}^2 \text{ V}^{-1} \text{ S}^{-1}$, and the magnitude of hole mobility is lower ($1.97 \times 10^4 \text{ cm}^2 \text{ V}^{-1} \text{ S}^{-1}$) at room temperature (Gao *et al.*, 2019). Moreover, other works demonstrate that GDY material provides high nonlinear optical susceptibility, uniformly distributed pores, and low thermal conductivity; see references (R. Liu *et al.*, 2017). These impressions have pumped GDY up to attract significant attention for several applications such as energy storage and conversion, water remediation, gas separation, metal-free catalysis, and gas sensor.

In an energy storage technology framework, 2D-GDY material has been fabricated to apply as a battery host electrode. Experimental works have suggested that GDY is a promising energy storage material for Li-ion batteries and capacitors (H. Du *et al.*, 2016; Jang *et al.*, 2013). First-principles computation reveals that diffusion of Li^+ on both in-plane and out-plane GDY provides high ion mobility with a moderate activation barrier of 0.53 – 0.57 eV (H. Zhang *et al.*, 2013). Since 2017, cathode material based on sulfide graphdiyne (SGDY) has been designed for Li-S batteries, as shown in Figure 1.4. SGDY was prepared by a thermal synthesis production, where GDY powder and sublimed sulfur were mixed in a quartz mortar, then the mixture was heated at 350 °C for 3 hours in a tube furnace under an Ar environment. The results show that SGDY provides the first cycle reversible specific capacity of 960.9 mAh g^{-1} , high reversibility, and almost 100% Coulombic efficiency. Moreover, the SGDY cathode exhibits superior cycle stability with a high reversible

capacity of 821.4 (at 0.5 C) and 713.7 (at 1 C) mAh g⁻¹ upon 100 cycles, as shown in Figure 1.5 (H. Du *et al.*, 2017).

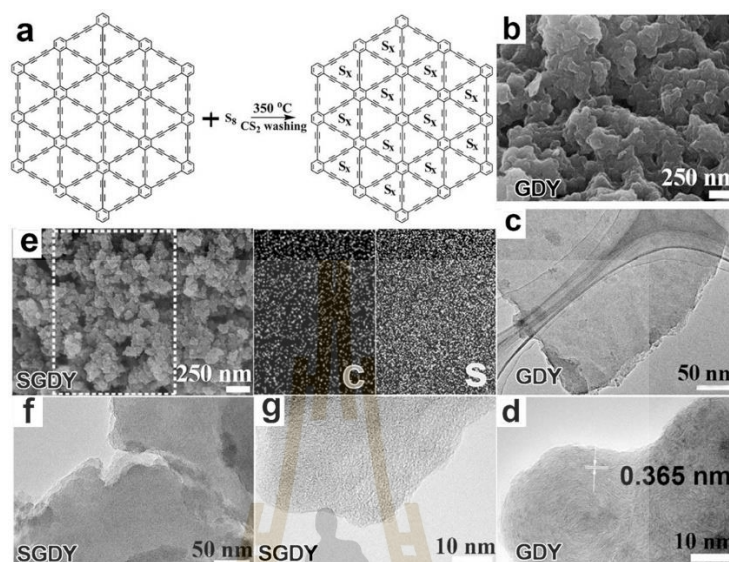


Figure 1.4 (a) The schematic of the preparation process of sulfide graphdiyne (SGDY). (b) SEM image of GDY. (c) TEM image of GDY. (d) HRTEM image of GDY. (e) SEM image of SGDY. (f) TEM image of SGDY. (g) HRTEM image of SGDY (H. Du *et al.*, 2017).

Although the sulfur cathode based on sulfide graphdiyne (SGDY) demonstrates excellent electrochemical performances such as high capacity, superior rate stability, and high Coulombic capacity, the SGDY composite still has some problems with shuttle effect and weak adsorption strength with sulfur materials. The first-principle calculation reveals that the adsorption energy between S₈ and pristine GDY monolayer is 0.410 eV which can be classified as the van der Waals interaction, suggesting low S₈ confinement within the cathode (Cai, 2020). In addition, the adsorption strength between long-chain LiPS species (i.e., Li₂S₈, Li₂S₆, and Li₂S₄) is in the range of 0.573 – 0.662 eV as weak physisorption (Cai, 2020). This adsorptivity cannot suppress the LiPSs solubility, leading to the shuttle effect. Thus, the main challenge in utilizing GDY as the host cathode is to design the carbon atoms capable of effective chemical adsorption with S₈ by increasing the electron-rich at an active site on the cathode surface.

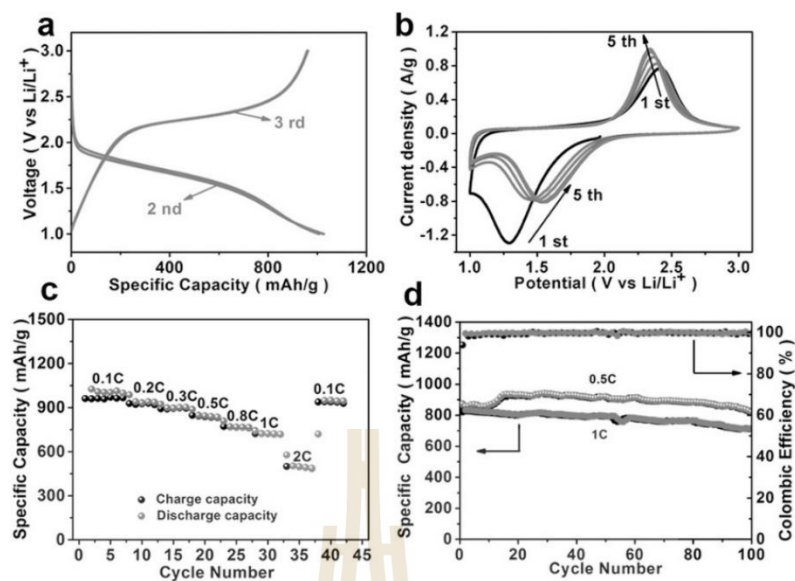


Figure 1.5 (a) The 2nd and 3rd charge/discharge of SGDY cathode at 0.1 C (1 C = 1672 mA g⁻¹). (b) CV curve at a scan rate of 0.1 mV s⁻¹. (c) Rate performance. (d) Cycling performance of SGDY cathode at current densities of 0.5 and 1 C (H. Du *et al.*, 2017).

1.3 Transition metal and nitrogen co-doping

Structural modification of 2D materials is one of the efficient strategies to alter the uniformity of charge distribution to promote chemical interaction with S₈. The possible way to intensify the adsorptivity of GDY from weak to strong binding is an atomic substitution of carbon atoms with other elements. Nitrogen doping is a common foreign element to substitute in a carbon material and has been widely used in carbon modification for Li-S batteries. For instance, nitrogen (N)-doped mesoporous carbon-based cathode shows a specific capacity of up to 1585 mA h g⁻¹ at a 0.1 C rate (Y. Liu *et al.*, 2016). Meanwhile, nitrogen-rich carbon nanotube/graphene also exhibits 1314 mA h g⁻¹ at a 0.2 C rate with high-capacity retention (Ding *et al.*, 2016). These doped N atoms with higher valence electrons are electron donors interacting with the travel Li atoms as electron acceptors in the LiPS molecules. Based on Lewis's acid-base theory, the electron donor with higher electronegativity acts as the Lewis base, whereas the electron acceptor with lower electronegativity acts as the Lewis acid, leading to a strong chemical interaction. For other dopants, boron (B)-dopant on porous carbon leads to a positive polarization of

carbon substrates and provides strong chemical interaction with S_8 and LiPSs (Yang *et al.*, 2014). However, other dopants (e.g., F, S, P, and Cl) are unfeasible to enhance the adsorptivity effectively and cannot inhibit the lithium polysulfide shuttling. Moreover, some works suggest that only N and O doping can improve the chemisorption between the cathode substrate and LiPS molecules (Eftekhari *et al.*, 2017).

Although the adsorptivity is improved upon N doping, there is still the problem of the shuttle effect and capacity fading when the batteries are used a lot. Both experiment and theoretical works show that only N doping cannot suppress LiPS shuttling. Therefore, co-doping is one of the possible ways to intensity the chemical interaction to obtain more effective N-doping. For example, cobalt (Co) and N co-doped graphene substrates have been synthesized to apply as host cathode for Li-S batteries. The experimental results reveal that the Co-N-C center behaves as a bifunctional electrocatalyst to contribute to the (de)formation of LiPS form, which yields a gravimetric capacity of 1210 mAh g^{-1} (Z. Du *et al.*, 2019). In addition, its first-principles calculation suggests that the LiPSs decomposition on the co-doped substrate provides a more minor activation energy barrier (1.4 eV) during discharge compared to that on the N-doped substrate (2.3 eV), as shown in Figure 1.6. Other computations reveal that the single-atom Fe and N co-doped graphene alters the adsorption with LiPS molecules, which can inhibit the dissociation of LiPSs into electrolyte solvents (J. Wang *et al.*, 2019). This is because of the synergetic role between transition metal (TM) and nitrogen in promoting the chemical interaction of the TM-S and Li-N bond. Interestingly, the energy barrier of LiPS decomposition is reduced in the presence of TM and N co-doping, accelerating the phase transformation during the (dis)charge process. Hence, the combination between TM and N substitution on a carbon material expectedly provides a significant impact on enhancing the battery performance in Li-S batteries.

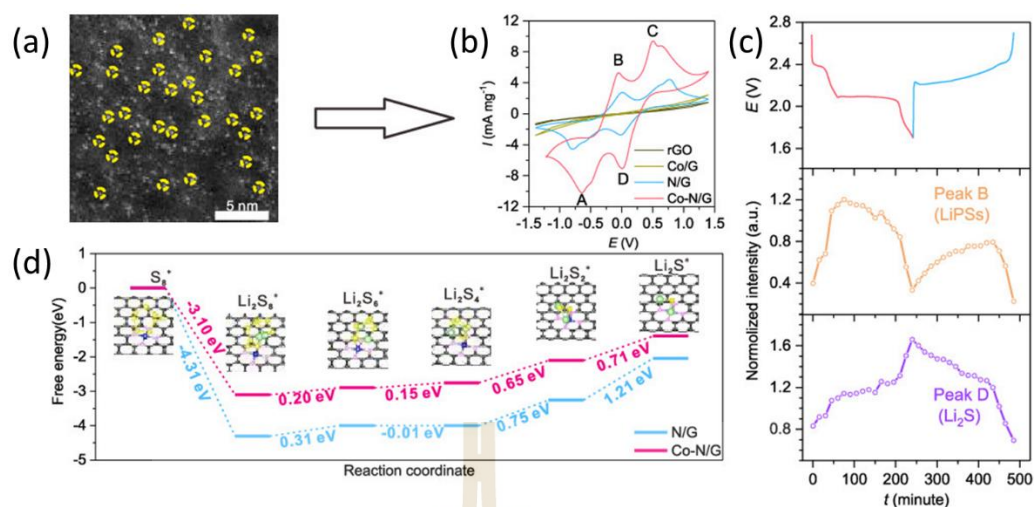


Figure 1.6 (a) HAADF-STEM image of Co-N doped graphene. (b) CV of symmetric cell with Co and N doping, N doping, and Co doping on graphene for Li-S battery. (c) Evolution of the intensities of peak B and peak D. (d) Energy profiles for LiPS on N-doped and Co-N-doped graphene (Z. Du *et al.*, 2019).

Recently, incorporating transition metals, including Co (X. Wang *et al.*, 2019) and Fe atom (Si *et al.*, 2019), in the N-doped GDY have successfully been fabricated as a novel electrocatalyst for both the oxygen reactions (ORR) and hydrogen evolution reactions (HER). The Schematic illustration of the synthetic procedure is shown in Figure 1.7. Co and Fe are much attention to because of their excellent catalytic activity for LiPS phase transformation. The material characterization reveals that C atoms in the GDY structure were substituted by N atoms, whereas Co atoms/clusters were trapped on the GDY surface. However, such TM and N co-doped GDY have not been applied yet as host cathode materials for Li-S batteries. According to the previous mention of the exciting properties of GDY and co-doping, there motivated good attention to the use TM and N co-doped GDY to be a promising host cathode as a new candidate material for Li-S batteries.

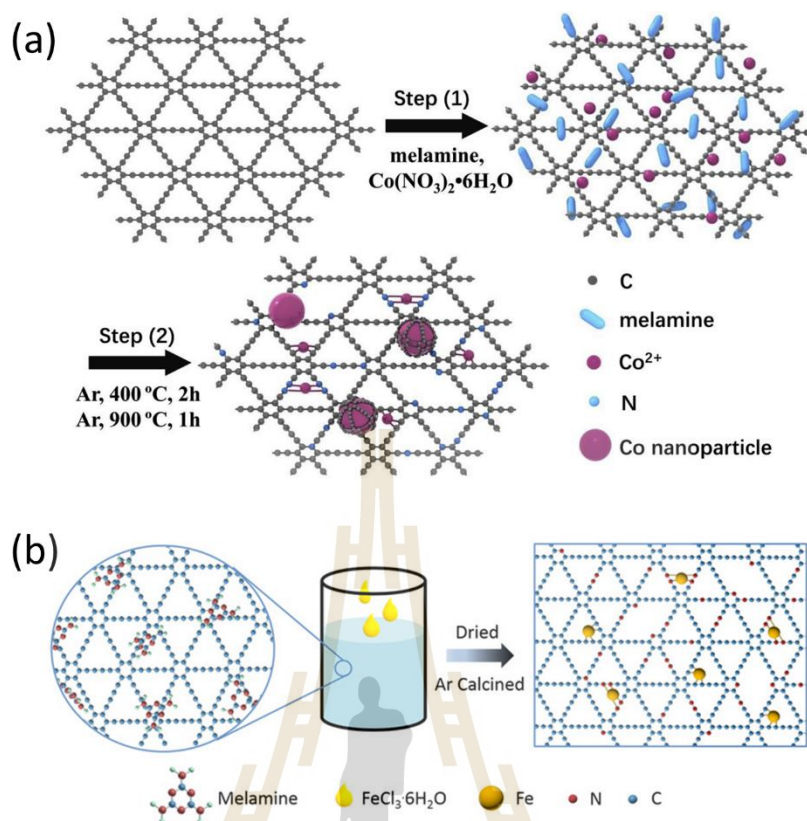


Figure 1.7 Schematic illustration of the synthetic procedure of (a) Co-N doped GDY (X. Wang *et al.*, 2019) and (b) Fe-N doped GDY (Si *et al.*, 2019) from experimental views.

1.4 Research objectives

Here, we studied the properties of pristine GDY and the TM and N co-doped GDY material as a host cathode for Li-S batteries using the standard computation methods, including the density functional theory (DFT) approach and ab-initio molecular dynamics (AIMD) simulation. The doped GDY models were constructed by doping N and TM (Co and Fe) atoms to find the most stable structural configuration. Two main aspects were investigated: (i) the adsorptivity of S_8 and LiPS molecules on the pristine and doped GDY monolayer to assess the ability to suppress the polysulfide shuttling, and (ii) the thermodynamic and kinetic behaviors of the decomposition reaction of small LiPSs.

1.5 Scope and limitations

In this thesis, all calculations were carried out using the spin-polarized DFT method via the plane-wave technique implemented in the Vienna ab initio Simulation Package (VASP 5.3) with the frozen-core projector-augmented wave (PAW) approach to treat the electron-ion interaction. The exchange-correlation functional was described by the generalized gradient approximation of Perdew-Burke-Ernzerhof (PBE). Even though obtained theoretical results in the framework of the DFT study (e.g., the total energy of a system, mechanical properties) provides an outcome accurately, corresponding electronic properties with especially band energy gap are underestimated smaller than experimental reports. This underestimation occurs from the intrinsic self-interaction error in the PBE approximation. However, electronic density of state (DOS) and band structure calculation still provides satisfactory results to explain an electronic feature of electron states and the other essential characteristics. In addition, the DOS-related electronic structure cannot simply be directly related to macroscopic conductivity.

The charge distribution on atoms and the amount of charge transfer were analyzed via the Bader charge calculation. This method considered the Bader volume of an atom enclosed to estimate the zero flux regions and determine the net charge on particles. However, the assigned charge was not distinguished by an integer number.

Nudged elastic band (NEB) approach is applied to find the minimum energy pathway (MEP), which passes over the energy barrier between the initial and final state for the catalytic decomposition path of LiPS dissociation and diffusion path of Li-ion to describe the ability of phase transformation during the charging process. It should be noted that the curvature of MEP possesses a limit of saddle points. Our NEB calculation was given five images as an intermediate configuration between the initial and final states.

1.6 References

- Armand, M., and Tarascon, J. M. (2008). Building better batteries. *Nature*. *451*: 652.
- Assary, R. S., Curtiss, L. A., and Moore, J. S. (2014). Toward a Molecular Understanding of Energetics in Li-S Batteries Using Nonaqueous Electrolytes: A High-Level Quantum Chemical Study. *The Journal of Physical Chemistry C*. *118*: 11545.
- Aurbach, D., McCloskey, B. D., Nazar, L. F., and Bruce, P. G. (2016). Advances in understanding mechanisms underpinning lithium-air batteries. *Nature Energy*. *1*: 1.
- Barchasz, C., Molton, F., Duboc, C., Leprêtre, J.-C., Patoux, S., and Alloin, F. (2012). Lithium/Sulfur Cell Discharge Mechanism: An Original Approach for Intermediate Species Identification. *Analytical Chemistry*. *84*: 3973.
- Barghamadi, M., Kapoor, A., and Wen, C. (2013). A Review on Li-S Batteries as a High Efficiency Rechargeable Lithium Battery. *Journal of The Electrochemical Society*. *160*: A1256.
- Baughman, R. H., Eckhardt, H., and Kertesz, M. (1987). Structure-property predictions for new planar forms of carbon: Layered phases containing sp² and sp atoms. *The Journal of Chemical Physics*. *87*: 6687.
- Boundy, R. G. (2019). Transportation Energy Data Book: Edition 37: Oak Ridge National Lab.(ORNL), Oak Ridge, TN (United States).
- Bradford, T. (2018). The energy system: Technology, economics, markets, and policy: MIT Press.
- Bresser, D., Passerini, S., and Scrosati, B. (2013). Recent progress and remaining challenges in sulfur-based lithium secondary batteries – a review. *Chemical Communications*. *49*: 10545.
- Cai, Y. (2020). The Anchoring Effect of 2D Graphdiyne Materials for Lithium-Sulfur Batteries. *ACS Omega*. *5*: 13424.
- Canfield, D. E. (2001). Biogeochemistry of Sulfur Isotopes. *Reviews in Mineralogy and Geochemistry*. *43*: 607.
- Cranford, S. W., and Buehler, M. J. (2012). Selective hydrogen purification through graphdiyne under ambient temperature and pressure. *Nanoscale*. *4*: 4587.

- Deng, W., Hu, A., Chen, X., Zhang, S., Tang, Q., Liu, Z., Fan, B., and Xiao, K. (2016). Sulfur-impregnated 3D hierarchical porous nitrogen-doped aligned carbon nanotubes as high-performance cathode for lithium-sulfur batteries. *Journal of Power Sources*. 322: 138.
- Ding, Y.-L., Kopold, P., Hahn, K., van Aken, P. A., Maier, J., and Yu, Y. (2016). Facile Solid-State Growth of 3D Well-Interconnected Nitrogen-Rich Carbon Nanotube–Graphene Hybrid Architectures for Lithium–Sulfur Batteries. *Advanced Functional Materials*. 26: 1112.
- Du, H., Yang, H., Huang, C., He, J., Liu, H., and Li, Y. (2016). Graphdiyne applied for lithium-ion capacitors displaying high power and energy densities. *Nano Energy*. 22: 615.
- Du, H., Zhang, Z., He, J., Cui, Z., Chai, J., Ma, J., Yang, Z., Huang, C., and Cui, G. (2017). A Delicately Designed Sulfide Graphdiyne Compatible Cathode for High-Performance Lithium/Magnesium–Sulfur Batteries. *Small*. 13: 1702277.
- Du, Z., Chen, X., Hu, W., Chuang, C., Xie, S., Hu, A., Yan, W., Kong, X., Wu, X., Ji, H., and Wan, L.-J. (2019). Cobalt in Nitrogen-Doped Graphene as Single-Atom Catalyst for High-Sulfur Content Lithium–Sulfur Batteries. *Journal of the American Chemical Society*. 141: 3977.
- Eftekhari, A. (2017). The rise of lithium–selenium batteries. *Sustainable Energy & Fuels*. 1: 14.
- Eftekhari, A., and Kim, D.-W. (2017). Cathode materials for lithium–sulfur batteries: a practical perspective. *Journal of Materials Chemistry A*. 5: 17734.
- Faraji, F., Majazi, A., and Al-Haddad, K. (2017). A comprehensive review of flywheel energy storage system technology. *Renewable and Sustainable Energy Reviews*. 67: 477.
- Gao, X., Liu, H., Wang, D., and Zhang, J. (2019). Graphdiyne: synthesis, properties, and applications. *Chemical Society Reviews*. 48: 908.
- Ghazi, Z. A., Zhu, L., Wang, H., Naeem, A., Khattak, A. M., Liang, B., Khan, N. A., Wei, Z., Li, L., and Tang, Z. (2016). Efficient Polysulfide Chemisorption in Covalent Organic Frameworks for High-Performance Lithium-Sulfur Batteries. *Advanced Energy Materials*. 6: 1601250.

- Goodenough, J. B., and Park, K.-S. (2013). The Li-Ion Rechargeable Battery: A Perspective. *Journal of the American Chemical Society*. 135: 1167.
- Hall, P. J., Mirzaeian, M., Fletcher, S. I., Sillars, F. B., Rennie, A. J., Shitta-Bey, G. O., Wilson, G., Cruden, A., and Carter, R. (2010). Energy storage in electrochemical capacitors: designing functional materials to improve performance. *Energy & Environmental Science*. 3: 1238.
- He, Z., Lv, Y., Zhang, T., Zhu, Y., Dai, L., Yao, S., Zhu, W., and Wang, L. (2022). Electrode materials for vanadium redox flow batteries: Intrinsic treatment and introducing catalyst. *Chemical Engineering Journal*. 427: 131680.
- Huang, J.-Q., Zhang, Q., and Wei, F. (2015). Multi-functional separator/interlayer system for high-stable lithium-sulfur batteries: Progress and prospects. *Energy Storage Materials*. 1: 127.
- Jang, B., Koo, J., Park, M., Lee, H., Nam, J., Kwon, Y., and Lee, H. (2013). Graphdiyne as a high-capacity lithium ion battery anode material. *Applied Physics Letters*. 103: 263904.
- Ji, X., Lee, K. T., and Nazar, L. F. (2009). A highly ordered nanostructured carbon-sulphur cathode for lithium-sulphur batteries. *Nature Materials*. 8: 500.
- Khan, Z., Vagin, M., and Crispin, X. (2020). Can hybrid Na-air batteries outperform nonaqueous Na-O₂ batteries? *advanced science*. 7: 1902866.
- Kutscher, C. F., Milford, J. B., and Kreith, F. (2018). Principles of sustainable energy systems: CRC Press.
- Lee, J. S., and Manthiram, A. (2017). Hydroxylated N-doped carbon nanotube-sulfur composites as cathodes for high-performance lithium-sulfur batteries. *Journal of Power Sources*. 343: 54.
- Li, G., Li, Y., Liu, H., Guo, Y., Li, Y., and Zhu, D. (2010). Architecture of graphdiyne nanoscale films. *Chemical Communications*. 46: 3256.
- Li, X., Tang, R., Hu, K., Zhang, L., and Ding, Z. (2016). Hierarchical Porous Carbon Aerogels with VN Modification as Cathode Matrix for High Performance Lithium-Sulfur Batteries. *Electrochimica Acta*. 210: 734.

- Liang, Y., Zhao, C. Z., Yuan, H., Chen, Y., Zhang, W., Huang, J. Q., Yu, D., Liu, Y., Titirici, M. M., and Chueh, Y. L. (2019). A review of rechargeable batteries for portable electronic devices. *InfoMat*. 1: 6.
- Liu, R., Zhou, J., Gao, X., Li, J., Xie, Z., Li, Z., Zhang, S., Tong, L., Zhang, J., and Liu, Z. (2017). Graphdiyne Filter for Decontaminating Lead-Ion-Polluted Water. *Advanced Electronic Materials*. 3: 1700122.
- Liu, X., Shao, X., Li, F., and Zhao, M. (2018). Anchoring effects of S-terminated Ti2C MXene for lithium-sulfur batteries: A first-principles study. *Applied Surface Science*. 455: 522.
- Liu, Y., Zhao, X., Chauhan, G. S., and Ahn, J.-H. (2016). Nanostructured nitrogen-doped mesoporous carbon derived from polyacrylonitrile for advanced lithium sulfur batteries. *Applied Surface Science*. 380: 151.
- Lu, X., and Wang, S. (2017). A GIS-based assessment of Tibet's potential for pumped hydropower energy storage. *Renewable and Sustainable Energy Reviews*. 69: 1045.
- Ma, L., Hendrickson, K. E., Wei, S., and Archer, L. A. (2015). Nanomaterials: Science and applications in the lithium-sulfur battery. *Nano Today*. 10: 315.
- Manthiram, A., Fu, Y., Chung, S.-H., Zu, C., and Su, Y.-S. (2014). Rechargeable Lithium-Sulfur Batteries. *Chemical Reviews*. 114: 11751.
- Mentbayeva, A., Belgibayeva, A., Umirov, N., Zhang, Y., Taniguchi, I., Kurmanbayeva, I., and Bakenov, Z. (2016). High performance freestanding composite cathode for lithium-sulfur batteries. *Electrochimica Acta*. 217: 242.
- Mikhaylik, Y. V., and Akridge, J. R. (2004). Polysulfide Shuttle Study in the Li/S Battery System. *Journal of The Electrochemical Society*. 151: A1969.
- Moy, D., Manivannan, A., and Narayanan, S. R. (2014). Direct Measurement of Polysulfide Shuttle Current: A Window into Understanding the Performance of Lithium-Sulfur Cells. *Journal of The Electrochemical Society*. 162: A1.
- Ni, Q., Bai, Y., Wu, F., and Wu, C. (2017). Polyanion-type electrode materials for sodium-ion batteries. *Advanced Science*. 4: 1600275.
- Pang, Q., Shyamsunder, A., Narayanan, B., Kwok, C. Y., Curtiss, L. A., and Nazar, L. F. (2018). Tuning the electrolyte network structure to invoke quasi-solid state

- sulfur conversion and suppress lithium dendrite formation in Li-S batteries. *Nature Energy*. 3: 783.
- Placke, T., Kloepsch, R., Dühnen, S., and Winter, M. (2017). Lithium ion, lithium metal, and alternative rechargeable battery technologies: the odyssey for high energy density. *Journal of Solid State Electrochemistry*. 21: 1939.
- Rehman, S., Gu, X., Khan, K., Mahmood, N., Yang, W., Huang, X., Guo, S., and Hou, Y. (2016). 3D Vertically Aligned and Interconnected Porous Carbon Nanosheets as Sulfur Immobilizers for High Performance Lithium-Sulfur Batteries. *Advanced Energy Materials*. 6: 1502518.
- Si, W., Yang, Z., Wang, X., Lv, Q., Zhao, F., Li, X., He, J., Long, Y., Gao, J., and Huang, C. (2019). Fe,N-Codoped Graphdiyne Displaying Efficient Oxygen Reduction Reaction Activity. *ChemSusChem*. 12: 173.
- Smith, W. (2000). The role of fuel cells in energy storage. *Journal of Power Sources*. 86: 74.
- Wang, J., Jia, L., Zhong, J., Xiao, Q., Wang, C., Zang, K., Liu, H., Zheng, H., Luo, J., Yang, J., Fan, H., Duan, W., Wu, Y., Lin, H., and Zhang, Y. (2019). Single-atom catalyst boosts electrochemical conversion reactions in batteries. *Energy Storage Materials*. 18: 246.
- Wang, X., Yang, Z., Si, W., Shen, X., Li, X., Li, R., Lv, Q., Wang, N., and Huang, C. (2019). Cobalt-nitrogen-doped graphdiyne as an efficient bifunctional catalyst for oxygen reduction and hydrogen evolution reactions. *Carbon*. 147: 9.
- Wang, Y.-X., Zhang, B., Lai, W., Xu, Y., Chou, S.-L., Liu, H.-K., and Dou, S.-X. (2017). Room-Temperature Sodium-Sulfur Batteries: A Comprehensive Review on Research Progress and Cell Chemistry. *Advanced Energy Materials*. 7: 1602829.
- Whittingham, M. S. (1976). Electrical Energy Storage and Intercalation Chemistry. *Science*. 192: 1126.
- Wild, M., O'Neill, L., Zhang, T., Purkayastha, R., Minton, G., Marinescu, M., and Offer, G. J. (2015). Lithium sulfur batteries, a mechanistic review. *Energy & Environmental Science*. 8: 3477.

- Wu, Y., Xu, C., Guo, J., Su, Q., Du, G., and Zhang, J. (2014). Enhanced electrochemical performance by wrapping graphene on carbon nanotube/sulfur composites for rechargeable lithium–sulfur batteries. *Materials Letters*. 137: 277.
- Xia, Y., Wang, B., Zhao, X., Wang, G., and Wang, H. (2016). Core-shell composite of hierarchical MoS₂ nanosheets supported on graphitized hollow carbon microspheres for high performance lithium-ion batteries. *Electrochimica Acta*. 187: 55.
- Yang, C.-P., Yin, Y.-X., Ye, H., Jiang, K.-C., Zhang, J., and Guo, Y.-G. (2014). Insight into the Effect of Boron Doping on Sulfur/Carbon Cathode in Lithium–Sulfur Batteries. *ACS Applied Materials & Interfaces*. 6: 8789.
- Yin, Y.-X., Xin, S., Guo, Y.-G., and Wan, L.-J. (2013). Lithium–Sulfur Batteries: Electrochemistry, Materials, and Prospects. *Angewandte Chemie International Edition*. 52: 13186.
- Zhang, C., Wei, Y.-L., Cao, P.-F., and Lin, M.-C. (2018). Energy storage system: Current studies on batteries and power condition system. *Renewable and Sustainable Energy Reviews*. 82: 3091.
- Zhang, H., Xia, Y., Bu, H., Wang, X., Zhang, M., Luo, Y., and Zhao, M. (2013). Graphdiyne: A promising anode material for lithium ion batteries with high capacity and rate capability. *Journal of Applied Physics*. 113: 044309.
- Zhang, Z., Wang, G., Lai, Y., and Li, J. (2016). A freestanding hollow carbon nanofiber/reduced graphene oxide interlayer for high-performance lithium–sulfur batteries. *Journal of Alloys and Compounds*. 663: 501.
- Zhao, Y., Zhu, W., Chen, G. Z., and Cairns, E. J. (2016). Polypyrrole/TiO₂ nanotube arrays with coaxial heterogeneous structure as sulfur hosts for lithium sulfur batteries. *Journal of Power Sources*. 327: 447.
- Zhu, L., Peng, H.-J., Liang, J., Huang, J.-Q., Chen, C.-M., Guo, X., Zhu, W., Li, P., and Zhang, Q. (2015). Interconnected carbon nanotube/graphene nanosphere scaffolds as free-standing paper electrode for high-rate and ultra-stable lithium–sulfur batteries. *Nano Energy*. 11: 746.

CHAPTER II

FIRST-PRINCIPLES METHODS

In this chapter, we will elucidate the theoretical and computational approaches at the core level of the implementation in this work. The computational tool is beneficial to provide a basic explanation of solid-state chemistries. Here, we will first introduce the fundamental equation of quantum mechanics with the Schrödinger equation for many-body particle systems to discuss how the solid-state material is discussed from the atomic perspective (section 2.1). Secondly, the development of density functional theory (DFT) as a computational quantum modeling will be described (section 2.2). The electron density and its roles will be reviewed. Next, the approximated approach used for the exchange-correlation functional will be explained in section 2.3, followed by the discussion of the wave function and pseudopotential (section 2.4). Moreover, based on the dynamic study, the introduction of the ab-initio molecular dynamics (AIMD) simulation will be described (section 2.5). Finally, the summary of the computational details in this work, set in the Vienna Ab initio Simulation Package (VASP), will be elucidated in section 2.6.

2.1 Many-body Schrödinger equation

The behavior of atomic nucleus and interacting electrons in a lattice solid-state system is fully described by quantum mechanics, which derives from the Many-body Schrödinger equation. The so-called time-independent Schrödinger equation as a simple form to explain such particle behavior in the system is

$$\hat{H}\Psi(\{\vec{R}_l; \vec{r}_i\}) = E\Psi(\{\vec{R}_l; \vec{r}_i\}) \quad (2.1)$$

where \hat{H} is the Hamiltonian operator, $\Psi(\{\hat{R}_l; \hat{r}_i\})$ is a wavefunction, E is a energy of the system, \vec{R}_l is a position of nucleus l , and \vec{r}_i is a position of an electron i . The Hamiltonian operator for the many-body system consists of both kinetic and potential energy terms; the kinetic operator (\hat{T}), the potential operator of nucleus-nucleus

interaction (\hat{V}_{NN}), the potential operator of electron-electron interaction (\hat{V}_{ee}), and the potential operator of nucleus-electrons interaction (\hat{V}_{Ne}), which can be written as

$$\hat{H} = \hat{T} + \hat{V}_{NN} + \hat{V}_{ee} + \hat{V}_{Ne} \quad (2.2)$$

From the above equation, the kinetic energy operator can be described as the following

$$\hat{T} = -\sum_{l=1}^M \frac{\hbar^2}{2m_l} \nabla_{\vec{R}_l}^2 - \sum_{i=1}^N \frac{\hbar^2}{2m_e} \nabla_{\vec{r}_i}^2 \quad (2.3)$$

where m_l is a mass of nucleus l with M particles, and m_e is a mass of an electron with N particles in the system. For the term of potential energy, the potential operator of the interaction between arbitrary two nuclei at position

$$\hat{V}_{NN} = \sum_{i>j} \frac{1}{4\pi\epsilon_0} \frac{Z_i Z_j e^2}{|\vec{R}_i - \vec{R}_j|} \quad (2.4)$$

where Z_i and Z_j are the atomic number of nuclei i and j , respectively. While the potential energy operator of the electron-electron interactions at positions \vec{r}_i and \vec{r}_j is similar as shown in above

$$\hat{V}_{ee} = \sum_{i>j} \frac{1}{4\pi\epsilon_0} \frac{e^2}{|\vec{r}_i - \vec{r}_j|} \quad (2.5)$$

For the last term in Eq. 2.2, the total potential operator of the interaction between nucleus l and electron l can be presented as the following

$$\hat{V}_{Ne} = \sum_{l=1}^M \sum_{i=1}^N \frac{1}{4\pi\epsilon_0} \frac{Z_l e^2}{|\vec{R}_l - \vec{r}_i|} \quad (2.6)$$

Although the time-independent form is more simplified, it is still complicated and difficult to solve the exact solution. In the solid-state system with several particles, there is the high dimensionality of Ψ .

The Born-Oppenheimer approximation (Born *et al.*, 1927; Cederbaum, 2008) has been proposed to reduce the complexity of the Schrödinger equation by cutting the terms of kinetic and potential operators of the nucleus. This principle assumes that the motion of the nucleus in the system is languid and that the difference in mass between a nucleus and an electron is massive. In addition, the potential energy of nucleus-nucleus interaction is treated to be constant, where the degree of freedom of

an electron is taken into account. Therefore, the reduced Hamiltonian operator becomes

$$\hat{H} = -\sum_{i=1}^N \frac{\hbar^2}{2m_e} \nabla_{\vec{r}_i}^2 + \hat{V}_{ee} + \hat{V}_{Ne} \quad (2.7)$$

or

$$\hat{H} = -\sum_{i=1}^N \frac{\hbar^2}{2m_e} \nabla_{\vec{r}_i}^2 + \sum_{i>j} \frac{1}{4\pi\epsilon_0} \frac{e^2}{|\vec{r}_i - \vec{r}_j|} + \sum_{l=1}^M \sum_{i=1}^N \frac{1}{4\pi\epsilon_0} \frac{Z_l e^2}{|\vec{R}_l - \vec{r}_i|} \quad (2.8)$$

Therefore, we obtain the reduced Schrödinger equation as

$$\hat{H}\Psi(\{\vec{r}_i\}) = E\Psi(\{\vec{r}_i\}) \quad (2.9)$$

Despite this simplification, solving $\Psi(\{\vec{r}_i\})$ remains difficult. The increase of N electrons in the system affects the rapid expansion of dimensionality Ψ . If two electrons with the same spin interchanges positions, much turn side (“exchange” property) is governed by the Pauli exclusion principle. Moreover, the influence of motion of surrounding electrons in the system affects each other (“correlation” property). Such complex phenomena also lead to difficult tasks in solving the solution. Therefore, the several approximation principles were further developed to obtain a simpler form of the Schrödinger equation for electrons in the lattice system.

2.2 Hartree-Fock approximation

Although Schrödinger equation is helpful to describe the behaviors of particles in many-body quantum systems, it is only useful for the small systems due to the high complexity. Many approaches have been proposed to simplify the approximated Schrödinger equation. John C. Slater (1900-1976) (Slater, 1930) proposed the simple approximate expression for a wavefunction of a multi-fermionic system and the mean-field approaches. Hartree proposed the simple approximation method to solve the solution of Schrödinger equation, but the Hartree approach still provided a significant inaccuracy. Hartree-Fock method (1930) (Fock, 1930; Hartree, 1928) was determined to estimate the Schrödinger equation by regarding the Slater determinant to yield the Hartree-Fock wave function and energy of the system, where the Hartree-Fock wavefunction, $\Psi^{HF}(\{\vec{r}_i\})$, can be written as

$$\Psi^{\text{HF}}(\{\vec{r}_i\}) = \frac{1}{\sqrt{N!}} \begin{vmatrix} \psi_1(\vec{r}_1) & \psi_1(\vec{r}_2) & \cdots & \psi_1(\vec{r}_N) \\ \psi_2(\vec{r}_1) & \psi_2(\vec{r}_2) & \cdots & \psi_2(\vec{r}_N) \\ \vdots & \vdots & \ddots & \vdots \\ \psi_N(\vec{r}_1) & \psi_N(\vec{r}_2) & \cdots & \psi_N(\vec{r}_N) \end{vmatrix} \quad (2.10)$$

Where N is the total number of electrons. This wavefunction is taken into account the antisymmetric property and the Pauli exclusion principle. The electrons can interchange the position that accurately switches the corresponding columns in the determinant. The Hartree-Fock Hamiltonian can be presented as the below equation,

$$\left[-\frac{\hbar^2}{2m_e} \nabla_r^2 + \hat{V}_{Ne} + \hat{V}_i^H + \hat{V}_i^X \right] \psi_i(\vec{r}_i) = \epsilon_i \psi_i(\vec{r}_i) \quad (2.11)$$

where \hat{V}_i^H and \hat{V}_i^X are the Hartree and exchange potential operators, respectively. Therefore, the Hartree-Fock potential operator, $\hat{V}_i^{\text{HF}} = \hat{V}_i^H + \hat{V}_i^X$, is the combination between \hat{V}_i^H and \hat{V}_i^X , where can be written as a function of the Hartree-Fock density, $\rho_i^{\text{HF}}(\vec{r}, \vec{r}')$, as the following

$$\hat{V}_i^{\text{HF}} = \frac{e^2}{4\pi\epsilon_0} \int \frac{\rho(\vec{r}') - \rho_i^{\text{HF}}(\vec{r}, \vec{r}')}{|\vec{r} - \vec{r}'|} d\vec{r}' \quad (2.12)$$

The first term deals with the total Coulomb repulsion potential and the last term is the fermionic exchange effect. The Hartree-Fock approximation is more accurate than the Hartree one. However, it does not consider the correlation effect of the electron interaction in the system. At the present, the analytical form of the correlation has not been found. The Hartree-Fock wavefunction equation is useful for the small system but useless with the increase of particles in the system.

2.3 Density functional theory

Density functional theory (DFT) is a modeling method for ab-initio quantum mechanics, which is basically studied the fundamental properties of atoms and electrons in the many-body system. The electron density is the main concept of the DFT approach, which expresses the exchange-correlation energy from the Hohenberg-

Kohn theorems. Meanwhile, Kohn-Sham's equation developed the electron density and the single-particle wavefunction.

2.3.1 Electron density

The concept of the DFT scheme considers the total electron density, $\rho(\vec{r})$, instead of the particles in the systems. This concept contributes to obtaining a more simple approximation of the Schrödinger equation than the Hartree-Fock approximation. The electron density can be written in terms of the wavefunction:

$$\rho(\vec{r}) = \sum_i |\psi_i(\vec{r})|^2 \quad (2.13)$$

where this electron density does not have the interaction with each other. Some literature replaced $\psi_i(\vec{r})$ by orbital $\phi_i(\vec{r})$, indicating a noninteracting electron system (the so-called Kohn-Sham orbitals).

2.3.2 The Hohenberg-Kohn theorems

In 1964, Hohenberg and Kohn (Hohenberg *et al.*, 1964) proposed the two theorems, that identified the character of electron density as an essential factor in the DFT approach, where both theorems involved the wavefunction, Hamiltonian, and external energy, as follows:

- **The first theorem:** the external potential $V_{ext}(\vec{r})$ is determined within a trivial additive constant by a ground-state electron density $\rho(\vec{r})$.
- **The second theorem:** the minimal ground state energy of the system $E_0[\rho(\vec{r})]$ that is the functional of electron density can be calculated in terms of the dependent-internal energies $F_{HK}[\rho(\vec{r})]$ and the independent-external potential $E_{ext}[\rho(\vec{r})]$, as follows:

$$E_0[\rho(\vec{r})] = F_{HK}[\rho(\vec{r})] + E_{ext}[\rho(\vec{r})] \quad (2.14)$$

Where the derivative of the total energy functional depended on $\rho(\vec{r})$ can be considered by variation principle:

$$\left. \frac{\delta E_0[\rho(\vec{r})]}{\delta N} \right|_{\rho=\rho_0} = 0 \quad \text{when} \quad N = \int \rho(\vec{r}) d\vec{r} \quad (2.15)$$

2.3.3 The Kohn-Sham equation

In 1965, Kohn and Sham (Kohn *et al.*, 1965) proposed the simple concept for solving the many-body problem derived from the independent electron

approximation. This concept assumes that each electron in the system moves liberally, where the average potential field is attributed to the interaction between electrons and nuclei in the system. Depending on the 2nd Hohenberg-Kohn theorem as Eq. 2.14, the total internal energy, $F_{HK}[\rho(\vec{r})]$, can be written as

$$F_{HK}[\rho(\vec{r})] = T_{non}[\rho(\vec{r})] + E_{ee}[\rho(\vec{r})] + E_{Ne}[\rho(\vec{r})] \quad (2.16)$$

where $T_{non}[\rho(\vec{r})]$ is a non-interacting kinetic energy, $E_{ee}[\rho(\vec{r})]$ is the energy of two electrons interaction and is the energy of the interaction between an electron and the present nucleus. These correct terms in the Eq. 2.16 can be written as a function of the electron density as

$$T_{non}[\rho(\vec{r})] = -\sum_{i=1}^N \frac{\hbar^2}{2m} \nabla^2$$

$$E_{ee}[\rho(\vec{r})] = \frac{1}{2} \frac{1}{4\pi\epsilon_0} \iint \frac{\rho(\vec{r}_1)\rho(\vec{r}_2)e^2}{|\vec{r}_1 - \vec{r}_2|} d\vec{r}_1 d\vec{r}_2$$

and

$$E_{Ne}[\rho(\vec{r})] = \frac{1}{4\pi\epsilon_0} \sum_{i=1}^N \frac{\rho(\vec{r})Z_i e^2}{|\vec{R}_i - \vec{r}|} \quad (2.17)$$

For the final right term in the Eq. 2.14, the total external energy, $E_{ext}[\rho(\vec{r})]$, is complained by

$$E_{ext}[\rho(\vec{r})] = T_{int}[\rho(\vec{r})] + E_x[\rho(\vec{r})] + E_c[\rho(\vec{r})] \quad (2.18)$$

where $T_{int}[\rho(\vec{r})]$ is a interacting kinetic energy, $E_x[\rho(\vec{r})]$ and $E_c[\rho(\vec{r})]$ are the exchange and correlation energy, respectively. However, in DFT approach, the term of external energy does not have the exact uniform. We will call all energy term of the external energies as the exchange-correlation energy, $E_{xc}[\rho(\vec{r})]$. Therefore, the total energy of ground state can be written as

$$E_0[\rho(\vec{r})] = T_{non}[\rho(\vec{r})] + E_{ee}[\rho(\vec{r})] + E_{Ne}[\rho(\vec{r})] + E_{xc}[\rho(\vec{r})] \quad (2.19)$$

From above equation, we obtain the potential operator that corresponds to the ground-state total energy (so-called the effective potential operator; $\hat{V}_{eff}[\rho(\vec{r})]$), depended on the electron density. Therefore, the simplified Schrödinger equation can be presented as

$$\left[\frac{\nabla_i^2}{2} + \hat{V}_{eff}[\rho(\vec{r})] \right] \Psi_i^{KS}(\vec{r}) = E_i \Psi_i^{KS}(\vec{r}) \quad (2.20)$$

We can call the Eq. 2.20 as Kohn-Sham equation, where $\Psi_i^{KS}(\vec{r})$ is Kohn-Sham orbital, E_i is the energy as an eigenvalue, corresponding to $\Psi_i^{KS}(\vec{r})$. $\hat{V}_{eff}[\rho(\vec{r})]$ is the effective potential operator comprised of

$$\begin{aligned}\hat{V}_{eff}[\rho(\vec{r})] &= \hat{V}_H[\rho(\vec{r})] + \hat{V}_{ext}[\rho(\vec{r})] + \hat{V}_{xc}[\rho(\vec{r})] \\ &= \frac{1}{2} \int \frac{\rho(\vec{r}')}{|\vec{r} - \vec{r}'|} d\vec{r}' - \sum_{j=1}^N \frac{Z_j}{|\vec{R}_j - \vec{r}|} + \hat{V}_{xc}[\rho(\vec{r})]\end{aligned}\quad (2.21)$$

where $\hat{V}_H[\rho(\vec{r})]$ is the Hartree potential operator, experienced by the total potential of the electron density in the system at position \vec{r} , $\hat{V}_{ext}[\rho(\vec{r})]$ is the external potential operator of the interaction between an electron and nucleus at position \vec{r} , and the last term $\hat{V}_{xc}[\rho(\vec{r})]$ is the exchange-correlation potential operator, which relates to the exchange-correlation energy as

$$V_{xc}[\rho(\vec{r})] = \frac{\delta E_{xc}[\rho(\vec{r})]}{\delta \rho(\vec{r})}\quad (2.22)$$

The exchange-correlation term does not have the exact form because we cannot know an analytically total energy form, including an interacting kinetic energy, exchange energy, and correlation energy. It is important to find the approximated exchange-correlation energy to solve the Kohn-Sham equation.

2.3.4 Exchange-correlation functional

In DFT functional when dealing with Kohn-Sham approach, all energy operators and a wavefunction are known exactly, unlike the un-known term of the exchange-correlation (XC) operator, which is the main problem of this theorem. Even though the XC energy is less than 10% of the total energy, it involves identifying materials properties. There are many attentions to propose the approximation of this energy term as a function of electron density. The XC energy can be treated to be local functionals of electron density in spherical three-dimensions. The local XC energy per electron can be written as the follow

$$\varepsilon_{xc}[\rho(\vec{r})] = \frac{1}{2} \int \frac{\rho_{xc}(\vec{r}, \vec{r}')}{|\vec{r} - \vec{r}'|} d\vec{r}'\quad (2.23)$$

Then the common XC energy functional is the combination over the whole space of electron density, multiplied by the $\varepsilon_{xc}[\rho(\vec{r})]$:

$$E_{XC}[\rho(\vec{r})] = \int \rho(\vec{r}) \varepsilon_{XC}(\vec{r}, \rho) d\vec{r} \quad (2.24)$$

Recently, there are two most popular XC functionals that have been used, including the local density approximation (LDA) and the generalized gradient approximation (GGA). For the LDA, it can be the exact form for homogeneous electron gas. The XC energy of the LDA can be written as

$$E_{XC}^{LDA}[\rho(\vec{r})] = \int \rho(\vec{r}) \varepsilon_{XC}^{LDA}[\rho(\vec{r})] d\vec{r} \quad (2.25)$$

However, this XC energy functional cannot be applied well for the real system due to the inhomogeneous behavior. To obtain more accurate XC energy functionals, GGA corrected this inhomogeneous character with general formula, regarded the density gradient as a follow:

$$E_{XC}^{GGA}[\rho(\vec{r})] = \int \rho(\vec{r}) \varepsilon_{XC}^{GGA}[\rho(\vec{r}), \nabla\rho(\vec{r})] d\vec{r} \quad (2.26)$$

This $E_{XC}^{GGA}[\rho(\vec{r})]$ is different from $E_{XC}^{LDA}[\rho(\vec{r})]$ because it is no simple functional form. Many different forms of GGA functionals have been proposed and widely used, including PW91, Perdew and Wang 1992 (John P Perdew *et al.*, 1992), and the PBE, Perdew, Burke, and Ernzerhof, 1996 (John P. Perdew *et al.*, 1996). In this thesis, we focused on the PBE functional which its XC energy density can be written as

$$\varepsilon_{XC}^{PBE}[\rho(\vec{r}), \nabla\rho(\vec{r})] = -\frac{3}{4} \left(\frac{3}{\pi} \right)^{\frac{1}{3}} n^{\frac{1}{3}}(\vec{r}) F(x) \quad (2.27)$$

where

$$F(x) = 1 + a \frac{x}{1 + bx^2}, \quad x = \frac{|\nabla\rho(\vec{r})|}{n^{\frac{4}{3}}(\vec{r})} \quad (a \text{ and } b \text{ are constant})$$

The energy density in Eq. 2.27 can be substituted in Ec. 2.26 to get the XC energy functional, $E_{XC}^{PBE}[\rho(\vec{r})]$, then the corresponding XC potential of PBE is

$$V_{XC}^{PBE}[\rho(\vec{r})] = \frac{\delta E_{XC}^{PBE}[\rho(\vec{r})]}{\delta\rho(\vec{r})} \quad (2.28)$$

2.3.5 Wavefunction and pseudopotential

The pseudopotential (PP) approach was proposed by Heine in 1970 for classifying electrons in the system. The materials normally consist of large-thousand electrons, leading to difficult and complicate calculation for DFT. The PP approach is

able to manage this problem by classifying electrons into two groups, including core electrons and valence electrons. The core electrons are generally the electrons in the inner shells closed to the nucleus. Such core electrons stay in deep potential and static under all transitions. For the valence electrons, they are the electrons staying away from the nucleus, which have abilities for bond formation, electric construction, and ionization. We might simply remove the less-influent core electrons and consider only the likely-free valence electrons. This approach is called frozen-core approximation.

We investigated the wavefunction and potential energy of two systems, where the first one considers all electrons (core and valence electrons) in the system while the second one considers only valence electrons. Therefore, we obtain the all electron wavefunction, $\psi_i^{AE}(\vec{r})$, and all electron potential, $\hat{V}^{AE}[\rho(\vec{r})]$. On the other hand, for the second system, we receive the pseudo-wavefunction, $\psi_i^{PP}(\vec{r})$, and pseudopotential, $\hat{V}^{PP}[\rho(\vec{r})]$. Thus, the Kohn-Sham equation can be written, based on the PP approach as

$$\left[-\frac{1}{2}\nabla^2 + \hat{V}^{PP}[\rho(\vec{r})] \right] \psi_i^{PP}(\vec{r}) = \epsilon_i \psi_i^{PP}(\vec{r}) \quad (2.29)$$

Figure 2.1 illustrates a pseudo wavefunction and all electron wavefunction with their corresponding pseudo- and all-electron potentials. The suitable $\psi_i^{PP}(\vec{r})$ has to meet the definitions as follows:

- The proper r_c (the cutoff distance) of the atom must be appropriate and make core part ($r < r_c$) which is similar between the all- and pseudo-wavefunction.
- The eigenfunction of all electron wavefunction and pseudo wavefunction must be the same.
- The pseudo wavefunction and pseudopotential must be smooth with all electron wavefunction and all electron potential at $r = r_c$.
- Net charges are not unchanged into the sphere at the radial r_c .

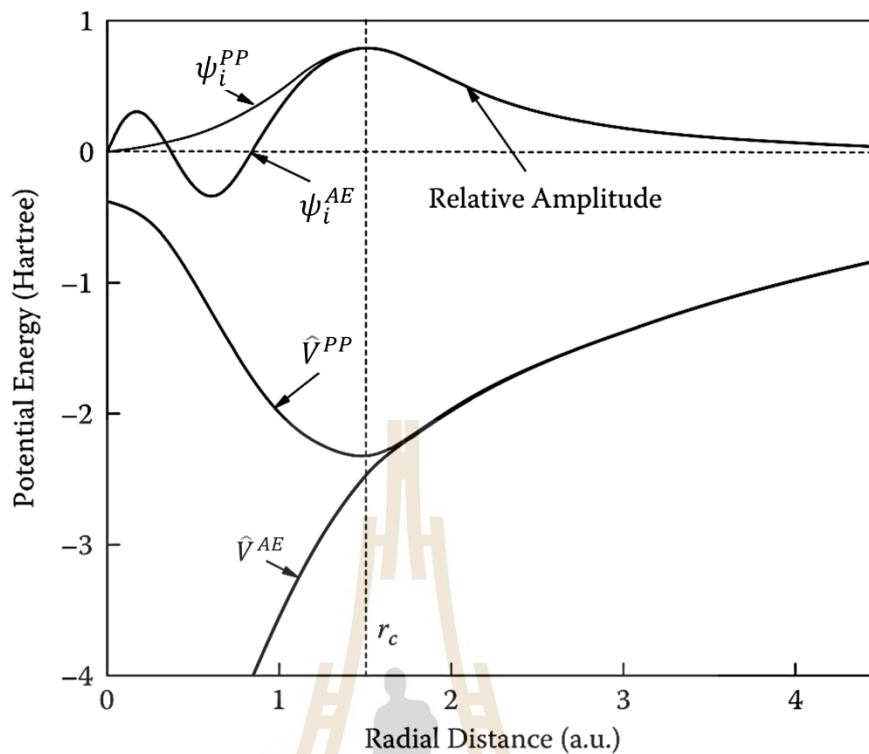


Figure 2.1 Schematic of pseudo wavefunction and the corresponding potential compared with those of all electron wavefunction and its potential (Modified from (Lee, 2016)).

2.3.6 Self-Consistent Field approach

In the DFT, the calculation of solution is interrelated during electron densities, Kohn-Sham approach, and Kohn-Sham Hamiltonian. The electron densities are calculated by the Kohn-Sham orbitals. Afterward, the electron densities will calculate the Kohn-Sham Hamiltonian, followed by the calculation of new electron densities and new Kohn-Sham orbital using Kohn-Sham Hamiltonian, and so on. This cycle is called self-consistency. We must search Kohn-Sham orbitals, bringing to a Kohn-Sham Hamiltonian to obtain new electron densities. Repeating all steps continues until receiving the appropriate Kohn-Sham orbitals. Figure 2.2 shows the flowchart of self-consistency.

- Construct the initial electron density and calculate the exchange-correlation energy.

- Calculate the effective potential operators to obtain Kohn-Sham Hamiltonian.
- Solve the Kohn-Sham equation by substituting the effective potential to obtain the Kohn-Sham orbitals and eigenvalues.
- Use the new Kohn-Sham orbitals to calculate the new electron densities
- Stop iteration when the energy change and electron density value become less than a stopping criterion.
- Use the suitable electron densities to calculate force and update position to obtain the minimized total energy for further calculation of materials properties.

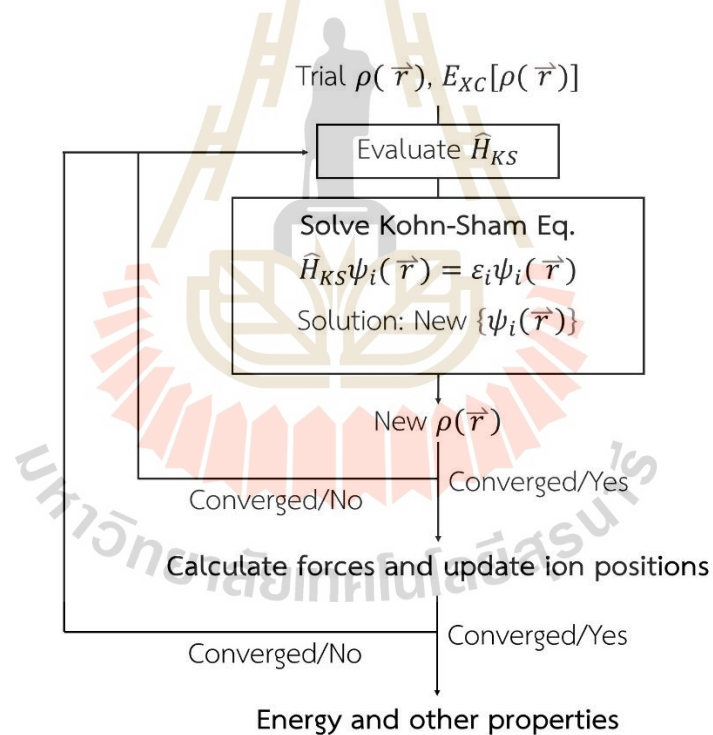


Figure 2.2 The scheme of self-consistency iteration for solving the Kohn-Sham equation and obtaining the calculated total energy and other properties (Modified from (Lee, 2016)).

2.4 Climbing image nudged elastic band (CI-NEB) method

The nudged elastic band (NEB) is a method to find the minimum energy path (MEP) and the corresponding barrier energy during the initial and final states of interest, where both initial and final states must optimize to get the relaxed configurations. The initial band (image) nudges along the MEP toward the saddle points, appearing energy barrier.

The NEB approach is performed by considering a force projection to bring the images toward the MEP, consisting of the saddle points. There are the involved forces between saddle points, including spring and interatomic forces, projected along the band. The DFT method help to find the MEP with the electronic minimization, where the lower-force direction is inducted by the electronic minimization from DFT calculation for the next nudging.

The CI-NEB (Henkelman *et al.*, 2000) is determined to ensure that one of images located in the highest activation energy barrier, i_{\max} , examined, where the force on this image is given by

$$\begin{aligned} F_{i_{\max}} &= -\nabla E(R_{i_{\max}}) + 2\nabla E(R_{i_{\max}}) \Big|_{\parallel} \\ &= -\nabla E(R_{i_{\max}}) + 2\nabla E(R_{i_{\max}}) \cdot \hat{\tau}_{i_{\max}} \hat{\tau}_{i_{\max}} \end{aligned} \quad (2.30)$$

2.5 Ab initio molecular dynamic simulation

Ab initio molecular dynamic (AIMD) is a method applying the combination between quantum mechanics and classical molecular dynamic. In resent, quantum molecular dynamics are categorized into two types, including Born-Oppenheimer molecular dynamics (BOMD) and Car-Parinello molecular dynamics (CPMD), which can be described as following

2.5.1 Born-Oppenheimer molecular dynamics (BOMD)

BOMD is generally proposed by considering the classical molecular dynamics (CMD) and density functional theory (DFT) in which this technique uses an interacting

force between ions calculated from DFT, as mentioned in section 2.3.6. The calculated force from DFT provides an accuracy more significantly than that from CMD, based on Newton's law. The calculated force from DFT is brought to calculate relevant parameters, including position $\vec{R}(t)$, velocity $\vec{v}(t)$, and acceleration $\vec{a}(t)$ of atoms in a system, where can be calculated from velocity-Verlet algorithm (VVA) (Swope *et al.*, 1982) as following

$$\begin{aligned}\vec{R}(t + \Delta t) &= \vec{R}(t) + \vec{v}(t)\Delta t + \frac{1}{2}\vec{a}(t)\Delta t^2 \\ \vec{v}(t + \Delta t) &= \frac{\vec{F}}{m} = -\frac{\nabla V(\vec{R}(t + \Delta t))}{m} \\ \vec{a}(t + \Delta t) &= \vec{v}(t) + \frac{1}{2}(\vec{a}(t) + \vec{a}(t + \Delta t))\Delta t\end{aligned}\quad (2.31)$$

To solve the above equations, we have first to know initial condition, i.e., $\vec{R}(0)$, $\vec{v}(0)$ and $\vec{a}(0)$. In the case of solid material, $\vec{R}(0)$ is an initial position of each atom, while initial velocity is involved with thermal energy as shown below

$$\frac{1}{2}m\vec{v}(0) = \frac{3}{2}k_B T \quad (2.32)$$

where k_B is Boltzmann's constant (1.38×10^{-23} J/K). From Eq. 2.32, $\vec{v}(0)$ of all atoms does not define directly because it can be represented by temperature, while $\vec{a}(0)$ is guessed for an initial value.

2.5.2 Car-Parinello molecular dynamics (CPMD)

The calculation of BOMD is classified into two steps. Firstly, an interacting force between atoms is calculated from DFT which involves with only electrons in the system. Finally, such a force becomes an input to solve the equation of motion in Eq. 2.31, which involves with only atoms or ions in the system. On the other word, there is separation of calculation steps obviously between in term of electrons and in term of ions, which spends more time to finish each step. Therefore, CPMD method helps to reduce the calculation time, which aggregates both steps into one step.

For CPMD, the Lagrangian of any system, consisting of N ions and N_e electrons, can be written as

$$L = \frac{1}{2} \sum_{I=1}^{3N} M_I \dot{\vec{R}}_I^2 + \frac{1}{2} \sum_{i=1}^{N_e} (2\mu) |\dot{\psi}_i(\vec{r})|^2 - E[\psi_i(\vec{r}), \vec{R}] + \sum_{i,j=1}^{N_e} \Lambda_{ij} \left[\int \psi_i^*(\vec{r}) \psi_j(\vec{r}) d\vec{r} - \delta_{ij} \right] \quad (2.33)$$

where μ is fictitious electron mass, Λ_{ij} is Lagrange multiplier, and δ_{ij} is Kronecker delta which is equal to 1 for $i = j$ and is equal to zero for $i \neq j$. From Eq. 2.33, the first term of the right hand side is kinetic energy of ions, while the second term is kinetic energy of electrons, the third is the total energy calculated from DFT, and the final term is an energy calculated from Kohn-Sham orbitals with orthogonal properties.

The equations of motion related to this Lagrangian (Martin, 2020) can be written as

$$\mu \ddot{\psi}_i(\vec{r}, t) = - \frac{\delta E}{\delta \psi_i^*} + \sum_{j=1}^{N_e} \Lambda_{ij} \psi_j(\vec{r}, t) \quad (2.34)$$

$$M_I \ddot{\vec{R}}_I = \vec{F}_I = - \frac{\delta E}{\delta \vec{R}_I} \quad (2.35)$$

where both above equations are obtained from solving Newton's law, which can find solution using Verlet integration (Martin, 2020; Swope *et al.*, 1982), where Kohn-Sham orbital and position of atoms as a function of time (Martin, 2020) can be respectively represented as

$$\psi_i(\vec{r}, t + \Delta t) = 2\psi_i(\vec{r}, t) - \psi_i(\vec{r}, t - \Delta t) - \frac{(\Delta t)^2}{\mu} \left[\hat{H} \psi_i(\vec{r}, t) - \sum_{j=1}^{N_e} \Lambda_{ij} \psi_j(\vec{r}, t) \right] \quad (2.36)$$

$$\vec{R}_I(t + \Delta t) = 2\vec{R}_I(t) - \vec{R}_I(t - \Delta t) + \frac{(\Delta t)^2}{M_I} \vec{F} \quad (2.37)$$

2.6 Summary of computational details

All calculations were carried out using the spin polarized DFT method as implemented in the Vienna ab initio Simulation Package (VASP 5.3) (Kresse *et al.*, 1996a, 1996b). The frozen-core projector augmented wave method was used to describe the electron-ion interaction (Blöchl, 1994). The valence electrons of Li 2s, C 2s2p, N 2s2p, S 3s3p, Co 3d4s, and Fe 3d4s were taken into account in a plane wave basis with a kinetic energy cutoff of 600 eV. The exchange-correlation functional was described by the generalized gradient approximation of Perdew-Burke-Ernzerhof (PBE) (John P. Perdew *et al.*, 1996). Weak Van der Waals interactions between the adsorbates (S_8 , Li_2S_x) and the substrates (GDY, $TMN_x@GDY$) were partially corrected using the DFT-D3 method with Becke-Jonson damping (Grimme *et al.*, 2010; Grimme *et al.*, 2011). To avoid interaction between periodic images, the unit cell of GDY was expanded to a 2 × 2 supercell with a vacuum gap of 20 Å along the z-direction. The 2 × 2 supercell is large enough to avoid spurious interaction between adsorbates in their periodic images as the difference of the adsorption energies calculated using the expanded 3 × 3 supercell is within 0.01 eV. The Brillouin zone integrations were carried out using the k-point sampling of Monkhorst-Pack scheme (Monkhorst *et al.*, 1976) as 3 × 3 × 1 for structural optimization and 7 × 7 × 1 for electronic density of states (DOS) calculations. The ground-state energies were obtained by solving Kohn-Sham equation self-consistently until the energy difference was within 10^{-6} eV. For structural optimization, the force convergence criterion was set to 0.02 eV Å⁻¹. The charge distributions were analyzed using Bader charge decomposition scheme (Tang *et al.*, 2009).

2.7 References

- Blöchl, P. E. (1994). Projector augmented-wave method. *Physical Review B*. 50: 17953.
- Born, M., and Oppenheimer, J. (1927). 1. Zur Quantentheorie der Molekeln. *Annalen der Physik*. 389: 457.
- Cederbaum, L. S. (2008). Born–Oppenheimer approximation and beyond for time-dependent electronic processes. *The Journal of chemical physics*. 128: 124101.

- Fock, V. (1930). Näherungsmethode zur Lösung des quantenmechanischen Mehrkörperproblems. *Zeitschrift für Physik*. 61: 126.
- Grimme, S., Antony, J., Ehrlich, S., and Krieg, H. (2010). A consistent and accurate ab initio parametrization of density functional dispersion correction (DFT-D) for the 94 elements H-Pu. *The Journal of Chemical Physics*. 132: 154104.
- Grimme, S., Ehrlich, S., and Goerigk, L. (2011). Effect of the damping function in dispersion corrected density functional theory. *Journal of Computational Chemistry*. 32: 1456.
- Hartree, D. R. (1928). *The wave mechanics of an atom with a non-Coulomb central field. Part I. Theory and methods*. Paper presented at the Mathematical Proceedings of the Cambridge Philosophical Society.
- Henkelman, G., Uberuaga, B. P., and Jónsson, H. (2000). A climbing image nudged elastic band method for finding saddle points and minimum energy paths. *The Journal of Chemical Physics*. 113: 9901.
- Hohenberg, P., and Kohn, W. (1964). Inhomogeneous electron gas. *Physical review*. 136: B864.
- Kohn, W., and Sham, L. J. (1965). Self-consistent equations including exchange and correlation effects. *Physical review*. 140: A1133.
- Kresse, G., and Furthmüller, J. (1996a). Efficiency of ab-initio total energy calculations for metals and semiconductors using a plane-wave basis set. *Computational Materials Science*. 6: 15.
- Kresse, G., and Furthmüller, J. (1996b). Efficient iterative schemes for ab initio total-energy calculations using a plane-wave basis set. *Physical Review B*. 54: 11169.
- Lee, J. G. (2016). *Computational materials science: an introduction*: CRC press.
- Martin, R. M. (2020). *Electronic structure: basic theory and practical methods*: Cambridge university press.
- Monkhorst, H. J., and Pack, J. D. (1976). Special points for Brillouin-zone integrations. *Physical Review B*. 13: 5188.
- Perdew, J. P., Burke, K., and Ernzerhof, M. (1996). Generalized Gradient Approximation Made Simple. *Physical Review Letters*. 77: 3865.

Perdew, J. P., and Wang, Y. (1992). Accurate and simple analytic representation of the electron-gas correlation energy. *Physical review B*. 45: 13244.

Slater, J. C. (1930). Note on Hartree's method. *Physical Review*. 35: 210.

Swope, W. C., Andersen, H. C., Berens, P. H., and Wilson, K. R. (1982). A computer simulation method for the calculation of equilibrium constants for the formation of physical clusters of molecules: Application to small water clusters. *The Journal of chemical physics*. 76: 637.

Tang, W., Sanville, E., and Henkelman, G. (2009). A grid-based Bader analysis algorithm without lattice bias. *Journal of Physics: Condensed Matter*. 21: 084204.



CHAPTER III

STRUCTURAL AND ELECTRONIC PROPERTIES

Before exploring the role of the GDY substrates for Li-S batteries, we first investigated the atomistic structures and the electronic properties of pristine and co-doped GDY. Here, we chose the GDY monolayer as the substrate model to study in this work. The structural and electronic properties of pristine GDY were discussed in section 3.1. Although transition metal and nitrogen co-doping on GDY have been successfully fabricated in the experiment, the doped GDY structures are still unclear. They have not been determined yet at the molecular level. To better understand comprehensively, the computations were utilized to find possible structural configurations of favorable doping sites of the doped transition metal (Co and Fe) and nitrogen dopants. The computational investigations, including co-doped configurations, electronic structures, and charge distributions, were explained in section 3.2.

3.1 Pristine graphdiyne monolayer

3.1.1 Geometric structure

Single-layer GDY belongs to the hexagonal lattice with the P6/mmm space group. A unit cell of monolayer GDY consisted of 18 carbon atoms, including one benzene ring and three diacetylenic linkages ($-\text{C}\equiv\text{C}-\text{C}\equiv\text{C}-$) connecting neighboring rings. The calculated lattice parameters of GDY unit cell are $a = b = 3.455 \text{ \AA}$, $\alpha = \beta = 90^\circ$ and $\gamma = 120^\circ$, which is in good agreement with the experimentally measured value of 9.458 \AA and the computationally calculated report of 9.46 \AA with DFT-PBE calculation (Luo *et al.*, 2013). To study the adsorption of the molecules on the substrates, the GDY unit cell was expanded to a 2×2 GDY supercell with its expanded lattice constant of 18.92 \AA , which is large enough to avoid self-interaction between neighboring periodic images as the difference of the adsorption energies

calculated using the expanded 3×3 supercell is within 0.01 eV, as shown in Figure 3.1. It should be noted that the theoretical prediction of d-spacings of GDY (100) and GDY (110) planes are 8.21 and 4.74 Å, respectively (Gao *et al.*, 2019). Here, we set the vacuum space along the z-direction with 20 Å. The calculated C–C bond distance in the benzene ring is 1.432 Å, and that in diacetylenic linkages are 1.369 and 1.232 Å which can be categorized as a single and triple C–C bond. Such calculated distances are consistent with previous computational calculations with 1.43, 1.40, and 1.23 Å, respectively (Pei, 2012).

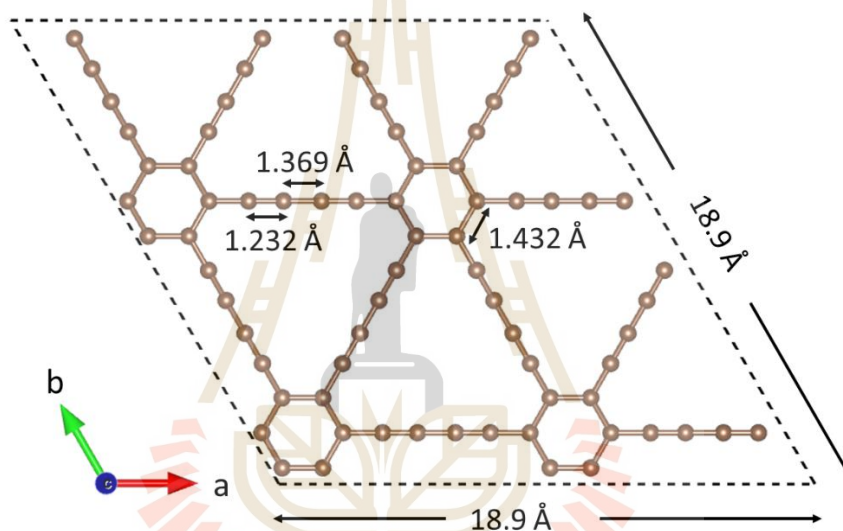


Figure 3.1 Geometric structure of 2×2 GDY supercell with its lattice constant and C–C bond distances.

3.1.2 Electronic properties

The electronic structure of pristine GDY was explained by analyzing the partial density of state (PDOS), as shown in Figure 3.2a. Our computations reveal that monolayer GDY possesses the narrow band gap of 0.47 eV, which can be classified as a semiconductor material. Such value is consistent with the previous first-principles calculation (DFT-PBE) with the band gap of 0.47 eV (Li *et al.*, 2014). It should be noted that the calculated band gap is underestimated lower than the measured band gap (0.6 – 1.0 eV) of the experimental study (Ketabi *et al.*, 2017) because of the well-known self-interaction error in DFT calculation that does not include the

intrinsic energy from many-body electron interaction. The PDOS shows that C 2p orbitals are dominant near the valence band maximum (VBM) and the conduction band minimum (CBM), where the C $2p_z$ hybridized carbon atom locates at the Fermi level. This implies that the major change in electronic features and optical properties of pristine GDY are governed by C $2p_z$ orbitals.

The electronic band structure of monolayer GDY is shown in Figure 3.2b. It indicates the direct band gap at the gamma point of the first Brillouin zone. The highly dispersive band edge position, especially around gamma point (Γ), provides the light-effective mass of charge carriers (i.e., electrons and holes), leading to rapid electronic transport. It should be noted that the electronic structure obtained by DFT calculation cannot accurately obtain the transport property of materials. However, the calculated band structure affects the calculation of effective mass and charge carrier mobility. The effective mass is calculated as following equation,

$$\frac{1}{m^*} = \frac{2E(k)}{\hbar^2 k^2} \quad (3.1)$$

where $E(k)$ is the energy of an electron at k point, \hbar is the Planck's constant 6.58×10^{-16} eV s. The previous DFT-PBE reports the effective mass of GDY material (Long *et al.*, 2011; Pei, 2012). They suggested that the effective mass in the conduction band (m_c^*) and valence band (m_v^*) is symmetrically equal in the same direction, where such effective mass along M - Γ and K - Γ directions is $0.077m_0$ and $0.080 m_0$, respectively, where m_0 is the mass of single electron.

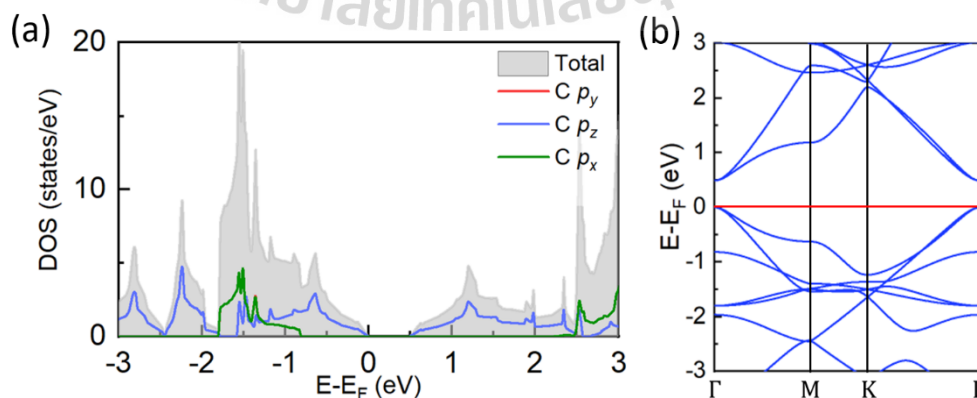


Figure 3.2 (a) Projected density of state (PDOS) of pristine GDY and (b) corresponding electronic band structure.

3.2 Transition metal and nitrogen co-doped graphdiyne

3.2.1 Geometric structure

In the experimental preparation of TM and N co-doped GDY, melamine was used as a nitrogen source, whereas $\text{Co}(\text{NO}_3)_2 \cdot 6\text{H}_2\text{O}$ and $\text{FeCl}_3 \cdot 6\text{H}_2\text{O}$ were used as Co and Fe sources, respectively, for doping on GDY structure. The mixtures were calcined at a high temperature of around 400 – 900 °C under an argon gas environment. The results of characterization using the X-Ray photoelectron spectrometer (XPS) technique show the successful substitution of N and TM atoms deposited on GDY sheet with the concentration of N atom in the range of 2.99 – 5.39 at. % and that of TM atom at least 0.47 at. %, see more details in (Wang *et al.*, 2019) and (Si *et al.*, 2019). Although the number of TM content was small, XPS spectra confirmed in the fact that both Co and Fe atoms form the chemical bond with the substrate nearby N atom sites.

Here, in computation, the possible configurations of the TM and N co-doped GDY were explored where a single TM atom was added, and the number of N atoms was varied from 2 to 4 atoms with concentrations of 2.78 – 5.56 at. % that close to the experimental concentrations. To obtain the most stable of the co-doped substrates, the thermodynamic stability was analyzed by calculating the formation energy (E_f) of each configuration which was calculated as the following equation,

$$E_f = E(\text{TM} + \text{N}_x @ \text{GDY}) - \frac{x}{2} E(\text{N}_2) - E(\text{TM}) - E(\text{GDY}) + xE(\text{C}) \quad (3.2)$$

where $E(\text{TM} + \text{N}_x @ \text{GDY})$ represents the total energy of co-doped GDY with TM atom (TM = Co or Fe) and x N atoms, $E(\text{N}_2)$ is the total energy of isolated nitrogen gas, $E(\text{TM})$ is the total energy of a single metal atom, $E(\text{GDY})$ is the total energy of perfect GDY, and $E(\text{C})$ is the total energy per carbon atom of perfect GDY. It should be noted that a lower E_f value means higher thermodynamic stability.

Three different N substituted at C atom sites on monolayer GDY, including two C sites on diacetylenic linkages, and one C site on the benzene doping sites are ring. However, N doping on the benzene ring is unstable due to the high energy barrier of formation. Therefore, in this thesis, we considered the N substitutions on the linkages, and a single TM atom was trapped near the doped N position on the N-

doped GDY. The formation energies and corresponding co-doped configurations are illustrated in Figure 3.3, where the E_F value is shown in parentheses. The concentrations of N doping are 2.78%, 4.17%, and 5.56% for 2, 3, and 4 doped N atoms on GDY. The formation energy calculation reveals that the $\text{CoN}_2@GDY$ and $\text{FeN}_2@GDY$ are the most stable configuration with the lowest formation energy of -2.41 eV and -2.00 eV, respectively. The other structures are significantly less stable where their formation energies are more at least 0.32 eV compared to the most stable configurations.

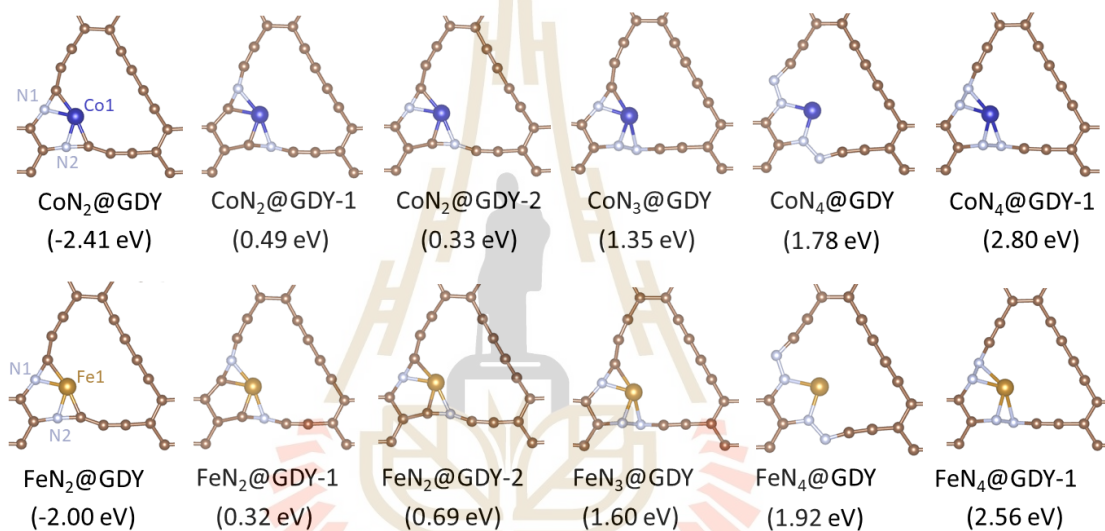


Figure 3.3 The possible configuration of the transition metal and nitrogen co-doped GDY. Note that the corresponding formation energy of each configuration is shown in parentheses. C, N, Co, and Fe atoms are represented by brown, grey, blue, and gold, respectively.

Furthermore, to confirm the stability of TM adsorption on N-doped GDY, we assessed the adsorption strength ($E_{ads, TM}$) of adsorbed TM atom in $\text{CoN}_2@GDY$ and $\text{FeN}_2@GDY$ substrate using the following equation,

$$E_{ads, TM} = E(TM N_2 @ GDY) - E(N_2 @ GDY) - E(TM) \quad (3.3)$$

where $E(TM N_2 @ GDY)$, $E(N_2 @ GDY)$, and $E(TM)$ denote the total energy of TM adsorbed $N_2@GDY$ monolayer, N-doped GDY, and isolated Co or Fe atom ($TM = \text{Co}$ or Fe), respectively, as shown in Table 3.1. The finding indicates that $N_2@GDY$ provides effectively chemical interaction to the trapped TM atom with the adsorption energy

of -6.64 eV and -8.94 eV for Co and Fe adsorbed on N₂@GDY, respectively. The average distance of the TM-N bond is 1.82 Å, while that of TM and the nearest C atom is 1.86 Å, and both values can be categorized as a covalent bond. This suggests that CoN₂@GDY and FeN₂@GDY systems are suitable for this study's substrate models.

We further examined the thermal stability of the chosen doped models using AIMD simulation with NVT ensemble at 300 K for 10 ps. The k-point sampling was decreased to 2×2×1 for the reduced computations. As shown in Figure 3.4, the AIMD simulation suggests that the doped GDY are still intact, where the adsorbed TM atom vibrates weakly around their equilibrium position without ejection. The comparative energy profiles show small changes, and the structures are not decomposed along the AIMD simulation time.

Table 3.1 Formation energy (E_f), Adsorption energy of M atom (E_{ads}), a bond distance of M-C bond (L_{M-C}), a bond distance of M-N bond (L_{M-N}), charge transfer (Q_M) of M atom to N-GDY.

parameters	CoN ₂ @GDY	FeN ₂ @GDY
E_f (eV)	-2.41	-2.00
E_{ads} (eV)	-6.64	-8.94
L_{M-C} (Å)	1.86	1.86
L_{M-N} (Å)	1.82	1.83
Q_M (e)	-0.61	-0.72

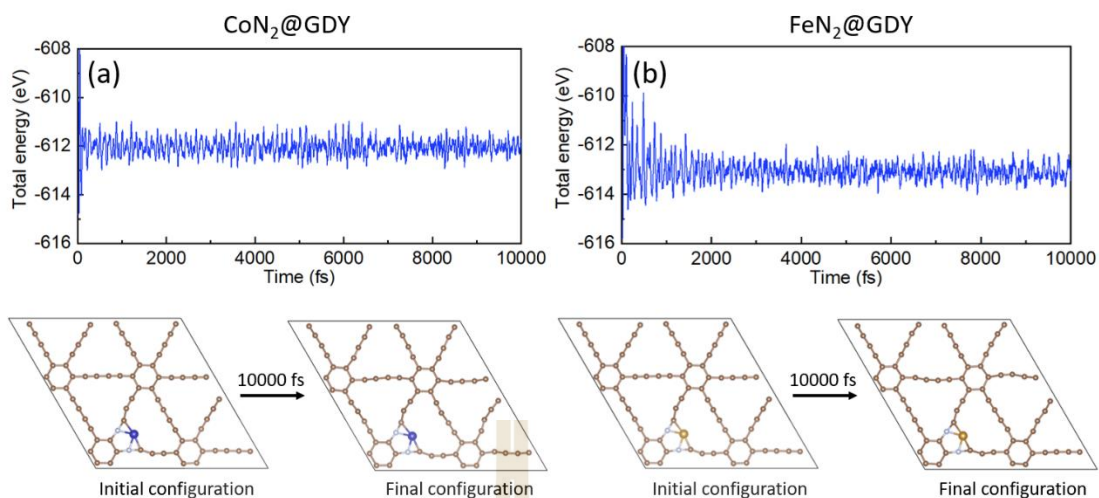


Figure 3.4 The variation of total energy as a function of time along AIMD simulation at 300 K and corresponding initial and final configurations of (a) CoN₂@GDY and (b) FeN₂@GDY.

3.2.2 Electronic properties

Generally, a host cathode material is expected to have good electrical conductivity. A metallic host cathode can effectively provide electron accessibility to contribute to the kinetic redox activities. Here, we analyze the PDOS of the co-doped GDY substrate to reveal the electronic properties change upon doping by Co and Fe impurity atoms. Compared to the PDOS of pristine GDY, PDOS of both co-doped GDY exhibits metallic features with appearing electron states at the Fermi level, as illustrated in Figure 3.5. The Fermi level is shifted to higher energy in the conduction band region because it has additional electrons from TM and N atoms partially occupied in the empty conduction band, which is consistent with the calculated band structure. The PDOS exhibits the strong hybridization between TM 3d states and C 2p states around VBM and CBM, while a small peak of N 2p states also hybridized with TM 3d states suggesting strong chemical interaction between TM-N and TM-C bond. This supports the explanation of the adsorption energy of TM adsorbed on N-doped GDY. In addition, we tested the electronic structure of the doped GDY with the applied Hubbard U correction; we calculated their PDOS using the PBE+U method. The U values for Fe and Co are 5.21 and 6.18 eV, respectively (He *et al.*, 2012). As described in APPENDIX A, these calculated Fe PDOS of Co and Fe

doped $N_2@GDY$ still exhibit a metallic behaviour, allowing us to use only the PBE method studied in this work.

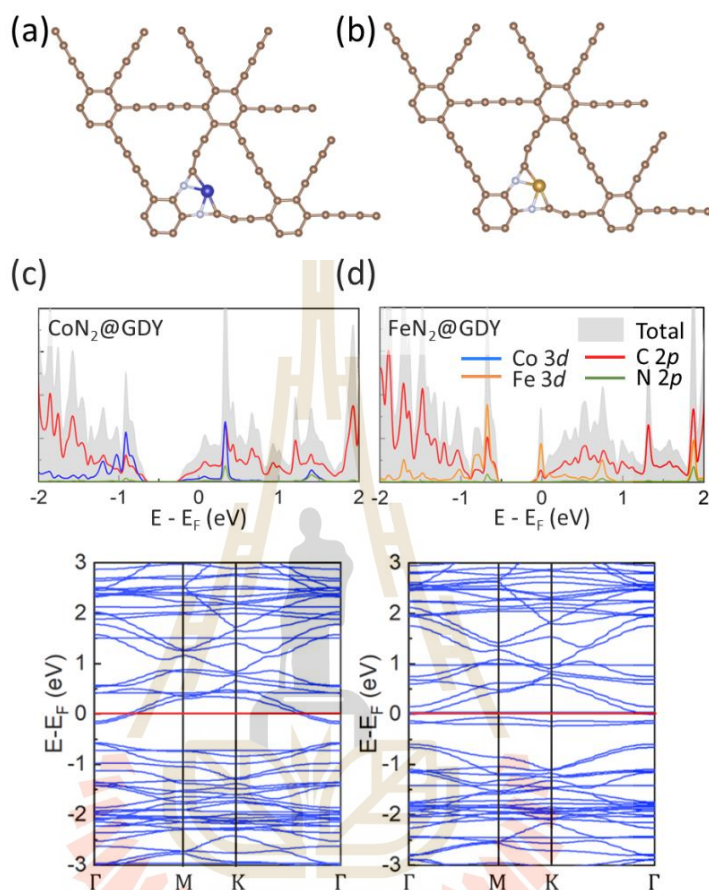


Figure 3.5 Geometric structure of (a) $CoN_2@GDY$ and (b) $FeN_2@GDY$. (c-d) the corresponding projected density of state (PDOS) and band structures of (a) $CoN_2@GDY$ and (b) $FeN_2@GDY$, respectively. Color code: brown; C, white; N, blue; Co, and yellow; Fe.

Moreover, we also consider Bader charge distribution in the co-doped GDY, as shown in Figure 3.6. The result reveals a large amount of electron transfer from the adsorbed Co (0.61 |e|) and Fe (0.72 |e|) to the N-doped GDY. The N atom behaves as the electron acceptor with a large negative charge around -1.21 |e| and -1.23 |e| in $CoN_2@GDY$ and $FeN_2@GDY$ substrate, respectively, whereas TM and the nearest C atom act as an electron donor. The combination between the acceptor and donor atoms at the active site on the substrate may enhance the adsorption strength of

LiPS molecules where the TM atom has a vacant valence orbital to receive an extra electron from a travel molecule (e.g., LiPS molecules). In contrast, the N atom may represent strong the interaction with the lower electronegative atoms. Overall, the electronic behavior of GDY is improved upon doping with TM and N dopants from semiconductors to be metallic, which could facilitate the redox kinetic process of the cathode using the charge and discharge process. Similar effects have been reported in a previous computational work that TM doping increases the conductivity of the C_2N host and improves the redox activity of Li-S batteries.

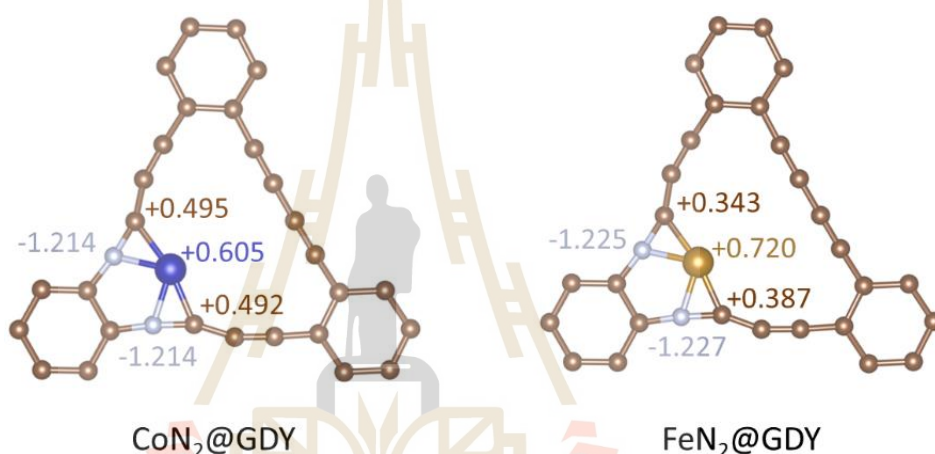
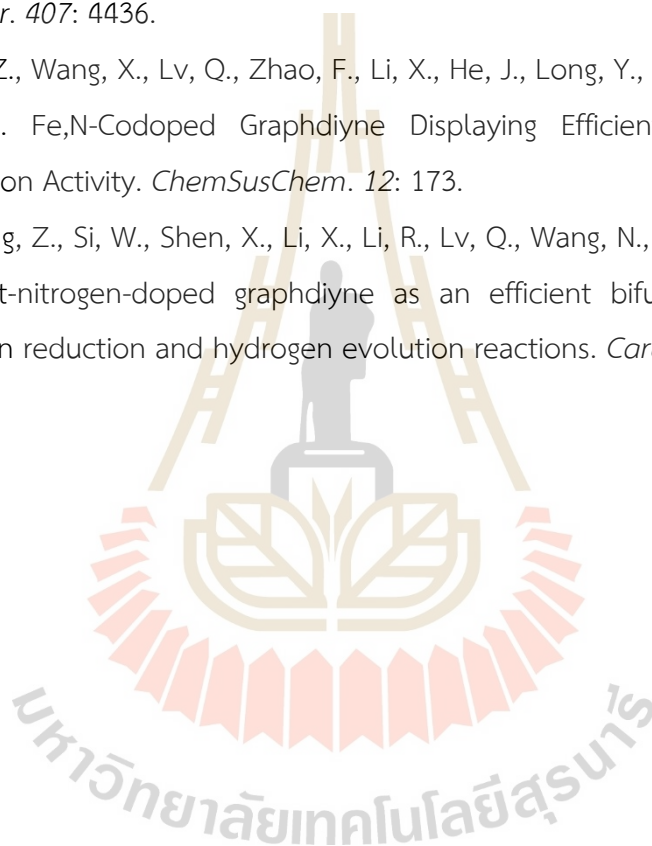


Figure 3.6 The Bader charge distribution of $CoN_2@GDY$ and $FeN_2@GDY$.

3.3 References

- Gao, X., Liu, H., Wang, D., and Zhang, J. (2019). Graphdiyne: synthesis, properties, and applications. *Chemical Society Reviews*. 48: 908.
- He, J., Ma, S. Y., Zhou, P., Zhang, C., He, C., and Sun, L. (2012). Magnetic properties of single transition-metal atom absorbed graphdiyne and graphyne sheet from DFT+ U calculations. *The Journal of Physical Chemistry C*. 116: 26313.
- Ketabi, N., Tolhurst, T. M., Leedahl, B., Liu, H., Li, Y., and Moewes, A. (2017). How functional groups change the electronic structure of graphdiyne: Theory and experiment. *Carbon*. 123: 1.
- Li, Y., Xu, L., Liu, H., and Li, Y. (2014). Graphdiyne and graphyne: from theoretical predictions to practical construction. *Chemical Society Reviews*. 43: 2572.

- Long, M., Tang, L., Wang, D., Li, Y., and Shuai, Z. (2011). Electronic Structure and Carrier Mobility in Graphdiyne Sheet and Nanoribbons: Theoretical Predictions. *ACS Nano*. 5: 2593.
- Luo, G., Zheng, Q., Mei, W.-N., Lu, J., and Nagase, S. (2013). Structural, Electronic, and Optical Properties of Bulk Graphdiyne. *The Journal of Physical Chemistry C*. 117: 13072.
- Pei, Y. (2012). Mechanical properties of graphdiyne sheet. *Physica B: Condensed Matter*. 407: 4436.
- Si, W., Yang, Z., Wang, X., Lv, Q., Zhao, F., Li, X., He, J., Long, Y., Gao, J., and Huang, C. (2019). Fe,N-Codoped Graphdiyne Displaying Efficient Oxygen Reduction Reaction Activity. *ChemSusChem*. 12: 173.
- Wang, X., Yang, Z., Si, W., Shen, X., Li, X., Li, R., Lv, Q., Wang, N., and Huang, C. (2019). Cobalt-nitrogen-doped graphdiyne as an efficient bifunctional catalyst for oxygen reduction and hydrogen evolution reactions. *Carbon*. 147: 9.



CHAPTER IV

ADSORPTIVITY AND SUPPRESSION OF POLYSULFIDE SHUTTTLING

In the previous chapter, we considered the possible configurations of transition metal and nitrogen co-doping on graphdiyne material and investigated their electronic properties. Therefore, the $\text{CoN}_2\text{@GDY}$ and $\text{FeN}_2\text{@GDY}$ are the best co-doped systems to use as substrate models in this study. Next, we further determined the adsorption strength of substrates toward the S_8 and LiPS molecules to explore the role of doped atoms on the suppression of the LiPS shuttling. Firstly, the optimized molecular structures of S_8 , and LiPS are discussed in section 4.1. Secondly, the interaction between the molecules and the substrates is explored by calculating adsorption energies and analyzing Bader charge distribution, as explained in section 4.2. Afterward, corresponding electronic properties upon adsorption are also examined via analyzing PDOS, as discussed in section 4.3. Finally, the prevention of the shuttle effect on the substrates is explored by comparing the adsorption energy of soluble LiPS molecules to the substrates and the binding energy of soluble LiPS molecules to electrolyte molecules in section 4.4.

4.1 Sulfur and lithium polysulfide molecules

Sulfur is a typical molecular crystal, where the orthorhombic α -sulfur is the most stable form at room temperature and standard pressure (Meyer, 1976; Steudel, 1996). In this work, we chose a single S_8 molecule as a basic model representing the most stable sulfur phase to determine the adsorption on the substrate, which is similar to previous DFT calculation that used an S_8 molecule to study as well (Cai, 2020; Wasalathilake *et al.*, 2018; Q. Zhang *et al.*, 2015). The most stable form of sulfur allotrope is a buckled octa-sulfur S_8 ring with a D_{4d} point group symmetry, as shown in Figure 4.1. The calculated bond distance of the S-S bond is 2.06 Å, and the S-S-S angle in the S_8 molecule is 109.42°, which is consistent with previous DFT-

B3LYP computation with S-S bond and the angle of 2.07 and 108.9°, respectively (Wang *et al.*, 2013). Other analysis reveals the various low index surface in S_8 crystal providing the information that S_8 (100) is the surface orientation with the lowest formation energy of 11 meV/Å², which the intermolecular interactions in S_8 crystal are van der Waals with no broken cycloocta ring (Arneson *et al.*, 2018).

Figure 4.1 illustrates the optimized geometry structure of several LiPS species, Li_2S_x where $x = 1, 2, 4, 6,$ and 8 . The Li_2S_8 and Li_2S_6 molecules are respectively, the first and second products of the redox reduction reaction, which forms to be a cluster ring, while Li_2S_4 has a C_1 symmetry with an appearing three-ring structure. Previous computation suggested that the large LiPSs ($Li_2S_4, Li_2S_6, Li_2S_8$) prefer forming a 3D-spherical structure instead of a 1D-long chain due to higher stability (Wang *et al.*, 2013). Meanwhile, Li_2S_2 is a tridimensional monocyclic ring with C_5 symmetry. The Li_2S is the final product of the discharge process which is the most stable structure with C_{2v} symmetry. The corresponding bond distance and the angle are illustrated in Table 4.1. The S-S bond lengths tend to increase, whereas those of Li-S bond decrease with increasing Li/S ratio. Overall, our optimized structures of S_8 and LiPS molecules are in good agreement with previous calculations (Cai, 2020; X. Liu *et al.*, 2018; D. Wang *et al.*, 2019).

Table 4.1 Geometric parameters of optimized LiPS species.

LiPSs	S-S bond (Å)	Li-S bond (Å)	Li-S-Li angle (°)
S_8	2.06	-	-
Li_2S_8	2.01-2.17	2.38-2.66	69.68
Li_2S_6	2.6-2.10	2.33-2.39	68.87
Li_2S_4	2.08-2.11	2.34-2.38	73.23
Li_2S_2	2.19	2.22	95.60
Li_2S	-	2.08	126.36

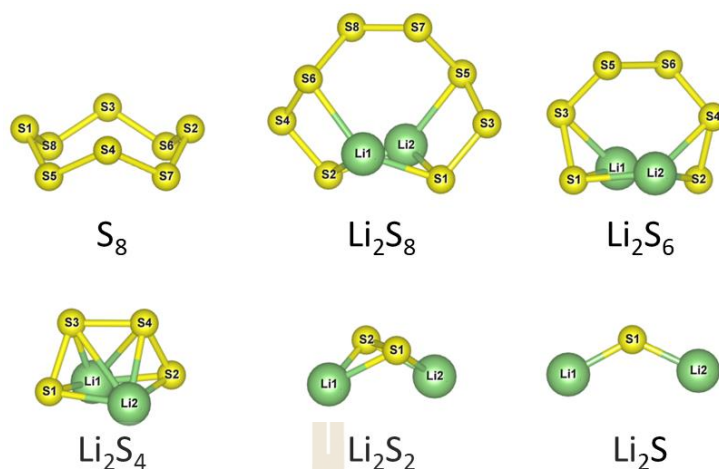


Figure 4.1 The relaxed molecular structures of S_8 and LiPS species. Li and S atoms are represented by green and yellow spheres, respectively.

4.2 Adsorptivity on pristine and doped substrates

The adsorption strength between the molecules and the GDY substrate is basically expected to be moderate in the range of 1 eV to 4 eV (L. Zhang *et al.*, 2018). The weak interaction cannot confine LiPS products on the cathode, resulting in the dissolution into a liquid solvent. In contrast, the too-strong interaction prevents the further spontaneous process of the kinetic redox reaction. To assess the anchoring effect, we explored the interfacial binding between them adsorbents and the substrates. We searched for the energetically preferential adsorption sites, regarding various possibility of the available positions on the substrate such as bridge, top, and hollow sites. Subsequently, the adsorption energy, E_{ads} , was calculated as follows equation (Lin *et al.*, 2019), to qualify the interaction strength,

$$E_{ads} = E(S_8 / Li_2 S_x + sub) - E(sub) - E(S_8 / Li_2 S_x) \quad (4.1)$$

where $E(S_8/Li_2S_x+sub)$ means the total energy of the adsorbed S_8/Li_2S_x systems, $E(sub)$ is the total energy of the substrate, and $E(S_8/Li_2S_x)$ is the total energy of an isolated S_8/Li_2S_x molecule, $x = 1, 2, 4, 6,$ and 8 . It should be noted that the more negative E_{ads} mean stronger adsorption strength.

Using Bader charge calculation, we also calculated the degree of charge transfer (Δq) between the molecules and the substrate by as the following equation,

$$\Delta q = q(\text{adsorbed}_{S_8/Li_2S_x}) - q(\text{isolated}_{S_8/Li_2S_x}) \quad (4.2)$$

where $q(\text{adsorbed}_{S_8/Li_2S_x})$ and $q(\text{isolated}_{S_8/Li_2S_x})$ denote the total Bader charge of S_8/Li_2S_x ($x = 1, 2, 4, 6, 8$) after and before adsorption on substrates, respectively. The negative value indicates that the electrons transfer from the adsorbate to cathode material, whereas the positive one is the opposite. The correlation between adsorption energies and degree of charge transfer are shown in Figure 4.2.

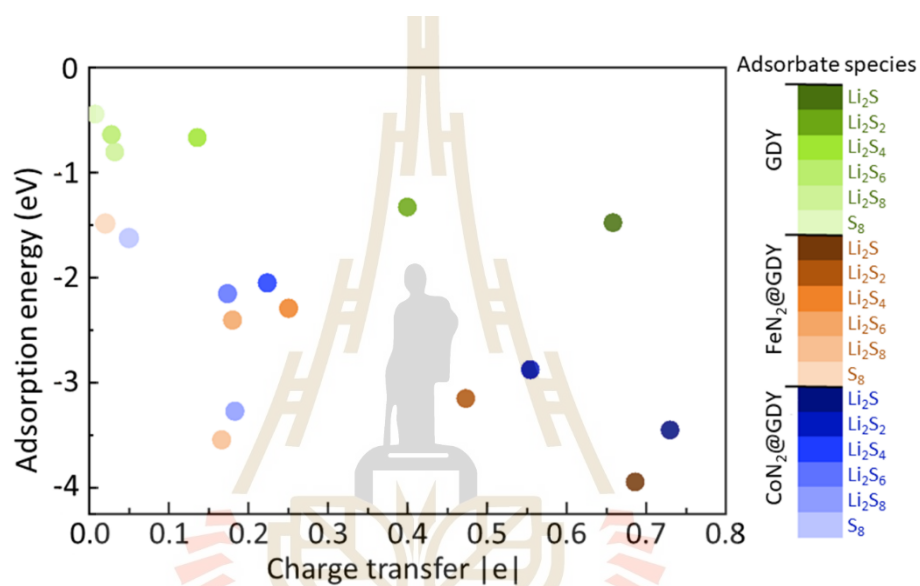


Figure 4.2 Correlation between $S_8/LiPSs$ adsorption energy and degree of charge transfer to substrate. The adsorbate species are represented as color gradient where these adsorbates adsorbed on pristine GDY (green color), $CoN_2@GDY$ (blue color), and $FeN_2@GDY$ (orange color).

To begin with the adsorption on pristine GDY, the optimized adsorption configurations of the $S_8/LiPS$ adsorbed on GDY substrate are shown in Figure 4.3a. We find that the most preferential adsorption site of the molecules is at the hollow site of the large triangle pore. The adsorption energy of S_8 molecule is -0.44 eV where its molecular orientation is horizontal to the GDY plane with an equilibrium distance of 3.52 Å. It implies the weak adsorption associated with van der Waals interaction suggesting that pristine GDY maybe not good accommodation for surfer cathode. For $LiPSs$ adsorption, the large $LiPS$ molecules were adsorbed by the adsorption energy

of -0.84 and -0.64 eV for the Li_2S_8 and Li_2S_6 , respectively. Meanwhile, a smaller LiPS size, Li_2S_4 provides a slightly higher binding of -0.67 eV. Such LiPS adsorption strengths are intrinsically classified as physisorption due to higher value than -1 eV, where the binding orientations are horizontal adsorption with a single Li atom in LiPS toward the GDY substrate. Compared to other 2D-carbon substrates, the large LiPS adsorbed on pristine graphene provides the E_{ads} in the range of -0.6 to -0.8 eV (Yin *et al.*, 2016). The chemisorption is presented in both the adsorbed Li_2S_2 and Li_2S molecules with their adsorption energy of -1.33 and -1.48 eV, where such molecules favorably adopt the vertical adsorption facing Li atoms to the GDY plane. In addition, the equilibrium adsorption distance between the trapped molecules and the substrate reduces when Li/S ratio increases with 2.39, 2.25, 1.73, 1.72, and 1.59 Å for Li_2S_8 , Li_2S_6 , Li_2S_4 , Li_2S_2 , and Li_2S adsorption on pristine GDY. It manifests that the stronger the adsorption strength is the shorter the equilibrium distance. Overall, the trend of the amount of charge transfer from the LiPS molecules to the pristine GDY substrates is increased when the adsorption energies are stronger. The adsorbed S_8 obtains small additional electrons from the pristine GDY with at most 0.001 |e|, implying weak van der Waals interaction. The amount of electron migration is up when the GDY substrate adsorbed the LiPS molecules with Li/S decreased, where Δq are 0.076, 0.034, 0.154, 0.407, and 0.658 |e| for Li_2S_8 , Li_2S_6 , Li_2S_4 , Li_2S_2 , and Li_2S molecule, respectively. Such values are consistent with their adsorption strength. However, their adsorptions are still weak physisorption, leading to promote LiPS dissolution easily.

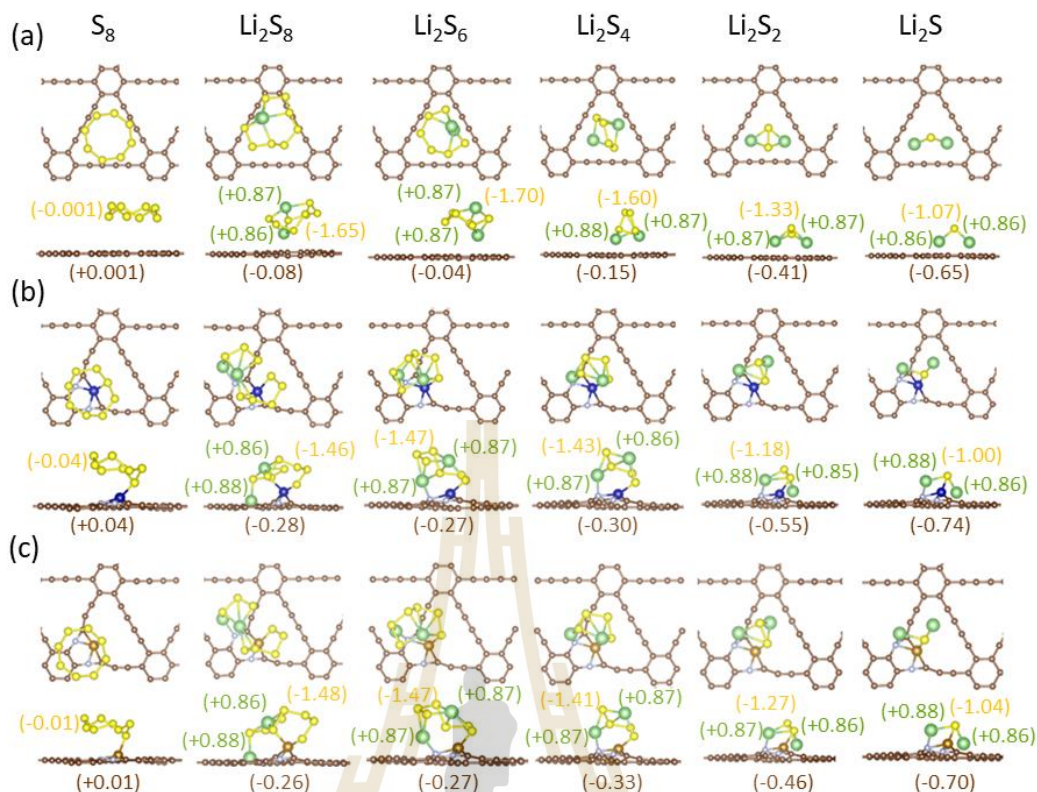


Figure 4.3 Top and side views of the most stable adsorption configurations of S_8 and LiPSs on (a) pristine GDY, (b) $CoN_2@GDY$, (c) $FeN_2@GDY$. Brown, C; light blue, N; yellow, S; green, Li; blue, Co; gold, Fe. Charges of each Li atom, all S atoms, and the substrate are labelled in green, yellow, and brown numbers, respectively.

Next, we examine the binding between S_8/Li_2S_x and the doped substrates. Various preferential adsorption sites were explored, and the most stable configurations of S_8/Li_2S_x adsorbed on the doped substrates are shown in Figure 4.3b,c. One of the S atoms in S_8 molecules could form the TM-S bond to the doped substrates with the bond distance of 2.11 Å and 2.16 Å for Co-S and Fe-S bond, respectively, which can be classified as covalent interaction. For LiPS adsorption, the adsorbed Li_2S_x even faces their S toward TM with the TM-S bond distance at most 2.20 Å, whereas their Li toward one of N atoms on the doped substrates with the Li-N bond distance at most 2.04 Å, for adsorption on both $CoN_2@GDY$ and $FeN_2@GDY$. Table 4.2 shows the change of atomistic bond distance of S_8/Li_2S_x upon adsorption on the doped substrates. the Li-S and S-S bonds are distorted owing to strongly chemical Li-N and TM-S bonds. The Li-S bond lengths are increased in all LiPS

molecules because of Li toward to react N at the substrate. Notably, the Li-S bond distance of Li_2S adsorbed the doped substrates is longest, leading to being strongest Li-N bond and adsorption which is a good agreement with the result in Figure 4.2. The bond distances of Li-S bonds are mostly increased by at least 0.12 Å, whereas those of S-S bonds in are decreased by at least 0.11 Å upon adsorption (see more details in Table 4.1 and 4.2). In particular, some S-S and Li-S bonds in the adsorbed Li_2S_8 on the doped GDY are broken with their breaking distance of 2.53 and 4.17 Å, respectively. This agrees with the experimental observation that, during the discharge process, Li_2S_8 readily accepts electrons and quickly transforms to other phases (Chen *et al.*, 2015).

Table 4.2 Geometric parameters of S_8 and LiPS after adsorption on $\text{MN}_2@\text{GDY}$.

LiPSs	$\text{CoN}_2@\text{GDY}$		$\text{FeN}_2@\text{GDY}$	
	S-S bond (Å)	Li-S bond (Å)	S-S bond (Å)	Li-S bond (Å)
S_8	2.05 - 2.15	-	2.02 - 2.13	-
Li_2S_8	2.02 - 2.08	2.38 - 2.66	1.99 - 2.09	2.57 - 3.01
Li_2S_6	2.05 - 2.06	2.39 - 2.40	2.32 - 2.43	2.37 - 2.40
Li_2S_4	2.04 - 2.08	2.37 - 2.54	2.02 - 2.03	2.43 - 2.49
Li_2S_2	2.08	2.88 - 2.34	2.1	2.32 - 2.36
Li_2S	-	2.34 - 2.35	-	2.37

As shown in Figure 4.2, the adsorption energies are substantially enhanced upon adsorption on the doped substrates. The adsorbed S_8 convinces the chemical interaction with E_{ads} of -1.60 and 1.47 eV on $\text{CoN}_2@\text{GDY}$ and $\text{FeN}_2@\text{GDY}$, respectively. For polysulfide adsorption, the calculated E_{ads} values on $\text{CoN}_2@\text{GDY}$ are -1.37 eV, -2.87 eV, -3.63 eV, -2.89 eV, and -3.45 eV, while those on $\text{FeN}_2@\text{GDY}$ are -1.42 eV, -2.87 eV, -2.17 eV, -3.15 eV, and -3.95 eV, for Li_2S_8 , Li_2S_6 , Li_2S_4 , Li_2S_2 , and Li_2S , respectively. Such interaction can be improved because of the presence of both TM and N dopants. The synergetic role of both dopants can be described by considering the Lewis acid-base theory, where TM behaves a Lewis acid as an electron acceptor while S acts as a Lewis base or electron donor. The TM atom receives the outer-

most valence electrons from the S atom where the interacted S is the most electron-rich site near Li atoms in LiPS molecules. Meanwhile, the N atom with high electronegativity (3.04) preferentially binds with the lower electronegative Li atom (0.98).

To get better understanding of adsorption strength, we further analyzed Bader charge analysis of the adsorption systems as shown in Figure 4.3 and APPENDIX A. They reveal that Li atoms on the adsorbed LiPS molecules show a positive charge of +0.9 |e|, whereas the net charge on S atom chains exhibit a negative charge in the range of -1.5 |e| to -1.0 |e|. The electrons on the adsorbed LiPS molecules transfer to the substrates. Notably, the net charge on S atoms tend to be decreased while the net charge on the doped substrates is prone to be increased with Li/S ratio increasing, suggesting that the adsorption strengths of short LiPS chains are stronger than those of long LiPS chains. In addition, the adsorptions of LiPS molecules on the FeN₂@GDY are slightly stronger than those on the CoN₂@GDY because the stronger Lewis acid of the doped Fe atom with higher number of unoccupied 3d states than those of the doped Co atom, leading to better interaction between the LiPS molecules and the doped substrates. This explanation is in good agreement with previous DFT-PBE calculations that the doped TM atom on the N-doped graphene with higher number of unoccupied 3d states strongly bind to the LiPS and S₈ molecules (L. Zhang *et al.*, 2018).

As a result, this is worth mentioning that CoN₂@GDY and FeN₂@GDY induce the chemical interaction with S₈ molecules, leading to good accommodation. In addition, the adsorptions of LiPS molecules are considerably increased because of the synergetic role of both TM-S and Li-N bonds. Such strong interaction may promote the prevention of LiPS dissolution and the suppression of shuttle. Compared to other cathode substrates for Li-S batteries, LiPS adsorbed on TM doped C₂N exhibits the same character where the doped TM binding with S and N binding with Li with the adsorption energies in the range of -2.5 to -5.0 eV (Lin *et al.*, 2019). It also suggests that Co@C₂N monolayer is the best host material. Likewise, a single-atom TM and N co-doped graphene enhance their adsorption energies toward LiPS molecules with E_{ads} in the range of -0.75 to -4.00 eV (L. Zhang *et al.*, 2018). Their

computations reveal that $\text{CrN}_4@$ graphene and $\text{FeN}_4@$ graphene show possible good performance for the Li-S batteries.

4.3 Electronic properties upon adsorption

To better understand the binding characters between LiPS molecules and the substrates, we further assessed their projected density of state (PDOS) and Bader charge distribution. As illustrated in Figure 4.4a, the band gap of GDY after and before S_8 adsorption is nearly identical, indicating weak interaction. Unlike this, the state of LiPS adsorption tends to shift to lower energy, increasing interaction strength. The overlapping of states at the same position occurs from S-C orbitals which are more dependent than Li-C orbitals. Thus, the hybridization between GDY carbon and LiPS sulfur is responsible for increasing adsorption energy. In addition, the mid-gap state of S orbital in Li_2S_4 , Li_2S_6 , and Li_2S_8 predominantly appears around the Fermi level. However, they occurred mid-gap is unreasonable for hybridization with C orbitals in GDY due to small perturbation in C orbitals, suggesting that GDY remains low conductivity to Li_2S_8 and Li_2S_6 . In contrast, Li_2S_4 adsorption promotes better electronic conductivity because of the appearing state in the GDY conduction band at the Fermi level. Li_2S_2 and Li_2S adsorption modify state at the Fermi level after their adsorption, which is beneficial to provide higher conductivity and easier eradicating Li_2S residue in the cathode during the charging process.

Figure 4.4b,c displays the DOS of S_8 and Li_2S_x adsorption on the doped systems. Apparently, the DOS of the doped systems upon adsorption still maintains good conductivity. This provides an advantage in accelerating the redox reaction for Li-S batteries. The electron state of the TM orbital can play a critical role in strongly hybridizing to S orbital at the same peak position, whereas Li-N overlapping is relatively low. This can manifest that the chemical interaction of the S-M and Li-N bonds is strong and weak, respectively. However, the peak of Li orbital in Li_2S_8 rises outstandingly to overlap N orbital in $\text{FeN}_2@$ GDY, which can answer why the adsorption energy of Li_2S_8 on $\text{FeN}_2@$ GDY is stronger than $\text{CoN}_2@$ GDY. This finding is essential to explain that transition metal atom possesses strong interaction with S in the adsorbates. The analysis is in good agreement with the PDOS of the adsorbed

systems that the overlap between Li and N states is negligible because of no covalent bond formed (see Figure 4.5) Therefore, only N doping in GDY still is not sufficient to improve the adsorption mechanism of this battery, which is constant with previous information. Their metallic properties of the substrates after Li_2S_2 and Li_2S adsorption effect to prolong more life cycle and increase Coulombic efficiency of Li-S battery.

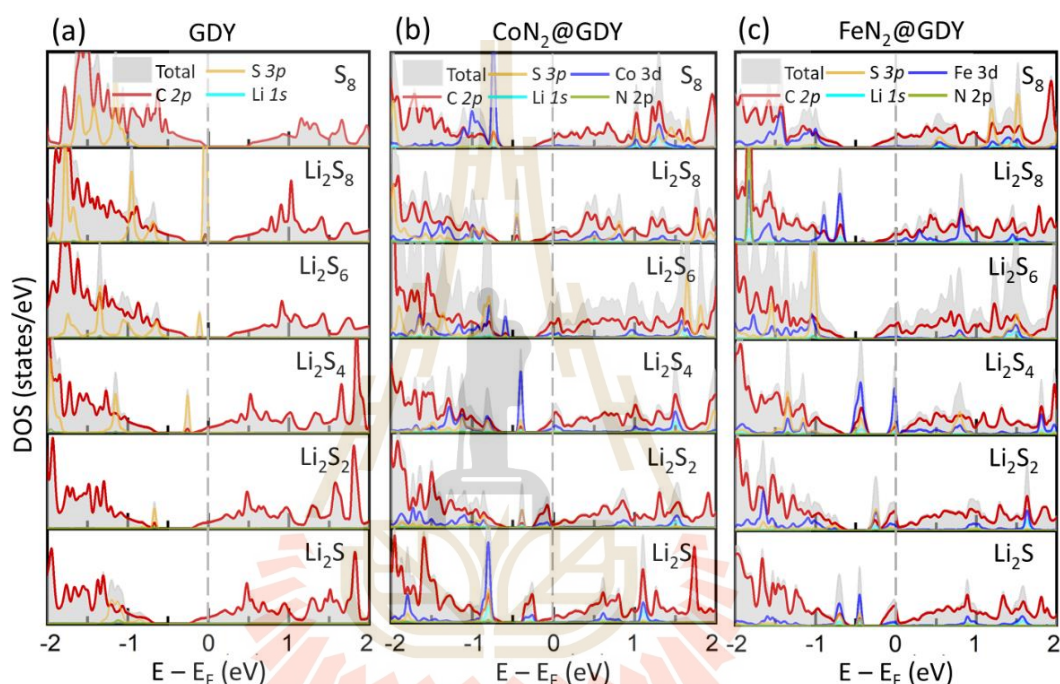


Figure 4.4 Projected density of state (PDOS) of S_8/LiPSs adsorption on (a) pristine GDY, (b) $\text{CoN}_2@\text{GDY}$, and (c) $\text{FeN}_2@\text{GDY}$. The Fermi level (E_F) is adjusted to 0 eV.

Overall, we analyzed the PDOS and charged transfer upon adsorption that the doped TM site behaves as the Lewis acid character binding with the Lewis base S atoms, while the doped high electronegative N site interacts with a Li atom through an electrostatic Coulombic force. The combination of TM and N active sites considerably improves the interaction of S_8 and LiPS molecules, leading to enhancing the battery performance of the cathode in Li-S batteries. Furthermore, such PDOS of the doped substrates with the molecule adsorption unravels the maintained metallic structures of the host cathode that promotes additional electron-rich facilitating

redox reaction activities during the charge and discharge process (Y. Wang *et al.*, 2019).

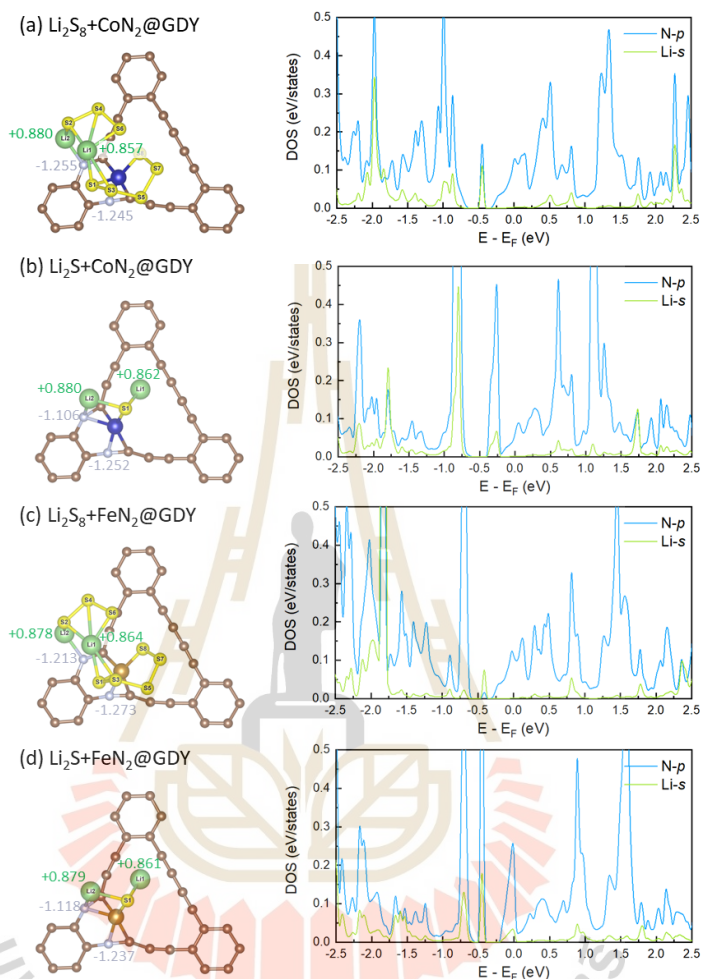


Figure 4.5 Bader charge distribution upon adsorption (left panel) and corresponding partial density of state (right panel) of Li and N for (a) Li_2S_8 and (b) Li_2S adsorbed $\text{CoN}_2@GDY$, and (c) Li_2S_8 and (d) Li_2S adsorbed $\text{FeN}_2@GDY$.

4.4 Suppression of shuttle effect

As we discussed in chapter I, the shuttle effect is a critical problem in fading the performance of Li-S batteries. Such a phenomenon stems from the dissolution of soluble LiPS molecules (i.e., Li_2S_8 , Li_2S_6 , and Li_2S_4) in the solvent. Both experimental and computational works suggest that the strong interaction between the electrolyte molecules and the LiPS molecules is the main cause leading to LiPS dissolution and shuttle effect (Hofmann *et al.*, 2014; M. Liu *et al.*, 2017; Xu *et al.*, 2017). To prevent

such processes, enhancing the adsorptivity on the electrode substrates is a promising way to restrict the motion of LiPS molecules (Q. Zhang *et al.*, 2015). In this section, we further explored the efficiency of the pristine and doped GDY systems to prevent polysulfide shuttling.

We initially discussed the common electrolyte used as a liquid solvent for Li-S cells. We chose 1,2-dimethoxyethane (DME) and 1,3-dioxolane (DOL) as ether-based electrolyte solvents in this work. DME is colorless and miscible with water, which is experimentally synthesized by the thermodynamic reaction between dimethyl ether and ethylene oxide (Claggett *et al.*, 1977). Meanwhile, DOL is a heterocyclic acetal containing the dioxolane ring prepared by the combination of aldehydes acetalization and ketones ketalization with ethylene glycol. Both electrolytes are commonly used as liquid electrolytes for Li-S batteries (Chang *et al.*, 2002). These electrolytes are compatible with the standard salt (LiTFSI) and exhibit poor solvation to LiPS as compared with the carbonate-based electrolytes (Choi *et al.*, 2008; Kim *et al.*, 2004; Scheers *et al.*, 2014)

We examined the adsorption of soluble LiPS molecules on the pristine and doped GDY substrates by introducing the explicit solvent molecules. Here, the Li_2S_6 was chosen as representative soluble LiPS molecule, that tends to dissolve owing to its weak adsorption strength as explained in section 4.2. Moreover, the experimental work reported that Li_2S_8 is immediately converted to smaller intermediate forms, while Li_2S_6 is more stable, and exists for a long time before further transformation during the charge and discharge cycles (Chen *et al.*, 2015). The optimized co-adsorbed systems include the adsorbed Li_2S_6 molecule on the substrates surrounded by added DME or DOL electrolytes from one up to four molecules, as shown in Figure 4.6. Both solvent molecules favorably bind with the adsorbed Li_2S_6 molecules, where the O atoms on the solvent molecules interact with the Li atoms on the Li_2S_6 toward the solvent media. One Li_2S_6 molecule adsorbed on the substrates can coordinate with 3 electrolyte molecules in the first solvation shell, where some Li atom is able to form Li-O bonds at most two bonds. The Li-O distances are in the range of 1.95 – 2.10 Å. The fourth electrolyte molecule stays at the outer solvation shell with a farther Li-O distance longer than 3.84 Å.

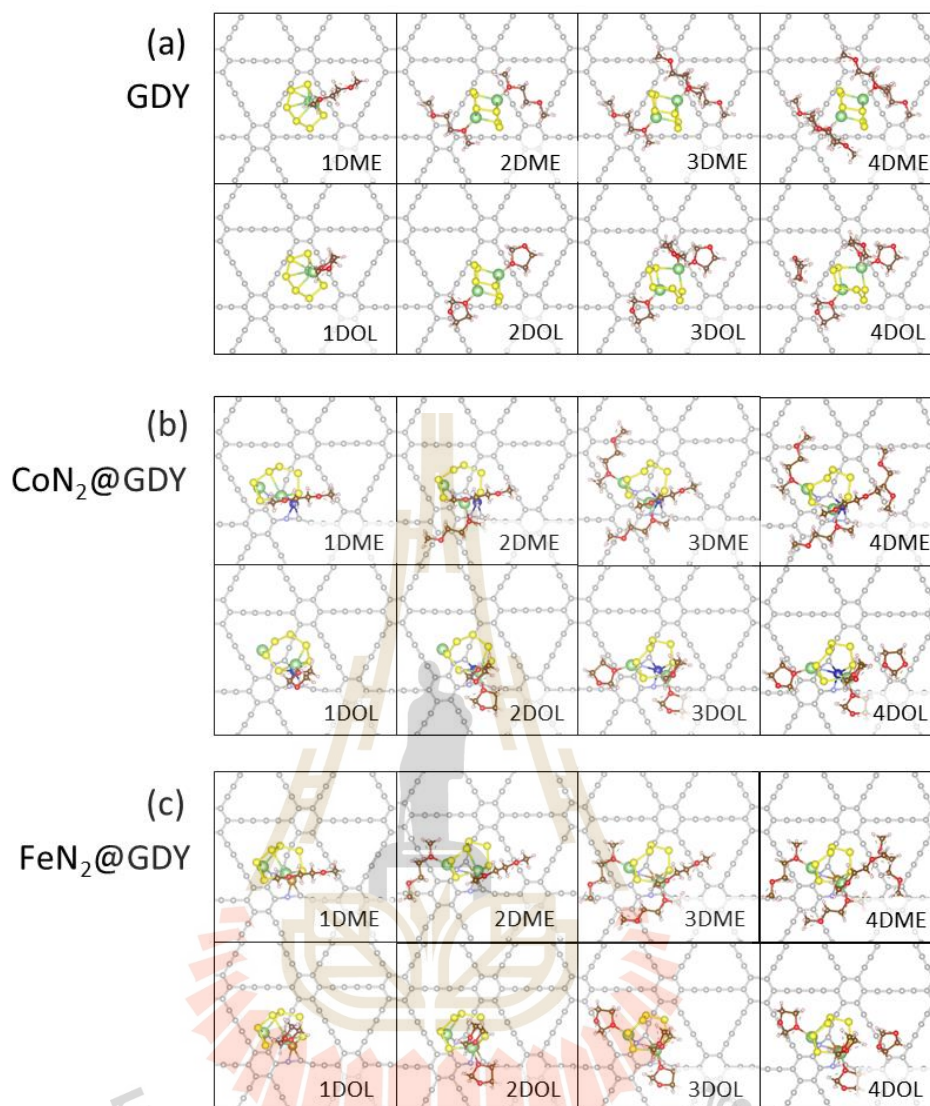


Figure 4.6 The co-adsorption configurations of 1 to 4 DME(s)/DOL(s) in the system of Li₂S₆ adsorbed on (a) GDY, (b) CoN₂@GDY, and (c) FeN₂@GDY. Color code: gray, GDY; brown, C; light blue, N; yellow, S; green, Li; white, H; blue, Co; gold, Fe; red, O.

To explore the prevention of polysulfide shuttling, we further calculated two involved energies in the co-adsorption systems: (i) the adsorption energies, $E_{ads, single}$, between the adsorbed Li₂S₆ molecule and the substrates, and (ii) the binding energies, $E_{b, single}$, between that Li₂S₆ molecule and the surrounding electrolyte molecules. Both energies were calculated in the same configuration corresponding to the co-adsorption systems shown in Figure 4.6. As schematically shown in Figure 4.7a, The corresponding $E_{ads, single}$ can be calculated as follow (Kamphaus *et al.*, 2016);

$$E_{ads, single} = E_{single}(Li_2S_6 + sub) - E_{single}(sub) - E_{single}(Li_2S_6) \quad (4.3)$$

where $E_{single}(Li_2S_6 + sub)$ is the calculated single-point energy of the adsorbed Li_2S_6 substrate obtained from the optimized solvated co-adsorbed configuration but removing the electrolyte molecules. $E_{single}(sub)$ and $E_{single}(Li_2S_6)$ are the calculated single-point energy of the substrate and an individual Li_2S_6 molecule, respectively. The binding interactions between the Li_2S_6 and the electrolyte molecules, $E_{b, single}$, are calculated using the following equation,

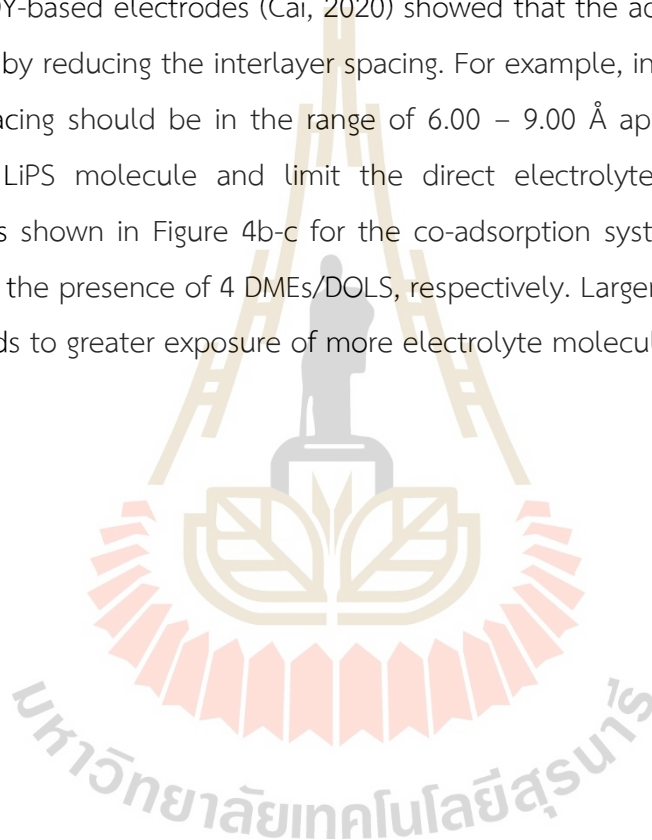
$$E_{b, single} = E_{single}(Li_2S_6 + elec) - E_{single}(elec) - E_{single}(Li_2S_6) \quad (4.4)$$

where $E_{single}(Li_2S_6 + elec)$ and $E_{single}(elec)$ are the calculated single-point energy of the optimized Li_2S_6 surrounded by electrolyte molecules but removing the substrate and the calculated single-point energy of electrolyte molecules, respectively. Then, the $E_{ads, single}$ and $E_{b, single}$ were compared to determine the dissolution of the Li_2S_6 molecule. If the $E_{ads, single}$ is more substantial (more negative) than the $E_{b, single}$, the adsorption prevails where the shuttle effect is suppressed, otherwise the dissolution is predicted. It should be noted that the additional electrolyte molecules do not directly interact with the adsorbed Li_2S_6 molecule (see Figure 4.8).

In both DME and DOL, the pristine GDY is ineffective electrode material to suppress the polysulfide shuttling because the interaction between the adsorbed Li_2S_6 molecule and the solvent is stronger than the adsorption of such Li_2S_6 on the GDY substrate, as shown in Figure 4.7b. The interaction energies tend to increase negatively with the increase of solvent molecules in the systems. The bind energies range from -0.85 to -2.74 eV, whereas the adsorption energies are relatively constant at around -0.5 eV. The dissolution of Li_2S_6 is expected even at low contact with one surrounding electrolyte molecule. The stronger interaction toward the liquid solvent induces the dissolution of the soluble LiPS, resulting in the shuttle effect.

The LiPS dissolution can be effectively prevented by introducing TM and N dopants on the GDY substrate. As shown in Figure 4.7b, the adsorption strength between Li_2S_6 and the doped substrates is improved up to -3.35 eV, where it was adsorbed on the TM-N center on the GDY substrate, suggesting that the combination between TM-S and Li-N bonds is significantly stronger than the Li-O bonds. Therefore, the enhanced adsorptivity significantly reduces the shuttling of the LiPS molecules.

In addition, our computation suggests that the candidate host cathode material for Li-S batteries should have the adsorption energy between the LiPS and the substrate of at least -3.0 eV to dramatically suppress the dissolution of LiPS molecules. It should be noted that we studied only the adsorption on the GDY monolayer system to explore the suppression. The required adsorption strength to suppress the dissolution may vary if we consider the LiPS adsorption in other systems such as multilayer systems. Previous computational studies of graphene- (Kamphaus *et al.*, 2016) and GDY-based electrodes (Cai, 2020) showed that the adsorption strength can be improved by reducing the interlayer spacing. For example, in the case of Li_2S_6 , the interlayer spacing should be in the range of 6.00 – 9.00 Å approximately to better confine the LiPS molecule and limit the direct electrolyte contact within two molecules, as shown in Figure 4b-c for the co-adsorption system of Li_2S_6 adsorbed CoN_2 @GDY in the presence of 4 DMEs/DOLS, respectively. Larger interlayer spacing up to 9.00 Å leads to greater exposure of more electrolyte molecules.



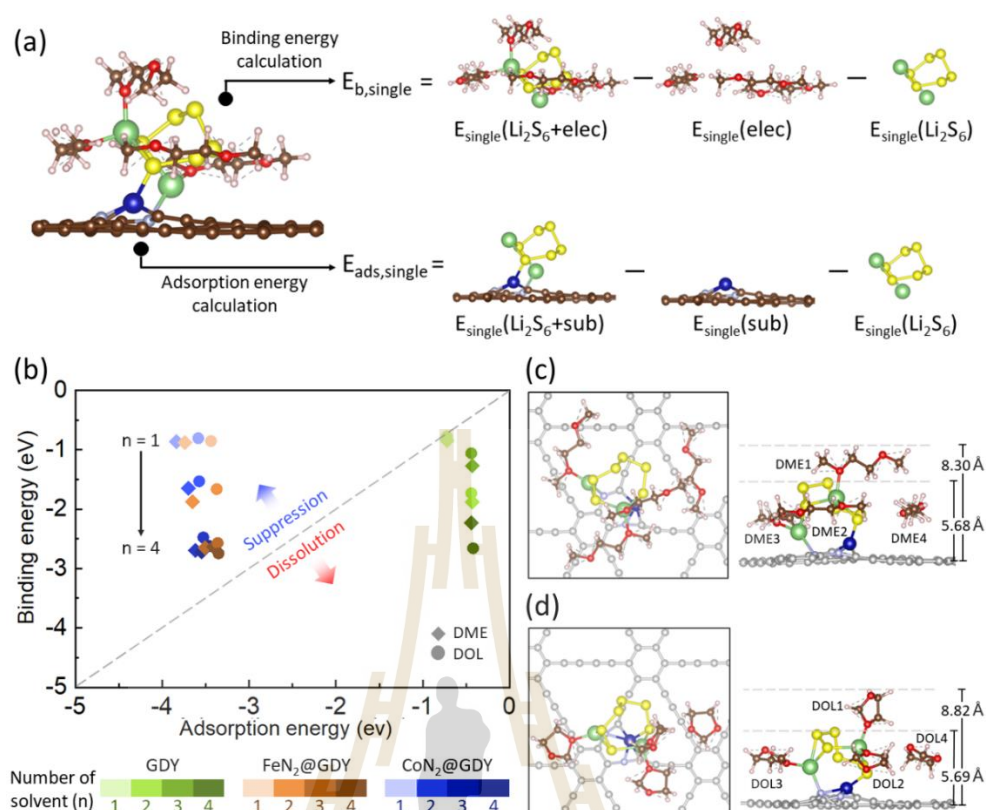


Figure 4.7 Schematic illustration of a) the computations of adsorption energy ($E_{ads,single}$) and binding energy ($E_{b,single}$), b) the comparison between $E_{ads,single}$ and $E_{b,single}$ to predict the suppression of shuttle effect and dissolution of LiPS. Co-adsorbed configuration of Li₂S₆ on CoN₂@GDY in the presence of (c) DME or (d) DOL molecules. The labeled distances identify the vertical distance from the substrate to the topmost of the electrolyte molecules. Gray, GDY; brown, C; light blue, N; yellow, S; green, Li; white, H; blue, Co; gold, Fe; red, O.

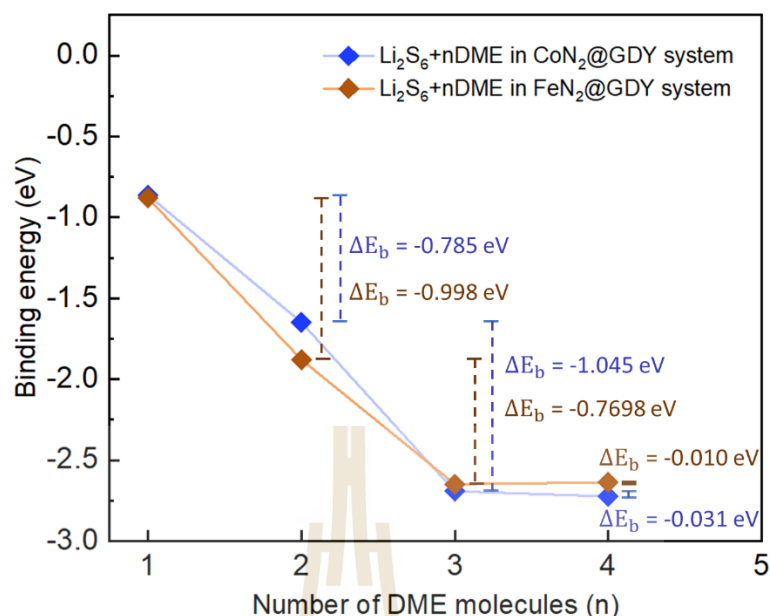


Figure 4.8 The difference of binding energies between Li₂S₆ and DME molecule(s) in the co-adsorption systems of CoN₂@GDY (blue line) and FeN₂@GDY (brown line).

4.5 References

- Arneson, C., Wawrzyniakowski, Z. D., Postlewaite, J. T., and Ma, Y. (2018). Lithiation and Delithiation Processes in Lithium–Sulfur Batteries from Ab Initio Molecular Dynamics Simulations. *The Journal of Physical Chemistry C*. 122: 8769.
- Cai, Y. (2020). The Anchoring Effect of 2D Graphdiyne Materials for Lithium–Sulfur Batteries. *ACS Omega*. 5: 13424.
- Chang, D.-R., Lee, S.-H., Kim, S.-W., and Kim, H.-T. (2002). Binary electrolyte based on tetra (ethylene glycol) dimethyl ether and 1, 3-dioxolane for lithium–sulfur battery. *Journal of Power Sources*. 112: 452.
- Chen, J.-J., Yuan, R.-M., Feng, J.-M., Zhang, Q., Huang, J.-X., Fu, G., Zheng, M.-S., Ren, B., and Dong, Q.-F. (2015). Conductive Lewis Base Matrix to Recover the Missing Link of Li₂S₈ during the Sulfur Redox Cycle in Li–S Battery. *Chemistry of Materials*. 27: 2048.
- Choi, J.-W., Cheruvally, G., Kim, D.-S., Ahn, J.-H., Kim, K.-W., and Ahn, H.-J. (2008). Rechargeable lithium/sulfur battery with liquid electrolytes containing toluene as additive. *Journal of Power Sources*. 183: 441.

- Claggett, A. R., Ilsley, W. H., Anderson, T. J., Glick, M. D., and Oliver, J. P. (1977). Metal-silicon bonded compounds. 9. The synthesis and structure of bis(trimethylsilyl)magnesium 1,2-dimethoxyethane adduct. *Journal of the American Chemical Society*. 99: 1797.
- Hofmann, A. F., Fronczek, D. N., and Bessler, W. G. (2014). Mechanistic modeling of polysulfide shuttle and capacity loss in lithium-sulfur batteries. *Journal of Power Sources*. 259: 300.
- Kamphaus, E. P., and Balbuena, P. B. (2016). Long-Chain Polysulfide Retention at the Cathode of Li-S Batteries. *The Journal of Physical Chemistry C*. 120: 4296.
- Kim, S., Jung, Y., and Lim, H. S. (2004). The effect of solvent component on the discharge performance of Lithium-sulfur cell containing various organic electrolytes. *Electrochimica Acta*. 50: 889.
- Lin, H., Jin, R., Wang, A., Zhu, S., and Li, H. (2019). Transition metal embedded C2N with efficient polysulfide immobilization and catalytic oxidation for advanced lithium-sulfur batteries: A first principles study. *Ceramics International*. 45: 17996.
- Liu, M., Li, Q., Qin, X., Liang, G., Han, W., Zhou, D., He, Y.-B., Li, B., and Kang, F. (2017). Suppressing Self-Discharge and Shuttle Effect of Lithium-Sulfur Batteries with V2O5-Decorated Carbon Nanofiber Interlayer. *Small*. 13: 1602539.
- Liu, X., Shao, X., Li, F., and Zhao, M. (2018). Anchoring effects of S-terminated Ti2C MXene for lithium-sulfur batteries: A first-principles study. *Applied Surface Science*. 455: 522.
- Meyer, B. (1976). Elemental sulfur. *Chemical Reviews*. 76: 367.
- Scheers, J., Fantini, S., and Johansson, P. (2014). A review of electrolytes for lithium-sulphur batteries. *Journal of Power Sources*. 255: 204.
- Studel, R. (1996). Das gelbe Element und seine erstaunliche Vielseitigkeit. *Chemie in unserer Zeit*. 30: 226.
- Wang, D., Li, F., Lian, R., Xu, J., Kan, D., Liu, Y., Chen, G., Gogotsi, Y., and Wei, Y. (2019). A General Atomic Surface Modification Strategy for Improving Anchoring and Electrocatalysis Behavior of Ti3C2T2 MXene in Lithium-Sulfur Batteries. *ACS Nano*. 13: 11078.

- Wang, L., Zhang, T., Yang, S., Cheng, F., Liang, J., and Chen, J. (2013). A quantum-chemical study on the discharge reaction mechanism of lithium-sulfur batteries. *Journal of Energy Chemistry*. 22: 72.
- Wang, Y., Shen, J., Xu, L.-C., Yang, Z., Li, R., Liu, R., and Li, X. (2019). Sulfur-functionalized vanadium carbide MXene (V₂CS₂) as a promising anchoring material for lithium-sulfur batteries. *Physical Chemistry Chemical Physics*. 21: 18559.
- Wasalathilake, K. C., Roknuzzaman, M., Ostrikov, K., Ayoko, G. A., and Yan, C. (2018). Interaction between functionalized graphene and sulfur compounds in a lithium-sulfur battery – a density functional theory investigation. *RSC Advances*. 8: 2271.
- Xu, N., Qian, T., Liu, X., Liu, J., Chen, Y., and Yan, C. (2017). Greatly Suppressed Shuttle Effect for Improved Lithium Sulfur Battery Performance through Short Chain Intermediates. *Nano Letters*. 17: 538.
- Yin, L.-C., Liang, J., Zhou, G.-M., Li, F., Saito, R., and Cheng, H.-M. (2016). Understanding the interactions between lithium polysulfides and N-doped graphene using density functional theory calculations. *Nano Energy*. 25: 203.
- Zhang, L., Liang, P., Shu, H. B., Man, X. L., Du, X. Q., Chao, D. L., Liu, Z. G., Sun, Y. P., Wan, H. Z., and Wang, H. (2018). Design rules of heteroatom-doped graphene to achieve high performance lithium-sulfur batteries: Both strong anchoring and catalysing based on first principles calculation. *Journal of Colloid and Interface Science*. 529: 426.
- Zhang, Q., Wang, Y., Seh, Z. W., Fu, Z., Zhang, R., and Cui, Y. (2015). Understanding the Anchoring Effect of Two-Dimensional Layered Materials for Lithium-Sulfur Batteries. *Nano Letters*. 15: 3780.

CHAPTER V

SOLUBILITY AND DISSOCIATION OF POLYSULFIDES

In the previous section, we assessed the ability to suppress of anchoring effect of TM and N doping. Our computations reveal that both $\text{CoN}_2@\text{GDY}$ and $\text{FeN}_2@\text{GDY}$ can effectively prevent the dissolution of soluble polysulfide molecules. In this chapter, using ab initio molecular dynamic (AIMD) simulation, we further considered the solubility of soluble LiPS molecules in the liquid electrolyte solvent to study their behaviors in non-effective suppression, as discussed in section 5.1. Moreover, the reduction products at the final discharge process, namely Li_2S_2 and Li_2S , are the insulative solid phase with low electronic conductivity. Their dissociation during charging is difficult due to the high activation energy for the phase conversion changing from LiPS to S_8 . Here, we also studied the effect of TM-N doping as a catalyst center to promote the phase transformation of Li_2S_2 and Li_2S , as discussed in section 5.2.

5.1 Solubility of the soluble LiPS in an electrolyte solution

The intermediate reduction products, especially long-chain LiPS molecules (Li_2S_8 , Li_2S_6 , and Li_2S_4), possess high solubility in electrolyte solvents. Here, we investigated the behavior of soluble LiPS species in ether-based electrolyte solvents, including DME and DOL, to study the solubility using AIMD simulation. The simulations were carried out with the NVT ensemble of the Nose-Hoover thermostat with a time step of 5 fs for five ps at 300 K. To lower the expense of the calculations, we used Gamma-point only for k-point sampling with an energy cutoff of 450 eV. In our models, one Li_2S_x molecule ($x = 4, 6, \text{ or } 8$) was added at the center of the cubic box with a size of $15 \times 15 \times 15 \text{ \AA}^3$. Afterward, electrolyte molecules were randomly packed into the box, where they were located surrounding the added LiPS molecule. The number of the added electrolytes was calculated regarding the liquid density of DME (0.87 g cm^{-3}) and DOL (1.06 g cm^{-3}) at room temperature. It should be noted

that both electrolytes were optimized using DFT calculation before packing, and their geometric structure and bond distances between atoms are consistent with previous DFT-PBE calculations.

After the simulation finished, the dynamically lowest energy configurations from the AIMD simulation were chosen to relax using the DFT method in order to get the ground-state energies and the optimized structures. We calculated the solvation energies, E_{sol} , of the soluble LiPS molecule in the DME and DOL solvent to examine the efficiency of dissolution of the LiPS molecule, which was calculated by using the following equation,

$$E_{sol} = E_{LiPS+solv} - E_{LiPS} - E_{solv} \quad (5.1)$$

where $E_{LiPS+solv}$ is the total energy of the optimized system of the LiPS molecule surrounded by solvent molecules, E_{LiPS} is the total energy of an isolated LiPS (Li_2S_8 , Li_2S_6 , or Li_2S_4) molecule, and is the total energy of the optimized solvent molecules (DME or DOL) in the system.

The optimized geometric dissolution configurations are shown in Figure 5.1a-f. Our computations reveal that there is no decomposition of the dissolved LiPS molecules because they still maintain their molecular structures throughout the AIMD simulation for 5 ps, indicating good thermodynamical stability in the electrolyte solutions. However, some bond distances between Li and S atoms on the LiPS molecules are elongated in the range of 2.27 – 2.65 Å because of the interaction between the Li atoms on LiPS and O atoms on the nearest electrolyte molecule. We also observed that one LiPS molecule (Li_2S_8 , Li_2S_6 , or Li_2S_4) can directly interact with at most 3 DME or 5 DOL molecules in the first solvation shell, whereas the others are in the outer solvation shell with a far distance of more than 5 Å.

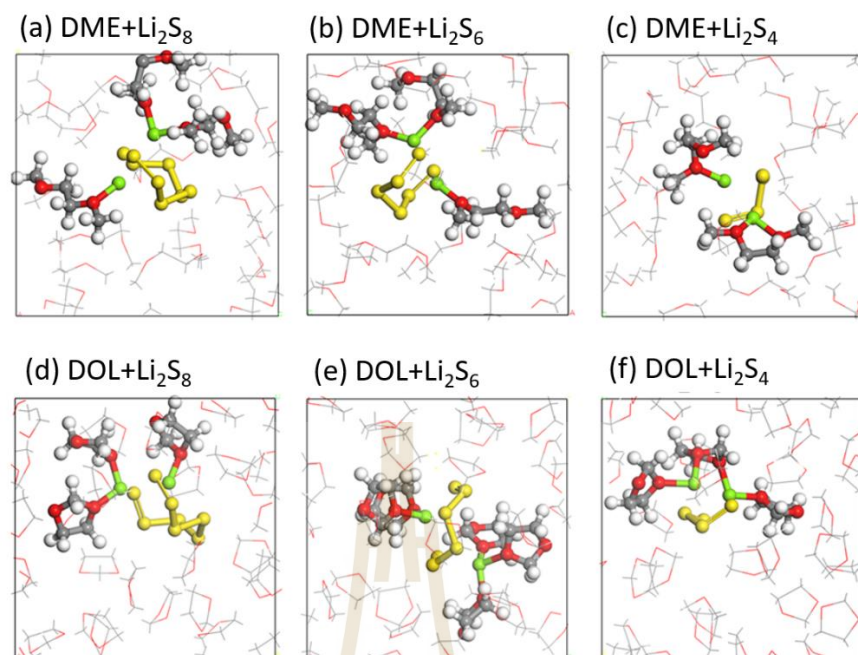


Figure 5.1 Low-energy configurations of a-c) DME- and d-f) DOL-solvated LiPSs as obtained from AIMD simulations. Illustrations in the ball-and-stick model represent electrolyte molecules in the first solvation shell, whereas the wireframe models are the outer solvation shell.

To identify the intermolecular structure, we further calculated the radial distribution function (RDF) for the DME and DOL solvent systems. The RDF calculation of Li_2S_8 in DME and DOL solvent was analyzed as the example case, as shown in Figures 5.2a and 5.2b, respectively. The peaks of Li-S RDFs in both solvent systems are quite different due to the molecular geometry during simulation. Such two outstanding peaks of Li-S RDFs exhibit the interaction between Li and S atoms at 2.47 and 3.50 Å, suggesting their close interaction along the simulation time. No decomposition of LiPS molecules may stem from the strong bonding of electron-rich atoms at the edge of the polysulfide chain interacting with positive charge Li atoms. For the Li-O RDFs, the Li ions closely interact with O atoms on the DME/DOL molecules at around 1.9 Å. The other RDFs of Li-C/H and S-C/H/O do not show any significant interaction, which is in good agreement with the previous computation (Kamphaus *et al.*, 2017).

As shown in Figure 5.2c, the analysis of the solubility of soluble LiPS molecules exhibits that the solvation energies are more negatively increased when the size of LiPS molecules increases, suggesting significantly vital interactions in the electrolyte media. In particular, the large LiPS molecule, Li_2S_8 , is able to easily dissolve in the electrolyte with the solvation energies of -3.75 eV and -3.04 eV in DME and DOL solvents, respectively. This explanation is in good agreement with the experimental investigations that the solubility depends on the molecular size of LiPS molecules (Mikhaylik *et al.*, 2004). Furthermore, the solvation energy in the DME solution is basically more negative than those in the DOL solution, indicating that soluble LiPS better dissolve in the DME solution, leading to the undesired shuttle effect.

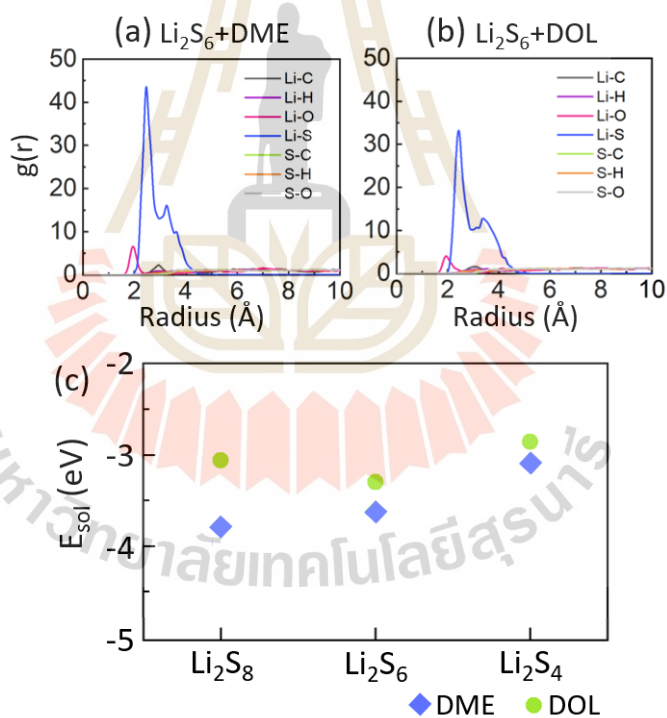


Figure 5.2 The corresponding radial distribution functions (RDFs) of Li and S bonding to elements on electrolyte molecules in (c) DME and (d) DOL systems. (g) their corresponding solvation energies.

5.2 Dissociation and diffusion of Li ions on LiPS

In chapter 4, we exhibited that the TM and N doping on GDY substantially enhances the adsorption strength toward LiPS molecules, which can inhibit the dissolution of long-chain LiPS molecules, leading to suppression of the shuttle effect. Here, we further examined the impact of TM-N doping on GDY substrate to improve the catalytic performance to enhance the sulfur utilization by investigating the decomposition of short-chain LiPS molecules, including Li_2S_2 and Li_2S . The slow phase transformation of the short-chain LiPS molecules is the main reason for rapid capacity decay, poor sulfur usage, and low-term cycle of Li-S batteries (Assary *et al.*, 2014). This difficult transformation is attributed to the high decomposition energy barrier of the LiPS dissociation mechanism leading to a kinetically sluggish oxidation reaction during charging. For this reason, reducing the activation energy with the help of a good catalysis material is an excellent way to facilitate the phase conversion process and contribute to the kinetic oxidation reaction. Herein, we investigated the decomposition mechanisms of short-chain LiPS molecules on the pristine and doped GDY substrates using CI-NEB calculation in VASP code. Furthermore, we also study the diffusion of the extracted Li-ion from the small LiPS molecules traveling on the substrate to assess ion mobility.

The energy profiles and corresponding reaction coordinates of the decomposition of Li_2S_2 and Li_2S are shown in Figure 5.3. There is a 2-reaction step, including (i) the delithiation of Li on LiPS molecules ($\text{A} \rightarrow \text{B}$), and (ii) the diffusion of the extract Li ion to the favorable adsorption site ($\text{B} \rightarrow \text{C}$). As shown in Figure 5.3a, the Li-S bond breaking of Li_2S_2 into LiS_2 and Li is difficult on the pristine GDY with the high decomposition energy barrier (E_a) of 0.86 eV. The decomposition products are unstable because the relative energy state of the products is higher than that of the precursor with endothermic reaction energy (E_r) of 0.73 eV. This difficult decomposition may stem from two bond breaking of Li-S bonds on the Li_2S_2 molecule (see Figure 5.3c). For the following step, the Li diffusion requires a small energy barrier of 0.11 eV with nearly thermoneutral reaction energy. It suggests that the delithiation process is the rate-determining step for the phase transformation on the pristine GDY with the effective barrier of 0.86 eV.

The difficult delithiation process of Li_2S_2 is dramatically improved with the presence of a doped TM-N center on GDY. This is because the weakened Li-S interaction on the molecules easily induces Li-S bond cleavage. Overall, the decomposition energy barrier is decreased on the doped GDY compared to that on the pristine one. As shown in Figure 5.3c, the Li_2S_2 on the doped GDY undergoes the decomposition reaction, yielding LiN and $\text{LiS}_2\text{-TM}$ intermediates, where the extracted Li moves down in the favorable site at the triangle GDY pore. Notably, the energy profiles for $\text{CoN}_2\text{@GDY}$ and $\text{FeN}_2\text{@GDY}$ are quite different, where the delithiation on the FeN_2 center shows endothermically up-hill for its delithiation process ($E_r = 0.29$ eV, $E_a = 0.41$ eV) and the diffusion process ($E_r = 0.20$ eV, $E_a = 0.40$ eV), where the overall reaction energy is 0.49 eV with the effective barrier of 0.69 eV (0.29 + 0.40).

For the Li_2S_2 decomposition on the $\text{CoN}_2\text{@GDY}$, the delithiation of the Li-S bond exhibits a small barrier of 0.13 eV with the exothermic reaction energy of -0.86 eV owing to the formation of stable products. The delithiation of the Li-S bond in the CoN_2 system is more thermodynamically durable than that in the FeN_2 system because the delithiation products move to the most favorable adsorption site into the triangle pore of $\text{CoN}_2\text{@GDY}$. In contrast, the position of the extract Li-ion in the FeN_2 system locates at 0.96 Å above the GDY plate, as shown in Figure 5.4. The following diffusion of Li-ion is an up-hill process with the diffusion barrier of 0.50 eV, which equals the reaction energy of diffusion. The overall effective barrier is the Li-N bond breaking of 0.51 eV with the overall exothermic reaction energy of -0.36 eV. To sum up, the role of TM-N doping decreases the decomposition energy barrier from 0.86 eV for the pristine GDY to 0.69 eV and 0.50 eV for $\text{FeN}_2\text{@GDY}$ and $\text{CoN}_2\text{@GDY}$, respectively.

For the decomposition of Li_2S , the energy profiles and corresponding reaction coordinates are shown in Figure 5.3b,d, respectively. Overall, the decomposition of Li_2S is thermodynamically and kinetically more favorable than Li_2S_2 . The delithiation of Li-S bond breaking on the pristine GDY provides the small decomposition energy barrier of 0.42 eV with the exothermic reaction energy of -0.34 eV. The stable decomposition products stem from the formation of chemical S-C interaction on the GDY linkage, where the S-C bond distance is 1.75 Å. The computation through the

Bader charge analysis suggests the electron migration with 1.3 e from the S atoms to the GDY substrate, which is higher than the charge transfer for Li₂S adsorption on the GDY (0.7 e). For the Li-ion diffusion step, Li moves to the next preferential site with the barrier of 0.54 eV by the reaction energy of 0.49 eV. The overall reaction energy is quite endothermic by 0.15 eV with an effective barrier of 0.54 eV for the Li-S bond breaking. Here, the rate-determining step is the Li diffusion instead of the delithiation, which is different from the previous reports that the decomposition of Li-S bond breaking is kinetically difficult (Y. Wang *et al.*, 2019; Zhou *et al.*, 2020). In addition, the stable formation of the Li-C bond may be the main contribution to improving the kinetics. The sp³ C atoms on the acetylenic linkage of pristine GDY could be the origin of the facile decomposition of the short-chain LiPS molecules. Compared to the other host cathode materials, our result suggests that the effective barrier of Li₂S decomposition on GDY (0.54 eV) is lower than that on the graphene (1.81 eV), which is consistent with the experimental investigation that GDY cathode shows a higher capacity, 713.7 mA h g⁻¹ at 100 cycles (Du *et al.*, 2017), than that of graphene cathodes, 662 mA h g⁻¹ at 100 cycles (B. Wang *et al.*, 2012), for the Li-S batteries.

With the introduction of the doped TM-N center, the decomposition reaction of Li₂S is thermodynamically and kinetically more favorable. As illustrated in Figures 5.3b and 5.3d, the delithiation process comprises two-reaction steps where the Li-S bond is elongated and reorganized on the Li₂S molecule, taking place before the cleavage of the Li-S bond. These steps are dramatically exothermic with small decomposition barrier for both FeN₂ ($E_r = -0.65$ eV, $E_a = 0.13$ eV) and CoN₂ ($E_r = -0.94$ eV, $E_a = 0.16$ eV) systems, followed by the endothermic reaction of the Li-N bond breaking with higher barrier for FeN₂ ($E_r = 0.52$ eV, $E_a = 0.53$ eV) and CoN₂ ($E_r = 0.50$ eV, $E_a = 0.52$ eV) systems. Both systems provide stable products than the precursor, where the exothermically effective reaction energies are 0.13 and 0.44 eV for FeN₂ and CoN₂ systems, respectively, which are more favorable than the endothermic reaction energy for the pristine GDY (0.15 eV). Compared to the effective reaction barrier for the pristine GDY (0.54 eV), the doped substrates provide the unchanged effective barrier of the FeN₂ (0.53 eV) and CoN₂ (0.52 eV) systems. We also compare the effective barriers with that decomposition for Li₂S molecules on the other

cathode materials such as V_2CO_2 with 0.43 eV (Y. Wang *et al.*, 2019), SnS_2 with 0.50 eV (Zhou *et al.*, 2017), and Ti_2CS_2 with 1.51 eV (B. Wang *et al.*, 2012). Furthermore, the Li_2S_2 and Li_2S decomposition on the doped GDY is energetically more favorable than those on the Co- and Fe-N4@graphene, where the total reaction energies of the doped GDY are at least 1.03 eV (Zeng *et al.*, 2019; L. Zhang *et al.*, 2018). Here, our computations reveal that the $CoN_2@GDY$ and $FeN_2@GDY$ promote the phase transformation and contribute to the decomposition, leading to more S utilization and long-term cycling for the cathode in Li-S batteries.

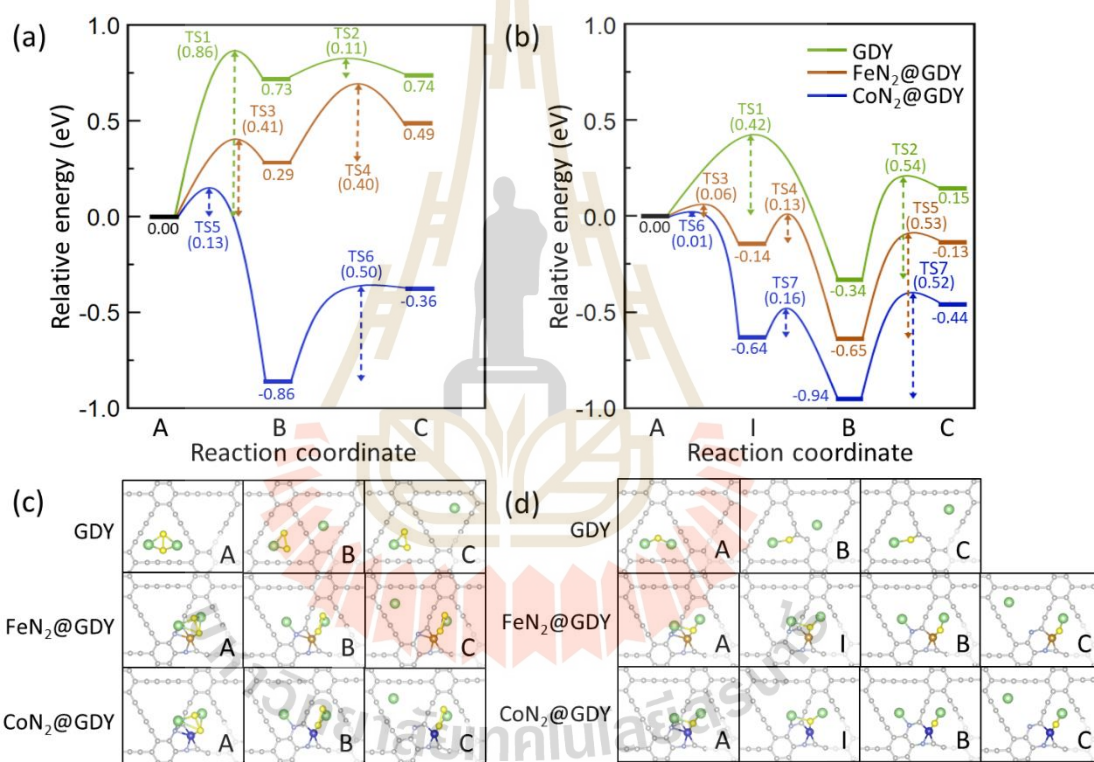


Figure 5.3 Potential energy profiles of (a) Li_2S_2 and (b) Li_2S decompositions on GDY (green line), $CoN_2@GDY$ (blue line), and $FeN_2@GDY$ (yellow line), and their corresponding intermediates for (c) Li_2S_2 and (d) Li_2S decompositions. The labeled numbers at the intermediate states indicate their relative energies, whereas the numbers in parentheses denote the energy barriers.

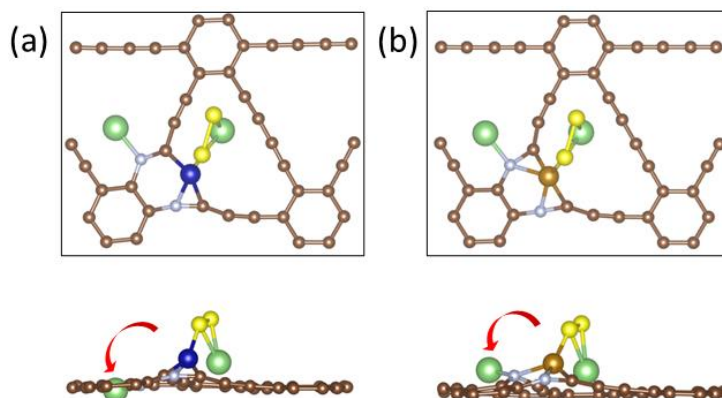


Figure 5.4 Top and side views for dissociation of Li-S bond of Li_2S_2 on (a) $\text{CoN}_2@\text{GDY}$ and (b) $\text{FeN}_2@\text{GDY}$. These configurations are the same as site B in Figure 5.3c. Brown, C; light blue, N; yellow, S; green, Li; blue, Co; gold, Fe.

We also investigated other decomposition pathways of Li_2S_2 and Li_2S on the doped systems, as shown in Figure 5.5. It should be noted that these different paths are energetically less favorable than the presented decomposition reaction, as shown in Figure 5.3. For the other high-energy paths, the delithiation process of Li-S bond breaking is an endothermic reaction by the decomposition energy barrier of more than 1 eV, where the reaction energies of both Li_2S_2 and Li_2S are in the range of 0.89 – 0.91 eV, suggesting that the reduction products are unstable than their precursors. The extracted Li ion travels across the acetylenic linkage, adsorbing on the favorable sites on the neighboring triangle GDY pore. The computation shows that the delithiation process of Li_2S on both doped systems is nearly identical and has a decomposition barrier of around 1.27 eV. At the same time, those of Li_2S_2 are slightly different, where $\text{CoN}_2@\text{GDY}$ provides the reaction energy (0.88 eV) and corresponding barrier (1.15 eV) smaller than $\text{FeN}_2@\text{GDY}$.

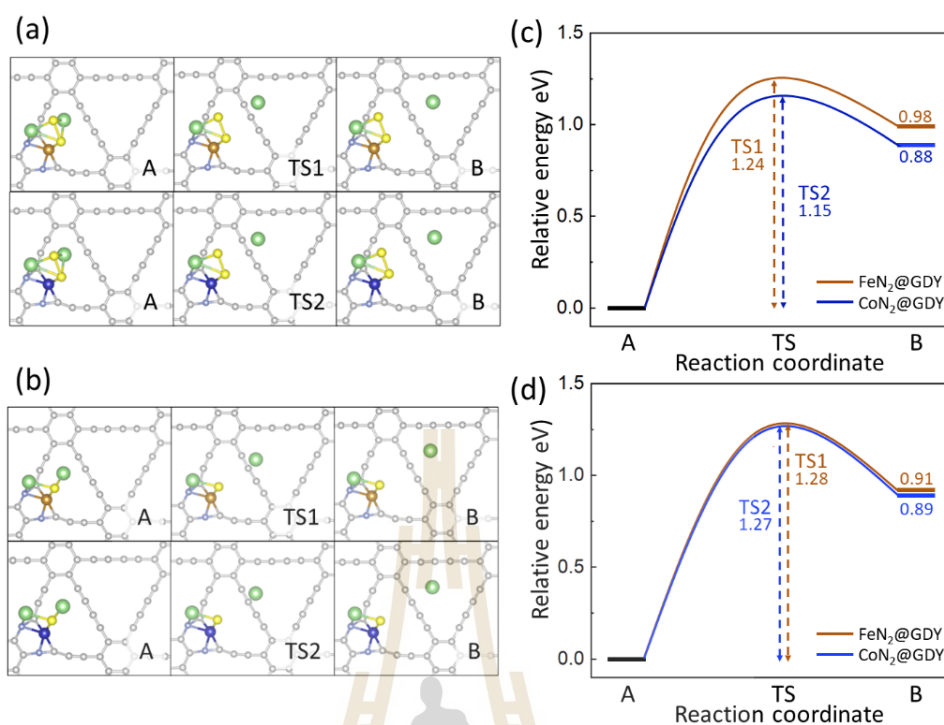


Figure 5.5 Another reaction path of catalytic decomposition of (a) Li_2S_2 and (b) Li_2S , and corresponding energy profile of (c) Li_2S_2 and (d) Li_2S , respectively, on $\text{CoN}_2@GDY$ (blue line) and $\text{FeN}_2@GDY$ (yellow line). Color code: gray, C; light blue, N; yellow, S; green, Li; blue, Co; gold, Fe.

Moreover, we also explored the Li diffusion on the pristine GDY, as shown in Figure 5.6. In this case, we can assume that this diffusion happens far from the TM-N doped center in the doped systems. Our computation reveals that the Li-ion migrates to the next favorable adsorption site in the same triangle pore with a small diffusion barrier of 0.10 eV. Meanwhile, the diffusion barrier is increased up to 0.61 eV when the Li-ion diffuses jumping across an acetylenic linkage to the neighboring pore. Such calculated diffusion barriers are slightly similar to those for other 2D-carbon cathode, such as graphene with 0.48 eV (H. Zhang *et al.*, 2013) and graphyne with 0.72 eV (Sun *et al.*, 2012), using DFT-PBE calculation. However, these moderate barriers are still lower than the initial operating potential of 3.45 volts for the charging process (Yang *et al.*, 2012).

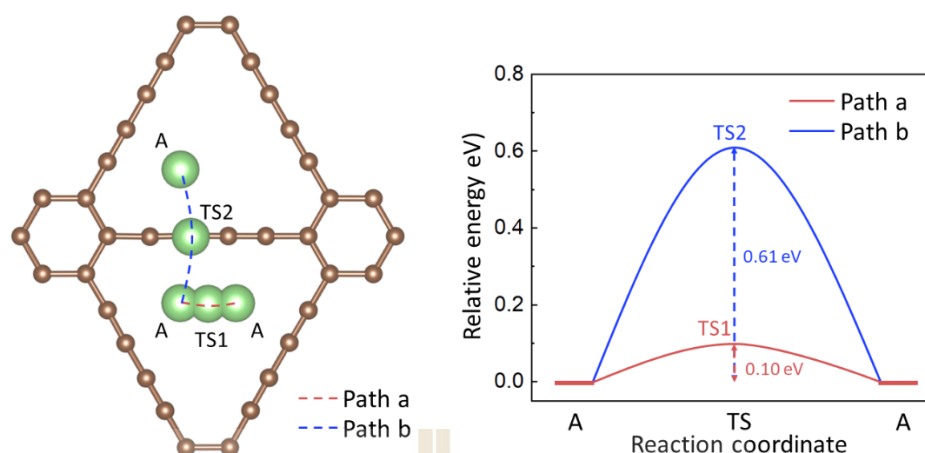


Figure 5.6 Diffusion of Li-ion along path a (red dash line) and path b (blue dash line), left panel. The corresponding energy profile along the path a (red solid line) and path b (blue solid line), right panel. Color code: brown, C; green, Li.

5.3 Reference

- Assary, R. S., Curtiss, L. A., and Moore, J. S. (2014). Toward a Molecular Understanding of Energetics in Li-S Batteries Using Nonaqueous Electrolytes: A High-Level Quantum Chemical Study. *The Journal of Physical Chemistry C*. 118: 11545.
- Du, H., Zhang, Z., He, J., Cui, Z., Chai, J., Ma, J., Yang, Z., Huang, C., and Cui, G. (2017). A Delicately Designed Sulfide Graphdiyne Compatible Cathode for High-Performance Lithium/Magnesium-Sulfur Batteries. *Small*. 13: 1702277.
- Kamphaus, E. P., and Balbuena, P. B. (2017). First-Principles Investigation of Lithium Polysulfide Structure and Behavior in Solution. *The Journal of Physical Chemistry C*. 121: 21105.
- Mikhaylik, Y. V., and Akridge, J. R. (2004). Polysulfide Shuttle Study in the Li/S Battery System. *Journal of The Electrochemical Society*. 151: A1969.
- Sun, C., and Searles, D. J. (2012). Lithium Storage on Graphdiyne Predicted by DFT Calculations. *The Journal of Physical Chemistry C*. 116: 26222.
- Wang, B., Li, K., Su, D., Ahn, H., and Wang, G. (2012). Superior Electrochemical Performance of Sulfur/Graphene Nanocomposite Material for High-Capacity Lithium-Sulfur Batteries. *Chemistry – An Asian Journal*. 7: 1637.
- Wang, Y., Shen, J., Xu, L.-C., Yang, Z., Li, R., Liu, R., and Li, X. (2019). Sulfur-functionalized vanadium carbide MXene (V₂CS₂) as a promising anchoring

- material for lithium–sulfur batteries. *Physical Chemistry Chemical Physics*. 21: 18559.
- Yang, Y., Zheng, G., Misra, S., Nelson, J., Toney, M. F., and Cui, Y. (2012). High-Capacity Micrometer-Sized Li₂S Particles as Cathode Materials for Advanced Rechargeable Lithium-Ion Batteries. *Journal of the American Chemical Society*. 134: 15387.
- Zeng, Q.-W., Hu, R.-M., Chen, Z.-B., and Shang, J.-X. (2019). Single-atom Fe and N co-doped graphene for lithium-sulfur batteries: a density functional theory study. *Materials Research Express*. 6: 095620.
- Zhang, H., Xia, Y., Bu, H., Wang, X., Zhang, M., Luo, Y., and Zhao, M. (2013). Graphdiyne: A promising anode material for lithium ion batteries with high capacity and rate capability. *Journal of Applied Physics*. 113: 044309.
- Zhang, L., Liang, P., Shu, H. B., Man, X. L., Du, X. Q., Chao, D. L., Liu, Z. G., Sun, Y. P., Wan, H. Z., and Wang, H. (2018). Design rules of heteroatom-doped graphene to achieve high performance lithium–sulfur batteries: Both strong anchoring and catalysing based on first principles calculation. *Journal of Colloid and Interface Science*. 529: 426.
- Zhou, G., Tian, H., Jin, Y., Tao, X., Liu, B., Zhang, R., Seh, Z. W., Zhuo, D., Liu, Y., Sun, J., Zhao, J., Zu, C., Wu, D. S., Zhang, Q., and Cui, Y. (2017). Catalytic oxidation of Li₂S on the surface of metal sulfides for Li–S batteries. *Proceedings of the National Academy of Sciences*. 114: 840.
- Zhou, G., Yang, A., Gao, G., Yu, X., Xu, J., Liu, C., Ye, Y., Pei, A., Wu, Y., Peng, Y., Li, Y., Liang, Z., Liu, K., Wang, L.-W., and Cui, Y. (2020). Supercooled liquid sulfur maintained in three-dimensional current collector for high-performance Li-S batteries. *Science Advances*. 6: 5098.

CHAPTER VI

CONCLUSIONS

In this thesis, using a first-principles method, the role of transition metal (TM) and nitrogen co-doping on graphdiyne (GDY) as a 2D-based cathode material for Li-S batteries was studied. We explored the structural and electronic properties of the doped GDY to find the most energetically favorable configurations of TM (Co, Fe) and N-doped GDY. Two main aspects were investigated: (i) the ability of the adsorption between the reduction product (Li_2S_x , $x = 1, 2, 4, 6, \text{ and } 8$) and the substrates to assess the suppression of polysulfide dissolution, and (ii) the thermodynamically and kinetically catalytic decomposition of short-chain LiPSs (Li_2S_2 and Li_2S) on the pristine and doped GDY.

The computations reveal that the constructed substrate models of CoN_2 @GDY and FeN_2 @GDY are energetically stable by the lowest formation energies of -2.41 and -2.00 eV, respectively, where the TM center interacts with the two nearest C atoms and two substituted N atoms, which their doping concentration is consistent with experimentally characterized reports. In addition, the AIMD simulation suggests that both doped systems are still intact throughout the simulation time, leading to good stability for the TM-N-doped GDY. The electronic structures of the host GDY is changed from a semiconductor to become metal upon doping, where the additional electron on the doped substrates increases which can promote good redox activities during the charge/discharge process.

The adsorption strength of S_8 and LiPS molecules on the pristine GDY is weak van der Waals interaction for the long-chain LiPSs and strong interaction for the short-chain LiPSs. The GDY-based electrode is ineffective material to inhibit the dissolution of soluble LiPSs in both DME and DOL solvents, leading to the shuttle effect. In contrast, the adsorptivity of the substrate is substantially improved upon doping by TM and N impurity. The doped TM atom behaves as a Lewis-acid site that receives electrons transferred from S atoms on the LiPS molecules, while the doped N atoms

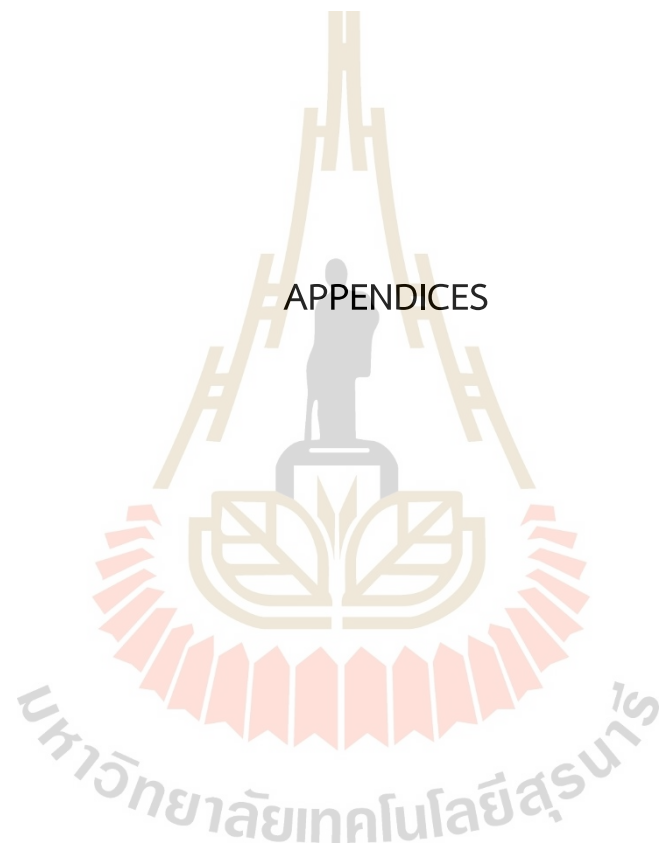
bind with Li on the adsorbates through electrostatic interaction. Such a synergetic binding contributes to the large charge migration from the adsorbates to the doped substrates, therefore, increasing the adsorption efficiency. This increased adsorption strength can dramatically suppress the dissolution of the long-chain LiPSs into the solvent, where the adsorption of the LiPSs on the doped substrates is stronger than the interaction between the LiPSs and the surrounding electrolyte molecules. Based on our results, we can suggest that the adsorption energy should be stronger than -3.00 eV to obtain significant suppression of the LiPS shuttling.

In the case of LiPS dissolution, the AIMD simulation reveals that the dissolved LiPSs interact with the solvent via Li-O bonds, where there is no decomposition throughout the simulation time. The longer chain LiPS is the higher the solubility in the ether-based solvent, especially DME. This high solubility of LiPSs may induce the shuttle effect.

Finally, the thermodynamic and kinetic decomposition of Li_2S_2 and Li_2S was investigated. We find that the decomposition on the pristine GDY is not energetically favorable and kinetically slow due to the high decomposition energy barrier and positive reaction energy. The catalytic activities were improved with the help of TM-N doped catalytic sites, which significantly reduce the barrier and provide stable reduction products. For the Li_2S_2 decomposition, the pristine GDY exhibits thermodynamically unstable ($E_r = 0.74$ eV, $E_a = 0.86$ eV), whereas the $\text{CoN}_2@GDY$ shows better catalytic behavior ($E_r = -0.36$ eV, $E_a = 0.50$ eV). For Li_2S decomposition, both $\text{FeN}_2@GDY$ ($E_r = -0.13$ eV, $E_a = 0.53$ eV) and CoN_2 ($E_r = -0.44$ eV, $E_a = 0.52$ eV) show good catalytic electrode as composed to the pristine GDY ($E_r = 0.15$ eV, $E_a = 0.54$ eV).

Overall, based on our computation, we could suggest that the presence of both TM and N doping on the 2D-carbon GDY not only prevents the dissolution of the shuttle effect by enhancing the adsorptivity of the adsorbates and the doped substrates but also promotes the LiPS decomposition by reducing the decomposition barrier, facilitating fast phase transformation during the charging process. Therefore, the $\text{FeN}_2@GDY$ and $\text{CoN}_2@GDY$ can be promising good candidates for the host cathode material of Li-S batteries.

APPENDICES



APPENDIX A

THE DOS WITH DFT+U AND BADER CHARGE DIFFERENCE

A.1 Density of state with DFT+U calculation

We calculated the PDOS of the doped substrates, using GGA+U functional where the applied U values for Fe and Co single-atom adsorbed GDY are 5.21 and 6.18 eV, respectively (He *et al.*, 2012). These calculated PDOSs show that the electronic character of the doped GDY was still metallic, which is similar to those with PBE method as shown in Figure 3.5 in the main manuscript, suggesting that the electronic properties was not changed using GGA+U or PBE method comparatively.

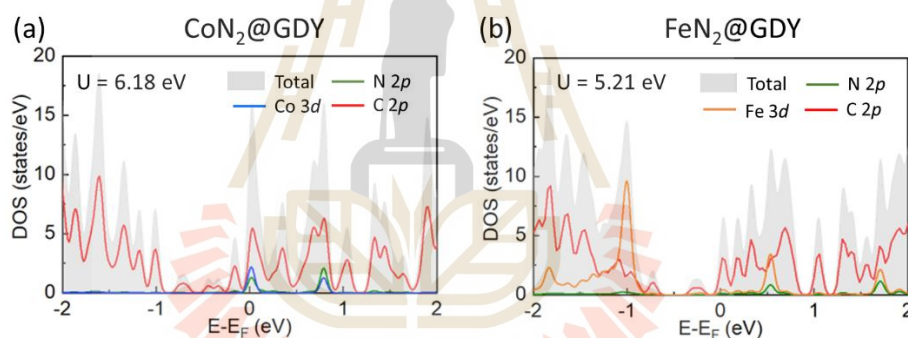


Figure A1 The projected density of state (PDOS) of (a) $\text{CoN}_2\text{@GDY}$ and (b) $\text{FeN}_2\text{@GDY}$, using DFT calculation with GGA+U method.

Reference

He, J., Ma, S. Y., Zhou, P., Zhang, C., He, C., and Sun, L. (2012). Magnetic properties of single transition-metal atom absorbed graphdiyne and graphyne sheet from DFT+ U calculations. *The Journal of Physical Chemistry C*. 116: 26313.

A.2 Bader charge difference between before and after adsorption

We analysed the charge distribution of each atom in LiPS molecules and substrates according to the adsorption systems as shown in Figure 2b-c, using Bader

0charge analysis. The Bader charge difference (Δq) upon adsorption can be calculated as the following:

$$\Delta q = q_x(\text{adsorbed}) - q_x(\text{isolated})$$

where $q_x(\text{adsorbed})$ and $q_x(\text{isolated})$ are the amount of Bader charge of X atom in substrates or LiPS molecules after and before adsorption, respectively (X = C, Co, Fe, N, Li, and S atoms). Note that the Δq of C atom is the average Bader charge distribution, whereas other atom species are individual charge distribution. The positive and negative Δq mean the charge accumulation and depletion, respectively. The labels of each atom are consistent with labeled atoms as shown in Figure S1 and S2. The corresponding charge difference are illustrated in Table A1.

Table A1 The Bader charge distribution after adsorption*.

species	CoN ₂ @GDY						FeN ₂ @GDY					
	S ₈	Li ₂ S ₈	Li ₂ S ₆	Li ₂ S ₄	Li ₂ S ₂	Li ₂ S	S ₈	Li ₂ S ₈	Li ₂ S ₆	Li ₂ S ₄	Li ₂ S ₂	Li ₂ S
Co1/Fe1	+0.023	-0.044	+0.011	+0.024	+0.010	-0.037	-0.058	-0.025	-0.086	-1.107	-0.041	-0.072
N1	+0.033	+0.014	-0.056	-0.085	-0.084	-0.135	+0.031	-0.022	-0.053	+0.002	-0.100	-0.117
N2	+0.041	+0.031	-0.032	+0.029	+0.035	+0.038	+0.034	+0.046	-0.004	+0.998	+0.007	+0.010
C _{avg}	-0.002	+0.004	+0.004	+0.005	+0.011	+0.013	-0.001	+0.004	+0.006	+0.006	+0.011	+0.013
Li1	-	+0.009	-0.005	-0.001	+0.011	+0.001	-	+0.002	-0.008	-0.005	+0.001	+0.003
Li2	-	-0.012	-0.003	-0.006	-0.012	-0.017	-	-0.010	-0.005	-0.008	-0.012	-0.016
S1	+0.001	-0.182	-0.052	-0.005	-0.080	-0.730	-0.004	-0.291	-0.058	-0.007	+0.002	-0.686
S2	+0.013	-0.023	-0.229	-0.223	-0.471	-	+0.001	-0.070	-0.183	-0.203	-0.463	-
S3	+0.018	+0.047	-0.037	-0.045	-	-	-0.001	+0.072	-0.032	-0.079	-	-
S4	-0.001	-0.051	-0.085	-0.023	-	-	-0.003	+0.099	-0.078	-0.021	-	-
S5	-0.002	-0.154	+0.062	-	-	-	-0.019	-0.164	+0.066	-	-	-
S6	+0.051	+0.072	+0.084	-	-	-	+0.104	+0.176	+0.029	-	-	-
S7	-0.021	-0.023	-	-	-	-	-0.032	-0.043	-	-	-	-
S8	-0.019	+0.046	-	-	-	-	-0.032	+0.169	-	-	-	-

*Note that the red numbers represent the amount of Bader charge distribution for the atom(s) in substrates(LiPSs) where contact with nearest other atom(s) from LiPSs(substrates). For example, Li2 in Li₂S₈ adsorbed CoN₂@GDY binds N1 atom, or S2 in Li₂S₆ adsorbed CoN₂@GDY binds Co1 atom.

APPENDIX B

PUBLICATION AND PRESENTATIONS

B.1 List of publications

Singsen, S., Fongkaew, I., Hirunsit P., and Suthirakun, S. (2022). Suppressing Polysulfides Shuttling and Promoting Sulfur Utilization via Transition Metal and Nitrogen Co-Doping on Graphdiyne Cathodes of Lithium-Sulfur Batteries: A First-Principles Modeling. *Journal of ACS Applied Energy Materials*. 5: 9722-9732.

Singsen, S., Suthirakun, S., Hirunsit P., and Balbuena, B. (2022). Surface Film Formation from Sodium Polysulfide Decomposition on Sodium-Metal Anode Surface. *The Journal of Physical Chemistry C*. 126: 166151-16626.

Singsen, S., Thasami, N., Tangpakonsab, P., Bae, H., Lee, H., Hussain, T., and Kaewmaraya, T. (2022). Transition-Metals Decorated Graphdiyne Monolayer as Efficient Sensor toward Phosphide (PH₃) and Arsine (AsH₃). *Physical Chemistry Chemical Physics*. 24: 26622-26630

Waehayee, A., Singsen, S., Duangkamol, C., Nakajima, H., Sangkhun, W., Butburee, T., Kamkaew, A., Suthirakun, S., and Siritanon, T. (2022). Interfacial Defects Induced Z-scheme Formation in Ag₃PO₄/MCo₂O₄ (M = Cu, and Zn) Heterostructures for Enhanced Dye Photodegradation and Benzylamine Selective Photooxidation. *Journal of Photochemistry and Photobiology A: Chemistry*. 430: 113956.

Khamdang, C., Singsen, S., Ngoipala, A., Fongkaew, I., Junkaew, A., and Suthirakun, S. (2022). Computational Design of a Strain-Induced 2D/2D g-C₃N₄/ZnO S-Scheme Heterostructured Photocatalyst for Water Splitting. *Journal of ACS Applied Energy Materials*. 5: 13997-14007

Jiamprasertboon, A., K a f i z a s , A., Hawkins, E., Singsen, S., Butburee, T., Wannapaiboon, S., Sangkhun, W., Nijpanich, S., Eknapakul, T., Chanlek, N., Waehayee, A., Suthirakun, S., Siritanon T. The Photocatalytic NO_x Oxidation of BiOCl Films Grown Using Aerosol-Assisted Chemical Vapor Deposition. *Journal of ACS Applied Nano Materials*. (accepted manuscript).

B.2 List of presentations

Singsen, S., Fongkaew, I., Hirunsit, P., and Suthirakun, S. (June 2022). Transition Metal and Nitrogen Co-Doped Graphdiyne as Anchoring Materials in Lithium-Sulfur Batteries: A First-Principles Study. **The 25th International Annual Symposium on Computational Science and Engineering 2022 (ANSCSE25)**. Department of Physics, Faculty of Science, Khon Kaen University, Thailand. (Poster presentation)

Singsen, S., Fongkaew, I., Hirunsit, P., and Suthirakun, S. (March 2022). Transition Metal and Nitrogen Co-Doped Graphdiyne as a Aingle-Atom Catalyst to Achieve Strong Anchoring Effect in Lithium-Sulfur Batteries. **The 9th Annual Research Chemical Engineering Graduate Student Association Symposium (ChEGSA9)**. Rudder Tower, Texas A&M University, USA. (Oral presentation)



Suppressing Polysulfides Shuttling and Promoting Sulfur Utilization via Transition Metal and Nitrogen Co-Doping on Graphdiyne Cathodes of Lithium-Sulfur Batteries: A First-Principles Modeling

Sirisaak Singsean, Ittipon Fongkaew, Pussana Hirunsit,* and Suwit Suthirakun*

Cite This: *ACS Appl. Energy Mater.* 2022, 5, 9722–9732

Read Online

ACCESS

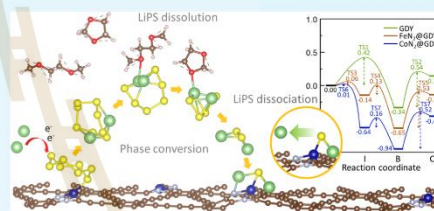
Metrics & More

Article Recommendations

Supporting Information

ABSTRACT: While lithium-sulfur (Li-S) batteries are considered the next-generation energy storage devices, several issues inhibit their commercialization, including poor conductivity, shuttling of lithium polysulfides (LiPSs), and sluggish decomposition of small LiPSs. Here, we illustrate through first-principles modeling that doping graphdiyne (GDY) with transition metal (Co, Fe) and nitrogen (TM-N) effectively suppresses the shuttle effect and enhances sulfur utilization by promoting dissociation of small LiPSs. We find that the TM-N doping provides additional electrons to the substrate, which could improve the redox activity of the substrates. The additional electrons also improve charge transfer between the substrate and adsorbate that enhances the LiPS adsorption. Electronic structure analysis reveals that the strong interactions originate from the formation of TM-S bonds and electrostatic attractions between Li and N. Such strong adsorptions prevail in the interaction between the LiPSs and electrolyte molecules; hence, the doped GDY could effectively prevent the dissolution of LiPSs and inhibit the shuttle effect. Moreover, the doped GDY substrates exhibit small barriers of Li-S and Li-N bond breaking that facilitate the decomposition of small LiPSs. This implies that TM-N-doped GDY promotes kinetics of LiPS transformation, which increases sulfur utilization and diminishes capacity fading upon charge-discharge cycles. From the computational viewpoints, the TM-N-doped GDY substrates are considered promising cathodes of Li-S batteries. This work serves as a useful guide to rationally design high-performance two-dimensional (2D) carbon-based cathode materials for Li-S batteries.

KEYWORDS: lithium-sulfur batteries, graphdiyne material, density functional theory, first-principles method, polysulfide solubility



1. INTRODUCTION

Rechargeable batteries have been widely used as efficient energy storage devices for several applications ranging from portable electronic devices to electric vehicles.¹ Among various kinds of batteries, lithium-sulfur (Li-S) batteries have been considered as next-generation rechargeable batteries^{2–4} due to their high theoretical specific capacity of 2600 Wh kg⁻¹ and energy density up to 1672 mA h g⁻¹.^{5,6} These values are much higher than the commercially used Li-ion batteries (387 Wh kg⁻¹, 155 mA h g⁻¹), Ni-H batteries (80 Wh kg⁻¹, 100 mA h g⁻¹), and Zn-air batteries (1086 Wh kg⁻¹, 820 mA h g⁻¹).^{7,8} In addition, the electrode materials are inexpensive since sulfur is naturally abundant.⁹

Upon the discharge process of the batteries, Li ions diffuse from the anode to react with S₈ (the most stable form of sulfur) at the cathode to form lithium polysulfides (LiPSs) with various Li/S ratios of Li₂S_x (x = 2, 4, 6, 8). Properties of LiPSs and their interaction with electrode materials play an important role in determining the performance of the batteries. For instance, the high capacity of the batteries can be attributed to the formation of stable LiPSs at the electrode.^{10,11} However, deep discharging leads to the formation of

electrically insulated and highly stable LiPSs including Li₂S₂ and Li₂S. Delithiation of such phases is difficult, resulting in permanent internal resistance, capacity fading, low sulfur utilization, and poor cyclability.¹² Moreover, soluble long-chain LiPSs such as Li₂S₈, Li₂S₆, and Li₂S₄ can dissolve into the electrolyte and diffuse back to the anode where the reduction of LiPSs occurs. Such a self-discharge process leads to a lowering of Coulombic efficiency, which is called the “shuttle effect”.^{13–15} These problems are major issues inhibiting the commercialization of Li-S batteries.

Many efforts have been devoted to preventing the shuttle effect and achieving long-term cycling stability. One possible solution is to find cathode materials that effectively accommodate S₈ and LiPSs with good electronic conductiv-

Received: May 6, 2022

Accepted: July 28, 2022

Published: August 9, 2022



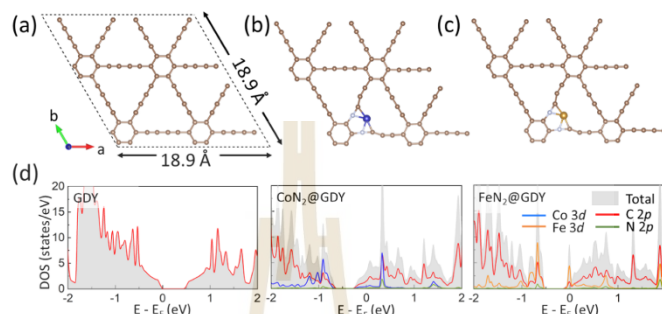


Figure 1. Optimized structure of (a) pristine GDY, (b) CoN_2 @GDY, and (c) FeN_2 @GDY, respectively, and (d) their corresponding projected density of state (PDOS). Fermi level is adjusted to 0 eV. Brown, C; light blue N; blue, Co; gold, Fe.

ity.¹⁶ Following these characteristics, carbon-based materials with different microstructures have been widely regarded as promising candidates such as graphene,^{17–20} carbon nanotube,^{21,22} porous carbon,^{23,24} and graphdiyne.^{25,26} Among them, graphdiyne (GDY) has been considered as an effective cathode material since its layered structure can provide good accommodation for S_8 and LiPSs.^{25,27,28} The sp - and sp^2 -hybridized carbon within the layer is the source of good electronic conductivity ($2.56 \times 10^{-1} \text{ S m}^{-1}$) and high carrier mobility of $2 \times 10^5 \text{ cm}^2 \text{ v}^{-1} \text{ s}^{-1}$.^{29,30} It has been reported that the GDY cathode provides a first-cycle specific capacity of 960.9 mAh g^{-1} and an almost 100% Coulombic efficiency with high reversibility.³¹ Nevertheless, the pristine GDY cathode still suffers from the shuttle effect due to the weak adsorption of S_8 /LiPSs.³²

Recently, there have been attempts to improve the adsorption of S_8 /LiPSs on the GDY cathode. Computational studies suggested that doping GDY with B, N, or Cl can significantly improve adsorption strength and charge transfer between S_8 /LiPSs and the cathode materials.^{32,33} In addition, incorporating transition metals (TMs) such as Co³⁴ and Fe³⁵ in the N-doped GDY could further improve adsorptivity and therefore suppress the shuttle effect. Such materials have successfully been synthesized yet applied for cathode materials of Li-S batteries. Previous computation also suggested that Co-doped C_2N and Fe-doped N-graphene are promising cathodes on both good anchoring and catalytic effect for Li-S batteries.^{36–38} TM and N co-doping induces strong interaction between Li and N, whereas the hybridization of TM and S atoms in the LiPSs leads to the formation of chemical bonds, which in turn increases adsorption capacity. Moreover, their electronic structures reveal enhanced electronic conductivity upon doping.³⁸

Herein, the aim of this work is to use first-principles modeling based on density functional theory to illustrate that TM-N-co-doped GDY is a promising candidate as cathode materials of Li-S batteries. Two main aspects were explored: (i) the ability to suppress the shuttle effect and (ii) the enhanced kinetics of decomposition of small LiPSs. To do this, we constructed the TM-N-doped GDY model where the doping sites and compositions were varied to yield TMN_x @GDY (TM = Co or Fe, $x = 2, 3, \text{ or } 4$). Then, we calculated their density of states to study their electronic properties including bonding characters and electronic conductivity.

Next, we adsorbed S_8 and LiPSs on the substrates and analyzed the electronic structures upon adsorption. The adsorption energies between the S_8 /LiPSs and the substrates are compared with the binding energies between LiPSs and electrolyte solvents to determine their ability to prevent the shuttle effect. Finally, we calculated the decomposition energies and barriers of small LiPSs to study the enhanced kinetics of LiPS transformation, which reflect the cyclability and sulfur utilization of the cathodes. The findings in this work provide insights into the effect of TM-N co-doping on the prevention of the shuttle effect and the enhanced sulfur utilization of the GDY cathodes. The obtained insight serves as a guide for developing two-dimensional (2D) carbon-based cathode materials of Li-S batteries.

2. COMPUTATIONAL DETAILS

All calculations were carried out using the spin-polarized DFT method as implemented in the Vienna Ab initio Simulation Package (VASP 5.3).^{39,40} The frozen-core projector augmented wave method was used to describe the electron–ion interaction.⁴¹ The valence electrons of Li 2s, C 2s2p, N 2s2p, S 3s3p, Co 3d4s, and Fe 3d4s were taken into account in a plane-wave basis with a kinetic energy cutoff of 600 eV. The exchange–correlation functional was described by the generalized gradient approximation of Perdew–Burke–Ernzerhof (PBE).⁴² Weak van der Waals interactions between the adsorbates (S_8 , Li $_2\text{S}_6$) and the substrates (GDY, TMN_x @GDY) were partially corrected using the DFT-D3 method with Becke–Johnson damping.^{43,44} To avoid interaction between periodic images, the unit cell of GDY was expanded to a 2×2 supercell with a vacuum gap of 20 Å along the z -direction. The 2×2 supercell is large enough to avoid spurious interaction between adsorbates in their periodic images as the difference of the adsorption energies calculated using the expanded 3×3 supercell is within 0.01 eV. The Brillouin zone integrations were carried out using the k -point sampling of the Monkhorst–Pack scheme⁴⁵ as $3 \times 3 \times 1$ for structural optimization and $7 \times 7 \times 1$ for electronic density of states (DOS) calculations. The ground-state energies were obtained by solving Kohn–Sham equation self-consistently until the energy difference was within 10^{-6} eV. For structural optimization, the force convergence criterion was set to 0.02 eV Å⁻¹. The charge distributions were analyzed using the Bader charge decomposition scheme.⁴⁶

Relative stabilities of doped structures were assessed by computing the formation energies, E_f , as follows³⁸

$$E_f = E(\text{TMN}_x\text{@GDY}) - \frac{x}{2}E(\text{N}_2) - E(\text{TM}) - E(\text{GDY}) + xE(\text{C}) \quad (1)$$

where $E(\text{TMN}_x\text{@GDY})$ represents the total energy of co-doped GDY with one TM atom (TM = Co or Fe) and x N atoms, $E(\text{N}_2)$ is the total energy of an isolated N_2 molecule, $E(\text{TM})$ is the total energy of a single metal atom, $E(\text{GDY})$ is the total energy of perfect GDY, and $E(\text{C})$ is the total energy per carbon atom of the perfect GDY.

To study the stability of LiPS molecules in the electrolyte solvents, we carried out ab initio molecular dynamics (AIMD) simulations of large LiPS molecules dissolved in 2-dimethoxyethane (DME) and 1,3-dioxolane (DOL) solvents. The simulations were carried out using the NVT ensemble of Nose–Hoover thermostat with a time step of 5 fs for 5 ps at 300 K. To lower the expense of the calculations, we used Γ -point only for k-point sampling with an energy cutoff of 450 eV. The volume of the explicit solvent system was set to $15 \times 15 \times 15 \text{ \AA}^3$ containing one LiPS molecule at the center of the box surrounded by the solvent molecules. The number of solvent molecules was calculated corresponding to the density of liquid solvent of DME (0.87 g cm^{-3}) and DOL (1.06 g cm^{-3}) at room temperature.

3. RESULTS AND DISCUSSION

3.1. Geometric and Electronic Properties of Pristine and Co-Doped GDY. A pristine GDY monolayer comprises a series of sp- and sp²-hybridized carbon atoms. Its 2D structure is derived from graphene with two units of acetylenic linkages ($-\text{C}\equiv\text{C}-$, sp components) that connect two adjacent sp² carbon atoms, as shown in Figure 1a. Its unit cell exhibits a hexagonal symmetry with the experimentally measured lattice parameter of 9.458 \AA .⁴⁷ From the unit cell, we constructed a 2×2 supercell containing 72 C atoms to use as a model substrate where its optimized supercell parameter of 18.924 \AA agrees with the experimental value of 18.916 \AA .⁴⁷ The calculated bond distances of sp² carbon (1.432 \AA) and the acetylenic linkages (1.396 , 1.232 \AA) also match with those reported in the previous DFT-PBE study⁴⁸ with differences less than 0.1%.

Although the TM-N-co-doped GDY materials were successfully synthesized, their structural information regarding the doping sites of both metal and nitrogen remains unclear. Characterizations using X-ray photoelectron spectroscopy (XPS) reveal possible configurations of nitrogen atoms at acetylenic linkage with the concentration of nitrogen in the range of 2.99–5.39%, where the transition metal, Co or Fe, can be adsorbed nearby the doped N sites. Hence, in this work, we considered various configurations of TM- and N-co-doped GDY where the number of N atoms was varied from two to four atoms yielding the N concentrations of 2.78–5.56% corresponding to the synthesized concentrations.^{34,35} Computations reveal that the preferred configurations involve two N atoms substituted at the acetylenic linkage next to the sp² carbon where the TM atom strongly binds with two N atoms and two sp C atoms, as shown in Figure 1b,c, and discussed in Supporting Information Section S1. Such configurations exhibit the lowest formation energies of -2.41 and -2.00 eV for $\text{CoN}_2\text{@GDY}$ and $\text{FeN}_2\text{@GDY}$, respectively. The other

configurations with different numbers of doped N atoms are at least 0.32 eV less stable (see SI Section S1).

In addition, we calculated the adsorption energies, $E_{\text{ads, TM}}$, of TM on the N-doped GDY to determine the stability of TM anchoring using the following equation⁴⁹

$$E_{\text{ads, TM}} = E_{\text{TMN}_x\text{@GDY}} - E_{\text{N}_x\text{@GDY}} - E_{\text{TM}} \quad (2)$$

where $E_{\text{TMN}_x\text{@GDY}}$, $E_{\text{N}_x\text{@GDY}}$, and E_{TM} denote the total energy of TM-N-co-doped GDY, N-doped GDY, and an isolated Co or Fe atom, respectively. We find that the TM atom effectively anchors to the N-doped GDY at the N doping sites as shown by their strong adsorption energies for both Co ($E_{\text{ads, TM}} = -6.64$ eV) and Fe ($E_{\text{ads, TM}} = -8.94$ eV). Therefore, such configurations of $\text{CoN}_2\text{@GDY}$ and $\text{FeN}_2\text{@GDY}$ were used as the doped substrate models.

We further examined the thermal stability of the chosen doped models using AIMD simulation with the NVT ensemble at 300 K for 10 ps. As detailed in SI Section S2, the result reveals that both $\text{CoN}_2\text{@GDY}$ and $\text{FeN}_2\text{@GDY}$ are still intact with the vibration of the adsorbed TM atom around the equilibrium position, suggesting good stability of the TM-N-doped substrates.

To explore the effects of TM-N doping on the electronic properties of the host cathodes, we calculated and analyzed their projected density of states, PDOS, (Figure 1d) and band structure (Figure S4). The PDOS and band structure of pristine GDY exhibits a semiconducting character with a direct band gap of 0.47 eV, which is consistent with previous DFT-PBE calculation.⁵⁰ The calculated band gap is lower than that of the experimental value (0.6 – 1.0 eV)⁵¹ due to the well-known self-interaction error of the DFT formalism. In addition, to test if the electronic structure of the doped GDY could be changed with the applied Hubbard U correction, we calculated their PDOS using the PBE + U method. The U values for Fe and Co are 5.21 and 6.18 eV, respectively.⁵² As described in SI Section S4, the PDOS exhibit their Fermi level in the band, which is consistent with those calculated using the PBE method. Upon doping, extra electrons from the TM and N dopants partially fill in the conduction band leading to the shifts of Fermi level into the conduction band, which is consistent with the calculated band structure (Figure S4). The features of the top of the valence band and bottom of the conduction band show significant hybridization between TM 3d and C 2p states with non-negligible contribution of N 2p states suggesting strong interactions between the TM- and N-doped GDY. From the atomistic viewpoint, the TM-N co-doping provides additional electrons that could facilitate redox processes of the cathode upon charge–discharge cycles. Similar effects have been reported in a previous computational work that TM doping increases the conductivity of the C_2N host and improves the redox activity of Li-S batteries.³⁶

3.2. Adsorption of S_8 /LiPSs on the Pristine and Doped GDY. Next, we examined the adsorption of S_8 and LiPSs on the pristine and doped GDY to explore the effect of doping on the prevention of the shuttle effect. The greater the adsorptivity is, the less likely the LiPSs is to redissolve into the electrolyte. First, we searched for the most stable adsorbed configurations and adsorption sites. The optimized molecular structures of S_8 and LiPSs are detailed in SI Section S5. The adsorption energy, E_{ads} , can be calculated using the following equation,³⁶ where all stable adsorbed configurations and their adsorption energies are summarized in Figure 2

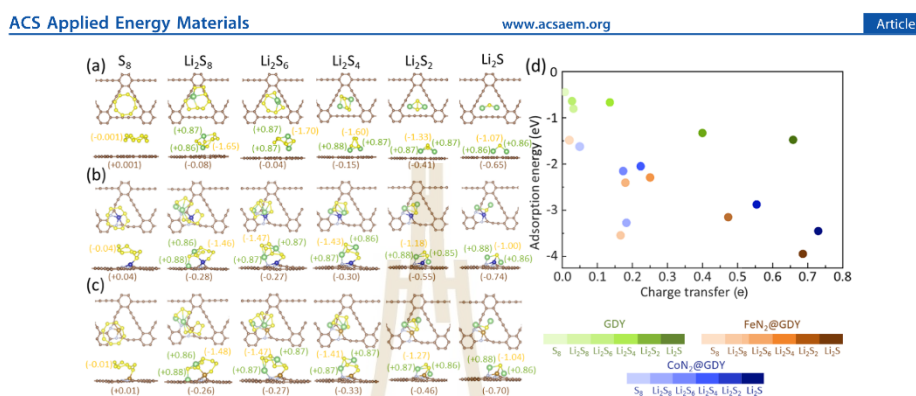


Figure 2. Top and side views of the most stable adsorption configurations of S₈ and LiPSs on (a) pristine GDY, (b) CoN₂@GDY, and (c) FeN₂@GDY. (d) Correlation between S₈/LiPSs adsorption energy and degree of charge transfer to substrate. Brown, C; light blue, N; yellow, S; green, Li; blue, Co; gold, Fe. Charges of each Li atom, all S atoms, and the substrate are labeled in green, yellow, and brown numbers, respectively.

$$E_{\text{ads}} = E_{S_8/\text{LiPSs}+\text{sub}} - E_{\text{sub}} - E_{S_8/\text{LiPSs}} \quad (3)$$

where $E_{S_8/\text{LiPSs}+\text{sub}}$ is the total energy of the adsorbed S₈/LiPSs systems, E_{sub} is the total energy of the substrate, and $E_{S_8/\text{LiPSs}}$ is the total energy of an isolated S₈/LiPSs molecule.

For the adsorption on the pristine GDY substrate, we find that most favorable adsorption sites are at the hollow site of the large triangle pore, as shown in Figure 2a. The adsorption energies of S₈ (−0.44 eV) and large LiPS molecules, including Li₂S₈ (−0.81 eV), Li₂S₆ (−0.64 eV), and Li₂S₄ (−0.67 eV), indicate relatively weak interaction between the molecules and the pristine GDY, as shown in Figure 2d. Stronger adsorption is predicted for small LiPS molecules where the adsorption energies of Li₂S₂ (−1.33 eV) and Li₂S (−1.48 eV) are much stronger. It can be seen that increasing the ratio of Li/S in the LiPS molecules improves the adsorptivity. In other words, LiPSs at late discharge states (Li₂S₂ and Li₂S) bind more strongly with the GDY host.

We analyzed the charge distribution of LiPSs and the GDY substrate to further describe the increased adsorptivity along the discharge process. As shown in Figure 2a, before the discharge process, the S₈ molecule weakly adsorbs on the GDY substrate ($E_{\text{ads}} = -0.44$ eV) with negligible charge transfer less than 0.01 e. During the early discharge process, Li reacts with S₈ to form Li₂S₈ and Li₂S₆, which bind more strongly to the substrate. Two Li atoms in the Li₂S₈ and Li₂S₆ molecules consistently exhibit a positive charge of +0.9 e per atom where their electrons are mainly accumulated at the electronegative S atoms with a total charge of −1.7 e and slightly transferred to the substrate of up to −0.1 e. The preferred adsorbed configurations of Li₂S₈ and Li₂S₆ exhibit the paralleled orientation where only one Li atom is interacting with the substrate.

At intermediate and late discharge states, the cathode contains higher Li concentrations with a formation of smaller LiPSs including Li₂S₄, Li₂S₂, and Li₂S. We find that Li in these small LiPSs still maintains its positive charge of +0.9 e per atom. However, electrons from the positively charged Li are now distributed at S in the LiPS molecules (varied from −1.1 to −1.6 e) and at the GDY substrate (varied from −0.2 to −0.7 e). This is because smaller LiPS molecules contain lower

amounts of electronegative S that they cannot hold the electrons of Li and therefore the excess electrons are transferred to the substrate. The charge transfer leads to strong Coulombic interaction between the positively charged Li and the negatively charged GDY that these LiPSs have their two Li atoms binding with the substrate. The adsorption strength corresponds well with number of electrons transferred, as shown in Figure 2d. The smaller the LiPS molecule, the greater the amount of charge transferred and the stronger the adsorption. Nevertheless, the adsorptions on the pristine GDY substrate are still relatively weak, especially for the large LiPS molecules.

Adsorptivity is substantially improved upon doping. As shown in Figure 2b,c, S₈/LiPSs prefer to strictly adsorb at the TM and N doping sites. The adsorption energies of all molecules become significantly stronger by at least −1.60 and −1.47 eV for adsorption on CoN₂@GDY and FeN₂@GDY, respectively, as illustrated in Figure 2d. Also, the improved adsorptivity correlates with the degree of charge transfer. Such strong interactions can be attributed to the presence of both TM and N active sites, which play synergistic roles in improving the stability of the adsorbed molecules. As shown in Figure 2b,c, the adsorbed structures reveal that the doped TM atom acts as a Lewis acid site that binds with an electron-rich S atom of the LiPS molecules, whereas the electronegative N atoms strongly interact with the Li atom(s) of the LiPS molecules (see more details in SI Section S6). The structures of the adsorbed S₈/LiPSs are changed compared with their isolated molecules (see Figure S6). The bond distances of Li–S bonds are mostly increased by at least 0.12 Å, whereas those of S–S bonds in LiPSs are decreased by at least 0.11 Å upon adsorption (see Tables S1 and S2). In particular, some S–S and Li–S bonds in the adsorbed Li₂S₈ on the doped GDY are broken with their breaking distance of 2.53 and 4.17 Å, respectively. This agrees with the experimental observation that, during the discharge process, Li₂S₈ readily accepts electrons and is depleted quickly by transforming to other phases.⁵³ Moreover, it can be seen that adsorptions on the FeN₂@GDY are somewhat stronger than those on the CoN₂@GDY. This may be due to the higher numbers of unoccupied 3d states of Fe, which makes Fe the better Lewis acid, leading

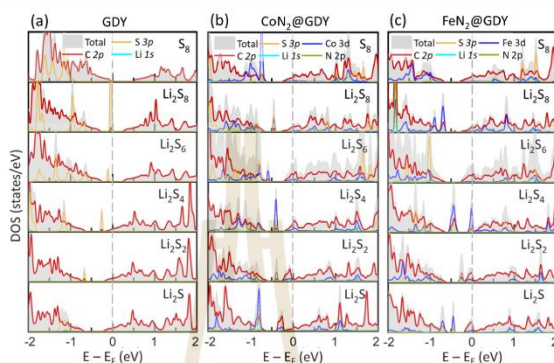


Figure 3. Projected density of state (PDOS) of S_8 /LiPSs adsorption on (a) pristine GDY, (b) CoN_2 @GDY, and (c) FeN_2 @GDY. The Fermi level (E_f) is adjusted to 0 eV.

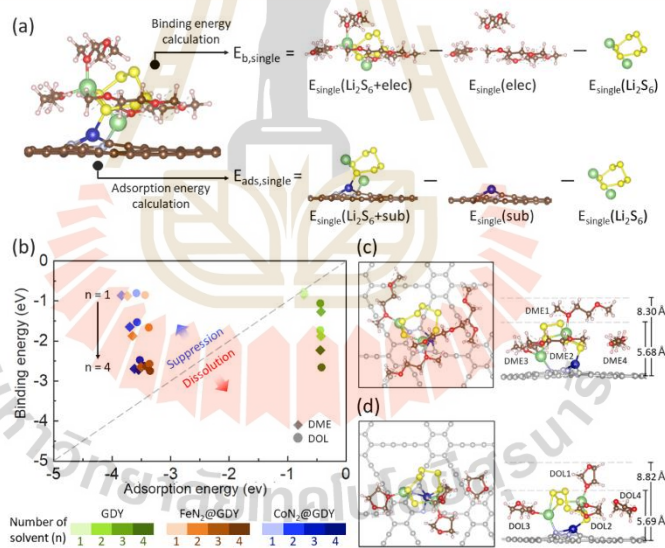


Figure 4. Schematic illustration of (a) the computations of adsorption energy ($E_{ads,single}$) and binding energy ($E_{b,single}$), (b) the comparison between $E_{ads,single}$ and $E_{b,single}$ to predict the suppression of shuttle effect and dissolution of LiPS. Co-adsorbed configuration of Li_2S_6 on CoN_2 @GDY in the presence of (c) DME or (d) DOL molecules. The labeled distances identify the vertical distance from the substrate to the topmost of the electrolyte molecules. Gray, GDY; brown, C; light blue, N; yellow, S; green, Li; white, H; blue, Co; gold, Fe; red, O.

to strong Lewis acid–base interaction between the molecules and the doped substrates. This explanation is consistent with the previous DFT-PBE calculations that transition metals, on the N-doped graphene, with lower unoccupied 3d orbitals weakly bind to the LiPS molecules as demonstrated through the series of first-row transition metals (Cr to Cu).³⁷ Interestingly, our calculated results of these co-doped GDY display better adsorptivity (1.4–3.9 eV) than those reported in previous theoretical studies within DFT-PBE description

where the reported adsorption energies on TM-N-co-doped graphene are in the range of 0.9–2.5 eV for large LiPS molecules.^{35,36}

To obtain insights into the bonding characters between molecules and the substrates, we further analyzed their PDOS. As shown in Figure 3a, PDOS of the adsorbed pristine GDY systems exhibits only a small overlap between the adsorbed molecular states (Li 2s and S 3p) and the C 2p states of the substrate. Such negligible overlaps imply no chemical

interaction between the adsorbed molecules and the GDY substrate. In contrast, adsorptions on the doped GDY exhibit significant hybridization between the S valence states and the doped TM 3d states. One example includes the PDOS of Li_2S_6 adsorbed CoN_2 @GDY, which displays a large overlap of S 3p and Co 3d states in the energy range of -0.8 to 1.5 eV (Figure 3b). The other example is the Li_2S_6 adsorbed FeN_2 @GDY system showing the overlap of S 3p and Fe 3d states in the energy range between -0.7 and 0.8 eV (Figure 3c).

In addition, the adsorption is enhanced by the electrostatic interaction between positively charged Li and the highly electronegative N site on the substrate. Bader charge analysis reveals that Li in LiPS molecules exhibits a positive charge of $+0.9$ e, whereas the doped N sites display negative charge in the range of -1.1 to -1.2 e for the doped GDY systems (see SI Section S7). The analysis is consistent with the PDOS of the adsorbed systems that the overlap between Li and N states is negligible since no covalent bond is formed.

Overall, we illustrated through the PDOS and charge analyses that the doped TM center acts as a Lewis acid site that strongly binds with the S moieties, whereas the doped N sites and Li interact via a Coulombic force. Such combined TM-N active sites significantly improve the adsorption of S_8 and LiPS molecules, which could further enhance the capacity of the electrode. In addition, the PDOS of the doped systems with S_8 /LiPSs adsorption reveals relatively populated states at the Fermi level, suggesting that the systems are electron-rich, which can facilitate the redox reaction of the lithiation process.⁵⁴

3.3. Suppression of Shuttle Effect by TM-N Anchoring. The strong interaction between the electrolyte molecules and the LiPSs is the major contribution leading to LiPS dissolution and the shuttle effect.^{55–57} One strategy used to inhibit such processes is to enhance the adsorptivity between the LiPS molecules and the electrode substrates.⁵⁸ As discussed in the previous section, TM-N co-doping improves the adsorption strength between the LiPSs and the GDY substrates. In this section, we further explored how TM-N doping can help suppress the shuttle effect.

Herein, we examined the adsorptivity of LiPSs on the pristine and doped GDY substrates in the presence of the electrolyte molecules. The Li_2S_6 molecule was chosen to represent the LiPSs that are prone to dissolution due to its weak adsorption energy, as illustrated in the previous section. In addition, it has been experimentally reported that Li_2S_8 is quickly transformed to other LiPSs, whereas Li_2S_6 is more stable and generally found during the charge–discharge cycles.⁵³ We chose 1,2-dimethoxyethane (DME) and 1,3-dioxolane (DOL) as ether-based electrolyte solvents since they are commonly used as liquid electrolyte for Li-S batteries. These electrolytes are compatible with the standard salt (LiTFSI) and exhibit poor solvation to LiPS compared with the carbonate-based electrolytes.^{59–61} The co-adsorbed systems include the adsorbed Li_2S_6 molecule on the substrates surrounded by up to four molecules of DME or DOL electrolyte. Additional electrolyte molecules do not directly interact with the adsorbed Li_2S_6 molecule (see SI Section S8). As shown in Figure 4, the DME/DOL molecules prefer to bind with the Li_2S_6 molecule through the Li–O interaction, where one Li_2S_6 molecule can coordinate with three electrolyte molecules in the first solvation shell. The Li–O distances are in the range of 1.95 – 2.10 Å. The fourth electrolyte molecule

stays at the outer solvation shell with the Li–O distance farther than 3.84 Å.

To systematically determine the suppression of the shuttle effect, we compare the adsorption energies between the Li_2S_6 molecule and the substrate with the effect of surrounded electrolyte molecules, $E_{\text{ads, single}}$, with the binding interaction energies between the Li_2S_6 and the electrolyte molecules, $E_{\text{b, single}}$, as schematically shown in Figure 4a.⁶² The corresponding $E_{\text{ads, single}}$ can be calculated as follows

$$E_{\text{ads, single}} = E_{\text{single}}(\text{Li}_2\text{S}_6 + \text{sub}) - E_{\text{single}}(\text{sub}) - E_{\text{single}}(\text{Li}_2\text{S}_6) \quad (4)$$

where $E_{\text{single}}(\text{Li}_2\text{S}_6 + \text{sub})$ is the calculated single-point energy of the adsorbed Li_2S_6 substrate obtained from the optimized solvated co-adsorbed configuration but removing the electrolyte molecules. $E_{\text{single}}(\text{sub})$ and $E_{\text{single}}(\text{Li}_2\text{S}_6)$ are the calculated single-point energies of the substrate and an individual Li_2S_6 molecule, respectively. The binding interactions between the Li_2S_6 and the electrolyte molecules, $E_{\text{b, single}}$, are calculated using the following equation

$$E_{\text{b, single}} = E_{\text{single}}(\text{Li}_2\text{S}_6 + \text{elec}) - E_{\text{single}}(\text{elec}) - E_{\text{single}}(\text{Li}_2\text{S}_6) \quad (5)$$

where $E_{\text{single}}(\text{Li}_2\text{S}_6 + \text{elec})$ and $E_{\text{single}}(\text{elec})$ are the calculated single-point energy of the optimized Li_2S_6 surrounded by electrolyte molecules but removing the substrate and the calculated single-point energy of electrolyte molecules, respectively. Then, $E_{\text{ads, single}}$ and $E_{\text{b, single}}$ were compared to determine the dissolution of the Li_2S_6 molecule. If $E_{\text{ads, single}}$ is stronger (more negative) than $E_{\text{b, single}}$ adsorption prevails, where the shuttle effect is suppressed, otherwise the dissolution is predicted.

As shown in Figure 4b, the pristine GDY is considered an ineffective electrode material to inhibit the shuttle effect because the interaction between the Li_2S_6 and the electrolyte is stronger than those of the adsorption on the substrate at all electrolyte contents for both DME and DOL electrolytes. As a result, the dissolution of Li_2S_6 is expected even at low contact of one surrounding electrolyte molecule.

The shuttle effect can be significantly suppressed with the help of TM-N doping. As shown in Figure 4b, while the binding energies are maintained in the range of -0.85 to -2.74 eV, the adsorption strength between the Li_2S_6 molecule and the substrates is greatly improved by at least -3.35 eV upon TM-N doping. Thus, the enhanced adsorptivity dramatically lowers the dissolution of the LiPS molecules. Based on our computations, to effectively prevent the dissolution, it is suggested that the adsorption strength between the candidate cathode material and LiPS molecules should be more negative than -3.0 eV. It is noted that, in this study, we only explored the suppression of the shuttle effect on monolayer GDY substrates. The required adsorption strength to suppress the dissolution may vary if we consider the LiPS adsorption in other systems such as multilayer systems. For example, previous computational studies of LiPS adsorptions on graphene⁶² and GDY-based electrodes³² reported that the adsorption strength can be improved by reducing the interlayer spacing. As shown in Figure 4c,d, the vertical distance of electrolyte adsorption on the substrate could be used to suggest that the interlayer spacing should be in the range of 6 –

9 Å. Such interlayer gaps can confine the Li_2S_6 molecule and limit the direct electrolyte contact with up to two electrolyte molecules in the first solvation shell. The interlayer spacing larger than 9 Å leads to greater exposure of more electrolyte molecules, which could lead to the dissolution of LiPSs.

3.4. Solubility of the Soluble LiPS in Electrolyte Solution. As previously discussed, the dissolution and shuttling of large LiPSs from the cathode to the anode leads to a low Coulombic efficiency of the batteries.^{13,63} To better understand the behavior of LiPS dissolution, we study the solvation of large LiPS molecules in the DME/DOL electrolytes by carrying out the AIMD simulations. Low-energy configurations were chosen from the AIMD results for further geometry relaxation using DFT to obtain the ground-state structures and energies. As shown in Figure 5, one LiPS

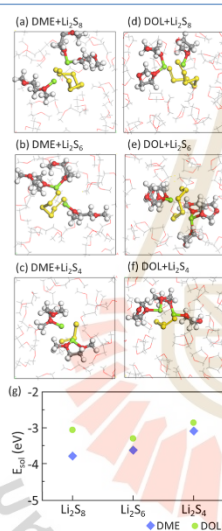


Figure 5. Low-energy configurations of (a–c) DME- and (d–f) DOL-solvated LiPSs as obtained from AIMD simulations with (g) their corresponding solvation energies. Illustrations in the ball-and-stick model represent electrolyte molecules in the first solvation shell, whereas the wireframe models are the outer solvation shell.

molecule (Li_2S_8 , Li_2S_6 , or Li_2S_4) can directly interact with at most three DME or five DOL molecules in the first solvation shell. We calculated the solvation energies, E_{solv} , to determine the interactions between the dissolved LiPS molecules and the electrolytes as follows

$$E_{\text{solv}} = E_{\text{LiPS+solv}} - E_{\text{LiPS}} - E_{\text{solv}} \quad (6)$$

where $E_{\text{LiPS+solv}}$ is the total energy of the optimized LiPS molecule surrounded by solvent molecules, E_{LiPS} is the total energy of an isolated LiPS (Li_2S_8 , Li_2S_6 , or Li_2S_4) molecule, and E_{solv} is the total energy of the optimized solvent molecules (DME or DOL) in the simulation box.

As shown in Figure 5a–f, the optimized LiPS molecules still maintain their molecular structures without any dissociations of chemical bonds indicating good stabilities in the electrolyte

environment. Nevertheless, elongations of Li–S bonds, in the range of 2.27–2.65 Å, are observed due to strong interactions between the Li moieties and the O atoms of the electrolyte molecules as illustrated through highly negative E_{solv} in Figure 5g. Such strong interactions signify the solubility of LiPS molecules in the electrolyte media. Generally, E_{solv} tends to be more negative at high S contents, indicating that the large LiPS molecules can be easily dissolved in the electrolyte. The calculated results agree very well with the experimental observations that the solubility tends to increase with the molecular size of LiPSs.¹³ In addition, the E_{solv} in DME are generally more negative than those in DOL electrolyte, implying that LiPSs better dissolve in the DME electrolyte. The high solubility of LiPSs in DME may promote LiPS dissolution, leading to an undesired shuttle effect.

3.5. Dissociation and Diffusion of Li Ions from the End Products of LiPSs. We have shown in the previous sections that TM-N doping significantly improves adsorptivity of the GDY substrates and effectively prevents the dissolution of large LiPSs and the shuttle effect. In this section, we further investigated the role of TM-N doping to enhance sulfur utilization by studying the decomposition of small LiPSs. As discussed earlier, the irreversible phase transformation of small LiPSs is the main reason for capacity fading, low sulfur utilization, and the low-cycle life of Li-S batteries.¹² Such difficult conversion of small LiPSs originates from the high activation energies of LiPS decomposition leading to slow oxidation kinetics of the charge process. As a result, lowering the activation energies with the help of catalysts is expected to accelerate the phase transformation process and promote oxidation kinetics. Here, we study the decomposition mechanisms of small LiPSs including Li_2S_2 and Li_2S on the pristine and doped GDY using the CI-NEB method. In addition, we explored the catalytic role of the doped TM-N centers toward decomposition kinetics.

As shown in Figure 6a,b, the decomposition of Li_2S_2 and Li_2S is a two-step process including (i) dissociation of Li–S bonds ($A \rightarrow B$) and (ii) diffusion of Li to the stable adsorption site ($B \rightarrow C$). Note that the presented mechanisms are the most favorable pathways, whereas other high-energy paths are detailed in SI Section S9. Computations reveal that, over the pristine GDY, the bond breaking of Li_2S_2 is difficult that it has to overcome a high barrier (E_a) of 0.86 eV with an endothermic reaction energy (E_r) of 0.73 eV. This is because this step involves breaking two Li–S bonds, as shown in Figure 6c. The subsequent step of Li diffusion exhibits a much lower barrier of 0.11 eV with a nearly thermoneutral reaction energy. It is obvious that the Li–S bond breaking is the rate-determining step where the overall process displays an effective barrier of 0.86 eV.

The presence of doped TM-N center greatly improves the kinetics of the difficult decomposition process by weakening the interaction within the Li_2S_2 molecule and changing the decomposition mechanism. First, the strongly adsorbed Li_2S_2 on the doped GDY weakens the Li–S bonds, in turn lowering the barrier of Li–S bond breaking yielding the LiN and LiS_2 -TM intermediates, as shown in Figure 6c. Next, for Li to diffuse, the Li–N bond breaking must take place where the Li atom moves to the stable adsorption site. Interestingly, the FeN_2 and CoN_2 active sites affect the dissociation quite differently. In particular, dissociation on the FeN_2 system exhibits all uphill processes for both Li–S ($E_r = 0.29$ eV, $E_a = 0.41$ eV) and Li–N bond breaking ($E_r = 0.20$ eV, $E_a = 0.40$

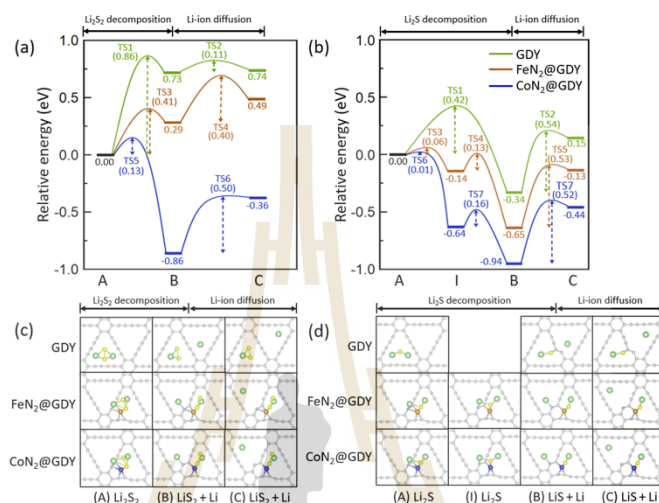


Figure 6. Potential energy profiles of (a) Li_2S_2 and (b) Li_2S decompositions on GDY (green line), CoN_2 @GDY (blue line), and FeN_2 @GDY (yellow line), and their corresponding intermediates for (c) Li_2S_2 and (d) Li_2S decompositions. The labeled numbers at the intermediate states indicate their relative energies, whereas the numbers in parentheses denote the energy barriers.

eV). The overall process yields a reaction energy of 0.49 eV with an effective barrier of 0.69 eV (0.29 + 0.40) for Li_2S_2 on FeN_2 @GDY.

In contrast, for the CoN_2 doped system, the dissociation of Li–S bonds on Li_2S_2 displays a small barrier of only 0.13 eV with an exothermicity of 0.86 eV due to the formation of stable intermediate. The subsequent step of Li–N bond breaking is endothermic by 0.50 eV, where the barrier is of the same magnitude (0.51 eV). The overall reaction energy is exothermic by 0.36 eV, where the effective barrier is limited by the Li–N bond breaking of 0.51 eV. The dissociated Li in the CoN_2 system is more stable than that in the FeN_2 system because it moves to the most stable site into the triangle pore of the CoN_2 system. On the other hand, in the FeN_2 system, the Li atom locates at 0.96 Å above the triangle pore (see Figure S12). To conclude, TM–N doping changes the Li_2S_2 decomposition mechanisms and reduces its effective barrier from 0.86 eV for the pristine GDY to 0.69 and 0.50 eV for FeN_2 and CoN_2 @GDY, respectively. The overall reaction energy is also reduced from 0.74 eV on the pristine GDY to 0.49 and –0.36 eV for FeN_2 and CoN_2 @GDY, respectively.

Unlike Li_2S_2 , decomposition of Li_2S is thermodynamically and kinetically more favorable even when the reaction takes place in the absence of the TM–N centers. As shown in Figure 6b, the Li–S bond breaking on the pristine GDY exhibits a lower energy barrier of 0.42 eV with an exothermicity of 0.34 eV. Such a relatively easy step is due to the formation of a stable Li–S intermediate where S chemically binds with the sp C of the GDY substrate with the S–C bond distance of 1.75 Å, as illustrated in Figure 6d. Bader charge analysis reveals that the decomposed Li_2S exhibits greater charge transfer to the substrate (1.3 e) compared with the adsorbed state (0.7 e). The greater degree of charge transfer well correlates with the highly stable decomposed Li_2S intermediate. The subsequent

step, Li diffusion, is energetically uphill by 0.49 eV with a barrier of 0.54 eV. The overall decomposition process is slightly endothermic by 0.15 eV with an effective barrier of 0.54 eV belonging to the Li diffusion step. The results are interesting because the rate-limiting step is not the Li–S bond breaking which is typically reported as a kinetically difficult step for Li_2S_2 decomposition in this study and Li_2S decomposition on other studied cathode materials.^{54,64} We find that the formation of stable Li–S–GDY intermediate through the strong S–C(sp) bond is the main contribution to such enhanced kinetics. Note that the sp C presented in the acetylenic linkages is one of the unique properties of GDY that could be the origin of the facile decomposition of small LiPSs. In particular, our study reveals that the effective barrier of Li_2S decomposition on GDY (0.54 eV) is significantly lower than that on graphene (1.81 eV),⁶⁵ suggesting the better transformation of LiPSs and high S utilization. This is consistent with the experimental results that the GDY cathode exhibits a higher energy capacity (713.7 mA h g^{–1} at 100 cycles)³¹ than graphene cathodes (662 mA h g^{–1} at 100 cycles).⁶⁶

In the presence of the doped TM–N centers, the Li_2S decomposition is thermodynamically more favorable. The TM–N doping changes the behavior of Li_2S adsorption, resulting in alternative decomposition mechanisms. As shown in Figure 6b,d, Li–S bond cleavage is now a two-step process where the Li–S bond elongation and reorganization of the Li_2S molecule take place before breaking the Li–S bond. These steps are strongly exothermic with small barriers for both FeN_2 ($E_t = -0.65$ eV, $E_a = 0.13$ eV) and CoN_2 ($E_t = -0.94$ eV, $E_a = 0.16$ eV) systems. The following step of Li–N bond breaking is endothermic with higher barriers for FeN_2 ($E_t = 0.52$ eV, $E_a = 0.53$ eV) and CoN_2 ($E_t = 0.50$ eV, $E_a = 0.52$ eV) systems. Overall, both systems yield thermodynamically favored products where their reaction energies are exothermic by

0.13 and 0.44 eV for FeN₂ and CoN₂ systems, respectively, which are more favorable than the endothermic reaction energy for the pristine GDY (0.15 eV). Its kinetics remains unchanged as the effective barriers of the FeN₂ (0.53 eV) and CoN₂ (0.52 eV) systems are very similar to that of the pristine system (0.54 eV). Our calculated effective barriers are comparable to those calculated for Li₂S decomposition in other cathode materials such as V₂CO₂ (0.43 eV),⁵⁴ SnS₂ (0.50 eV),⁶⁵ and Ti₂CS₂ (1.51 eV).⁶⁷ In addition, the decomposition of Li₂S₂ and Li₂S on the doped GDY is energetically more favorable than those on the Co/FeN₄@graphene where the overall reaction energies of the doped GDY are at least 1.03 eV more favorable.^{37,38} The calculated results suggest that the TM-N-doped GDY facilitates the decomposition of small LiPS molecules, which could improve energy density, cyclability, and S utilization of the electrode.

In addition, Li diffusion on the pristine GDY was also considered (see SI Section S10). It is reasonable to assume that such diffusion occurs far from the active site in the doped systems. From the result, Li ion diffuses with a small diffusion barrier of 0.10 eV for movement among nearby favorable sites in the same triangle pore. The barrier is much higher (0.61 eV) for Li to jump across an acetylenic linkage to the next triangle pore. The calculated barriers are in a similar order to those DFT-calculated values of the 2D carbon-based cathode materials including graphene (0.48 eV)⁶⁸ and graphyne (0.72 eV).⁶⁹ Nevertheless, such moderate barriers should be easily overcome at an operating potential of 3.45 V for initial charging conditions.⁷⁰

4. CONCLUSIONS

In this work, we used a first-principles method to study the role of TM-N doping on (i) the suppression of shuttle effect and (ii) promotion of small LiPS decomposition on GDY-based electrodes of Li-S batteries. The constructed models are based on the experimentally characterized TM (Fe, Co)-N-co-doped GDY where the TM center binds with two C atoms and two substituted N atoms at the acetylenic chain. The models are further used for the adsorption study of S₈/LiPSs and co-adsorption of Li₂S₈ with electrolyte molecules. The calculated results reveal that TM-N-doped GDY systems exhibit improved adsorptivity of S₈/LiPS molecules. In particular, the TM center acts as a Lewis acid site that binds with the S atoms while the doping N atom interacts with Li of the adsorbate via electrostatic attraction. Such a binding mode induces greater charge transfer between the molecules and the substrates, thus increasing the adsorption strength. The increased adsorptivity of the doped substrates helps suppress the LiPS dissolution into the electrolyte, which is determined by comparing the adsorption energy and electrolyte-LiPS binding energy. Based on our results, it is suggested that the doped substrates effectively suppress the dissolution of LiPSs where the adsorption energies should be stronger than -3.00 eV. Finally, the catalytic role of TM-N centers on the decomposition of small LiPS was determined. We find that the decomposition of Li₂S₂ and Li₂S on the pristine GDY is thermodynamically unfavorable and kinetically sluggish. The doped TM-N centers act as catalytic sites that weaken the Li-S bonds and alter the decomposition mechanisms, which in turn improves their kinetics. In particular, the highly endothermic reaction of Li₂S₂ decomposition on pristine GDY ($E_r = 0.74$ eV, $E_a = 0.86$ eV) has become thermodynamically favored and kinetically more facile in the presence of

CoN₂ center on the substrate ($E_r = -0.36$ eV, $E_a = 0.50$ eV). Interestingly, the decomposition of Li₂S on the pristine GDY is already kinetically facile but thermodynamically challenged ($E_r = 0.15$ eV, $E_a = 0.54$ eV). The presence of TM-N catalytic sites makes such processes thermodynamically favorable where their fast kinetics are maintained for both FeN₂ ($E_r = -0.13$ eV, $E_a = 0.53$ eV) and CoN₂ ($E_r = -0.44$ eV, $E_a = 0.52$ eV) systems. Overall, it is suggested by our computational study that the TM-N doping not only suppresses the shuttle effect by increasing the adsorption strength of LiPSs and the substrate but also facilitates small-LiPS decomposition by improving their thermodynamics and kinetics properties. Therefore, the TM-N-co-doped GDY can be considered potential electrode materials for Li-S batteries.

■ ASSOCIATED CONTENT

Supporting Information

The Supporting Information is available free of charge at <https://pubs.acs.org/doi/10.1021/acsaem.2c01395>.

Detailed results of possible configurations and charge distribution of the doped GDY substrates (Section S1); calculation of thermal stability using AIMD simulation (Section S2); electronic band structures of substrates using DFT-PBE calculation (Section S3); projected density of state of the substrates using DFT calculation with GGA + U (Section S4); molecular structure of S₈ and LiPS species before and after adsorption (Section S5); Bader charge analysis upon adsorption (Section S6); partial density of state of Li and N for LiPSs adsorbed co-doped GDY (Section S7); co-adsorption systems of Li₂S₆ in the presence of solvent molecules (Section S8); catalytic decomposition of Li₂S₂ and Li₂S for other reaction paths (Section S9); and diffusion of Li ion on GDY monolayer (Section S10) (PDF)

■ AUTHOR INFORMATION

Corresponding Authors

Pussana Hirunsit – National Nanotechnology Center (NANOTEC), National Science and Technology Development Agency (NSTDA), Pathum Thani 12120, Thailand; orcid.org/0000-0003-1309-7553; Email: pussana.hirunsit@gmail.com

Suwit Suthirakum – School of Chemistry, Institute of Science, Suranaree University of Technology, Nakhon Ratchasima 30000, Thailand; orcid.org/0000-0002-6590-6343; Email: suthirak@sut.ac.th

Authors

Sirisak Singesen – Center of Excellence in Advanced Functional Materials, School of Physics, Suranaree University of Technology, Nakhon Ratchasima 30000, Thailand; Thailand Center of Excellence in Physics, Commission on the Higher Education, Bangkok 10400, Thailand

Ittipon Fongkaew – Center of Excellence in Advanced Functional Materials, School of Physics, Suranaree University of Technology, Nakhon Ratchasima 30000, Thailand; Thailand Center of Excellence in Physics, Commission on the Higher Education, Bangkok 10400, Thailand

Complete contact information is available at: <https://pubs.acs.org/doi/10.1021/acsaem.2c01395>

Notes

The authors declare no competing financial interest.

ACKNOWLEDGMENTS

This research was funded by Suranaree University of Technology (SUT), National Research Council of Thailand (NRCT) (grant nos. N42A6S0325 and M6300470-3/2565), Thailand Science Research and Innovation (TSRI), and National Science, Research and Innovation Fund (NSRF) (160363). The authors thank NSTDA Supercomputer Center (ThaiSC) and Institute of Science, Suranaree University of Technology, for the computational resources.

REFERENCES

- Braun, P. V.; Cho, J.; Pikul, J. H.; King, W. P.; Zhang, H. High Power Rechargeable Batteries. *Curr. Opin. Solid State Mater. Sci.* **2012**, *16*, 186–198.
- Bruce, P. G.; Freunberger, S. A.; Hardwick, L. J.; Tarascon, J.-M. Li–O₂ and Li–S Batteries with High Energy Storage. *Nat. Mater.* **2012**, *11*, 19–29.
- Manthiram, A.; Chung, S.-H.; Zu, C. Lithium–Sulfur Batteries: Progress and Prospects. *Adv. Mater.* **2015**, *27*, 1980–2006.
- Manthiram, A.; Fu, Y.; Chung, S.-H.; Zu, C.; Su, Y.-S. Rechargeable Lithium–Sulfur Batteries. *Chem. Rev.* **2014**, *114*, 11751–11787.
- Yin, Y.-X.; Xin, S.; Guo, Y.-G.; Wan, L.-J. Lithium–Sulfur Batteries: Electrochemistry, Materials, and Prospects. *Angew. Chem., Int. Ed.* **2013**, *52*, 13186–13200.
- Ji, X.; Lee, K. T.; Nazar, L. F. A Highly Ordered Nanostructured Carbon–Sulphur Cathode for Lithium–Sulphur Batteries. *Nat. Mater.* **2009**, *8*, 500–506.
- Ma, L.; Hendrickson, K. E.; Wei, S.; Archer, L. A. Nanomaterials: Science and Applications in the Lithium–Sulfur Battery. *Nano Today* **2015**, *10*, 315–338.
- Barghamadi, M.; Kapoor, A.; Wen, C. A Review on Li–S Batteries as a High Efficiency Rechargeable Lithium Battery. *J. Electrochem. Soc.* **2013**, *160*, A1256–A1263.
- Canfield, D. E. Biogeochemistry of Sulfur Isotopes. *Rev. Mineral. Geochem.* **2001**, *43*, 607–636.
- Barchasz, C.; Molton, F.; Duboc, C.; Leprêtre, J.-C.; Patoux, S.; Alloin, F. Lithium/Sulfur Cell Discharge Mechanism: An Original Approach for Intermediate Species Identification. *Anal. Chem.* **2012**, *84*, 3973–3980.
- Moy, D.; Manivannan, A.; Narayanan, S. R. Direct Measurement of Polysulfide Shuttle Current: A Window into Understanding the Performance of Lithium–Sulfur Cells. *J. Electrochem. Soc.* **2015**, *162*, A1–A7.
- Assary, R. S.; Curtiss, L. A.; Moore, J. S. Toward a Molecular Understanding of Energetics in Li–S Batteries Using Nonaqueous Electrolytes: A High-Level Quantum Chemical Study. *J. Phys. Chem. C* **2014**, *118*, 11545–11558.
- Mikhaylik, Y. V.; Akridge, J. R. Polysulfide Shuttle Study in the Li/S Battery System. *J. Electrochem. Soc.* **2004**, *151*, A1969.
- Bresser, D.; Passerini, S.; Scrosati, B. Recent Progress and Remaining Challenges in Sulfur-Based Lithium Secondary Batteries – a Review. *Chem. Commun.* **2013**, *49*, 10545–10562.
- Huang, J.-Q.; Zhang, Q.; Wei, F. Multi-Functional Separator/Interlayer System for High-Stable Lithium–Sulfur Batteries: Progress and Prospects. *Energy Storage Mater.* **2015**, *1*, 127–145.
- Eftekhari, A.; Kim, D.-W. Cathode Materials for Lithium–Sulfur Batteries: A Practical Perspective. *J. Mater. Chem. A* **2017**, *5*, 17734–17776.
- Li, H.; Sun, M.; Zhang, T.; Fang, Y.; Wang, G. Improving the Performance of PEDOT-PSS Coated Sulfur@activated Porous Graphene Composite Cathodes for Lithium–Sulfur Batteries. *J. Mater. Chem. A* **2014**, *2*, 18345–18352.
- Xi, K.; Chen, B.; Li, H.; Xie, R.; Gao, C.; Zhang, C.; Kumar, R. V.; Robertson, J. Soluble Polysulfide Sorption Using Carbon Nanotube Forest for Enhancing Cycle Performance in a Lithium–Sulphur Battery. *Nano Energy* **2015**, *12*, 538–546.
- Xie, Y.; Meng, Z.; Cai, T.; Han, W.-Q. Effect of Boron-Doping on the Graphene Aerogel Used as Cathode for the Lithium–Sulfur Battery. *ACS Appl. Mater. Interfaces* **2015**, *7*, 25202–25210.
- Liu, S.; Li, Y.; Hong, X.; Xu, J.; Zheng, C.; Xie, K. Reduced Graphene Oxide–Hollow Carbon Sphere Nanostructure Cathode Material with Ultra-High Sulfur Content for High Performance Lithium–Sulfur Batteries. *Electrochim. Acta* **2016**, *188*, 516–522.
- Ma, X. Z.; Jin, B.; Xin, P. M.; Wang, H. H. Multiwalled Carbon Nanotubes–Sulfur Composites with Enhanced Electrochemical Performance for Lithium/Sulfur Batteries. *Appl. Surf. Sci.* **2014**, *307*, 346–350.
- Sun, L.; Kong, W.; Jiang, Y.; Wu, H.; Jiang, K.; Wang, J.; Fan, S. Super-Aligned Carbon Nanotube/Graphene Hybrid Materials as a Framework for Sulfur Cathodes in High Performance Lithium Sulfur Batteries. *J. Mater. Chem. A* **2015**, *3*, 5305–5312.
- Zhao, C.; Liu, L.; Zhao, H.; Krall, A.; Wen, Z.; Chen, J.; Hurley, P.; Jiang, J.; Li, Y. Sulfur-Infiltrated Porous Carbon Microspheres with Controllable Multi-Modal Pore Size Distribution for High Energy Lithium–Sulfur Batteries. *Nanoscale* **2014**, *6*, 882–888.
- Huang, J.-Q.; Xu, Z.-L.; Abouali, S.; Akbari Garakani, M.; Kim, J.-K. Porous Graphene Oxide/Carbon Nanotube Hybrid Films as Interlayer for Lithium–Sulfur Batteries. *Carbon* **2016**, *99*, 624–632.
- Wang, F.; Zuo, Z.; Li, L.; He, F.; Li, Y. Graphdiyne Nanostructure for High-Performance Lithium–Sulfur Batteries. *Nano Energy* **2020**, *68*, No. 104307.
- Kong, S.; Cai, D.; Li, G.; Xu, X.; Zhou, S.; Ding, X.; Zhang, Y.; Yang, S.; Zhou, X.; Nie, H.; Huang, S.; Peng, P.; Yang, Z. Hydrogen-Substituted Graphdiyne/Graphene as an Sp/Sp² Hybridized Carbon Interlayer for Lithium–Sulfur Batteries. *Nanoscale* **2021**, *13*, 3817–3826.
- Wang, J.; Wang, K.; Yang, Z.; Li, X.; Gao, J.; He, J.; Wang, N.; Wang, H.; Zhang, Y.; Huang, C. Effective Stabilization of Long-Cycle Lithium–Sulfur Batteries Utilizing In Situ Prepared Graphdiyne-Modulated Separators. *ACS Sustainable Chem. Eng.* **2020**, *8*, 1741–1750.
- Baughman, R. H.; Eckhardt, H.; Kertesz, M. Structure-property Predictions for New Planar Forms of Carbon: Layered Phases Containing Sp² and Sp Atoms. *J. Chem. Phys.* **1987**, *87*, 6687–6699.
- Long, M.; Tang, L.; Wang, D.; Li, Y.; Shuai, Z. Electronic Structure and Carrier Mobility in Graphdiyne Sheet and Nanoribbons: Theoretical Predictions. *ACS Nano* **2011**, *5*, 2593–2600.
- Yu, H.; Xue, Y.; Li, Y. Graphdiyne and Its Assembly Architectures: Synthesis, Functionalization, and Applications. *Adv. Mater.* **2019**, *31*, No. 1803101.
- Du, H.; Zhang, Z.; He, J.; Cui, Z.; Chai, J.; Ma, J.; Yang, Z.; Huang, C.; Cui, G. A Delicately Designed Sulfide Graphdiyne Compatible Cathode for High-Performance Lithium/Magnesium–Sulfur Batteries. *Small* **2017**, *13*, No. 1702277.
- Cai, Y. The Anchoring Effect of 2D Graphdiyne Materials for Lithium–Sulfur Batteries. *ACS Omega* **2020**, *5*, 13424–13429.
- Muhammad, I.; Younis, U.; Xie, H.; Kawazoe, Y.; Sun, Q. Graphdiyne-Based Monolayers as Promising Anchoring Materials for Lithium–Sulfur Batteries: A Theoretical Study. *Adv. Theory Simul.* **2020**, *3*, No. 1900236.
- Wang, X.; Yang, Z.; Si, W.; Shen, X.; Li, X.; Li, R.; Lv, Q.; Wang, N.; Huang, C. Cobalt-Nitrogen-Doped Graphdiyne as an Efficient Bifunctional Catalyst for Oxygen Reduction and Hydrogen Evolution Reactions. *Carbon* **2019**, *147*, 9–18.
- Si, W.; Yang, Z.; Wang, X.; Lv, Q.; Zhao, F.; Li, X.; He, J.; Long, Y.; Gao, J.; Huang, C. Fe,N-Codoped Graphdiyne Displaying Efficient Oxygen Reduction Reaction Activity. *ChemSusChem* **2019**, *12*, 173–178.
- Lin, H.; Jin, R.; Wang, A.; Zhu, S.; Li, H. Transition Metal Embedded C₂N with Efficient Polysulfide Immobilization and

- Catalytic Oxidation for Advanced Lithium-Sulfur Batteries: A First Principles Study. *Ceram. Int.* **2019**, *45*, 17996–18002.
- (37) Zhang, L.; Liang, P.; Shu, H. B.; Man, X. L.; Du, X. Q.; Chao, D. L.; Liu, Z. G.; Sun, Y. P.; Wan, H. Z.; Wang, H. Design Rules of Heteroatom-Doped Graphene to Achieve High Performance Lithium-Sulfur Batteries: Both Strong Anchoring and Catalysing Based on First Principles Calculation. *J. Colloid Interface Sci.* **2018**, *529*, 426–431.
- (38) Zeng, Q.-W.; Hu, R.-M.; Chen, Z.-B.; Shang, J.-X. Single-Atom Fe and N Co-Doped Graphene for Lithium-Sulfur Batteries: A Density Functional Theory Study. *Mater. Res. Express* **2019**, *6*, No. 095620.
- (39) Kresse, G.; Furthmüller, J. Efficient Iterative Schemes for Ab Initio Total-Energy Calculations Using a Plane-Wave Basis Set. *Phys. Rev. B* **1996**, *54*, 11169–11186.
- (40) Kresse, G.; Furthmüller, J. Efficiency of Ab-Initio Total Energy Calculations for Metals and Semiconductors Using a Plane-Wave Basis Set. *Comput. Mater. Sci.* **1996**, *6*, 15–50.
- (41) Blöchl, P. E. Projector Augmented-Wave Method. *Phys. Rev. B* **1994**, *50*, 17953–17979.
- (42) Perdew, J. P.; Burke, K.; Ernzerhof, M. Generalized Gradient Approximation Made Simple. *Phys. Rev. Lett.* **1996**, *77*, 3865–3868.
- (43) Grimme, S.; Antony, J.; Ehrlich, S.; Krieg, H. A Consistent and Accurate Ab Initio Parametrization of Density Functional Dispersion Correction (DFT-D) for the 94 Elements H-Pu. *J. Chem. Phys.* **2010**, *132*, No. 154104.
- (44) Grimme, S.; Ehrlich, S.; Goerigk, L. Effect of the Damping Function in Dispersion Corrected Density Functional Theory. *J. Comput. Chem.* **2011**, *32*, 1456–1465.
- (45) Monkhorst, H. J.; Pack, J. D. Special Points for Brillouin-Zone Integrations. *Phys. Rev. B* **1976**, *13*, 5188–5192.
- (46) Tang, W.; Sanville, E.; Henkelman, G. A Grid-Based Bader Analysis Algorithm without Lattice Bias. *J. Phys. Condens. Matter* **2009**, *21*, No. 084204.
- (47) Li, G.; Li, Y.; Liu, H.; Guo, Y.; Li, Y.; Zhu, D. Architecture of Graphdiyne Nanoscale Films. *Chem. Commun.* **2010**, *46*, 3256–3258.
- (48) Pei, Y. Mechanical Properties of Graphdiyne Sheet. *Phys. B Condens. Matter* **2012**, *407*, 4436–4439.
- (49) Singen, S.; Tangpakonsab, P.; Tussamee, N.; Kaewmaraya, T. First-Principles Calculation for Water Purification of Pb, Sn and Zn Ions Adsorption on Graphdiyne Surface. *J. Phys. Conf. Ser.* **2021**, *1719*, No. 012028.
- (50) Tan, X.; Shao, H.; Hu, T.; Liu, G.; Jiang, J.; Jiang, H. High Thermoelectric Performance in Two-Dimensional Graphyne Sheets Predicted by First-Principles Calculations. *Phys. Chem. Chem. Phys.* **2015**, *17*, 22872–22881.
- (51) Ketabi, N.; Tolhurst, T. M.; Leedahl, B.; Liu, H.; Li, Y.; Moewes, A. How Functional Groups Change the Electronic Structure of Graphdiyne: Theory and Experiment. *Carbon* **2017**, *123*, 1–6.
- (52) He, J.; Ma, S. Y.; Zhou, P.; Zhang, C. X.; He, C.; Sun, L. Z. Magnetic Properties of Single Transition-Metal Atom Adsorbed Graphdiyne and Graphyne Sheet from DFT+U Calculations. *J. Phys. Chem. C* **2012**, *116*, 26313–26321.
- (53) Chen, J.-J.; Yuan, R.-M.; Feng, J.-M.; Zhang, Q.; Huang, J.-X.; Fu, G.; Zheng, M.-S.; Ren, B.; Dong, Q.-F. Conductive Lewis Base Matrix to Recover the Missing Link of Li₂S₈ during the Sulfur Redox Cycle in Li-S Battery. *Chem. Mater.* **2015**, *27*, 2048–2055.
- (54) Wang, Y.; Shen, J.; Xu, L.-C.; Yang, Z.; Li, R.; Liu, R.; Li, X. Sulfur-Functionalized Vanadium Carbide MXene (V₂CS₂) as a Promising Anchoring Material for Lithium-Sulfur Batteries. *Phys. Chem. Chem. Phys.* **2019**, *21*, 18559–18568.
- (55) Hofmann, A. F.; Fronczek, D. N.; Bessler, W. G. Mechanistic Modeling of Polysulfide Shuttle and Capacity Loss in Lithium-Sulfur Batteries. *J. Power Sources* **2014**, *259*, 300–310.
- (56) Xu, N.; Qian, T.; Liu, X.; Liu, J.; Chen, Y.; Yan, C. Greatly Suppressed Shuttle Effect for Improved Lithium Sulfur Battery Performance through Short Chain Intermediates. *Nano Lett.* **2017**, *17*, 538–543.
- (57) Liu, M.; Li, Q.; Qin, X.; Liang, G.; Han, W.; Zhou, D.; He, Y.-B.; Li, B.; Kang, F. Suppressing Self-Discharge and Shuttle Effect of Lithium-Sulfur Batteries with V₂O₅-Decorated Carbon Nanofiber Interlayer. *Small* **2017**, *13*, No. 1602539.
- (58) Zhang, Q.; Wang, Y.; Seh, Z. W.; Fu, Z.; Zhang, R.; Cui, Y. Understanding the Anchoring Effect of Two-Dimensional Layered Materials for Lithium-Sulfur Batteries. *Nano Lett.* **2015**, *15*, 3780–3786.
- (59) Scheers, J.; Fantini, S.; Johansson, P. A Review of Electrolytes for Lithium-Sulphur Batteries. *J. Power Sources* **2014**, *255*, 204–218.
- (60) Choi, J.-W.; Cheruvally, G.; Kim, D.-S.; Ahn, J.-H.; Kim, K.-W.; Ahn, H.-J. Rechargeable Lithium/Sulfur Battery with Liquid Electrolytes Containing Toluene as Additive. *J. Power Sources* **2008**, *183*, 441–445.
- (61) Kim, S.; Jung, Y.; Lim, H. S. The Effect of Solvent Component on the Discharge Performance of Lithium-Sulfur Cell Containing Various Organic Electrolytes. *Electrochim. Acta* **2004**, *50*, 889–892.
- (62) Kamphaus, E. P.; Balbuena, P. B. Long-Chain Polysulfide Retention at the Cathode of Li-S Batteries. *J. Phys. Chem. C* **2016**, *120*, 4296–4305.
- (63) Song, M.-K.; Zhang, Y.; Cairns, E. J. A Long-Life, High-Rate Lithium/Sulfur Cell: A Multifaceted Approach to Enhancing Cell Performance. *Nano Lett.* **2013**, *13*, 5891–5899.
- (64) Zhou, G.; Yang, A.; Gao, G.; Yu, X.; Xu, J.; Liu, C.; Ye, Y.; Pei, A.; Wu, Y.; Peng, Y.; Li, Y.; Liang, Z.; Liu, K.; Wang, L.-W.; Cui, Y. Supercooled Liquid Sulfur Maintained in Three-Dimensional Current Collector for High-Performance Li-S Batteries. *Sci. Adv.* **2020**, *6*, No. eaay5098.
- (65) Zhou, G.; Tian, H.; Jin, Y.; Tao, X.; Liu, B.; Zhang, R.; Seh, Z. W.; Zhuo, D.; Liu, Y.; Sun, J.; Zhao, J.; Zu, C.; Wu, D. S.; Zhang, Q.; Cui, Y. Catalytic Oxidation of Li-Sub>2</Sub>S on the Surface of Metal Sulfides for Li-S Batteries. *Proc. Natl. Acad. Sci.* **2017**, *114*, 840–845.
- (66) Wang, B.; Li, K.; Su, D.; Ahn, H.; Wang, G. Superior Electrochemical Performance of Sulfur/Graphene Nanocomposite Material for High-Capacity Lithium-Sulfur Batteries. *Chem. – An Asian J.* **2012**, *7*, 1637–1643.
- (67) Liu, X.; Shao, X.; Li, F.; Zhao, M. Anchoring Effects of S-Terminated Ti₂C MXene for Lithium-Sulfur Batteries: A First-Principles Study. *Appl. Surf. Sci.* **2018**, *455*, 522–526.
- (68) Zhang, H.; Xia, Y.; Bu, H.; Wang, X.; Zhang, M.; Luo, Y.; Zhao, M. Graphdiyne: A Promising Anode Material for Lithium Ion Batteries with High Capacity and Rate Capability. *J. Appl. Phys.* **2013**, *113*, No. 044309.
- (69) Sun, C.; Searles, D. J. Lithium Storage on Graphdiyne Predicted by DFT Calculations. *J. Phys. Chem. C* **2012**, *116*, 26222–26226.
- (70) Yang, Y.; Zheng, G.; Misra, S.; Nelson, J.; Toney, M. F.; Cui, Y. High-Capacity Micrometer-Sized Li₂S Particles as Cathode Materials for Advanced Rechargeable Lithium-Ion Batteries. *J. Am. Chem. Soc.* **2012**, *134*, 15387–15394.

Abstract submitted in The 25th International Annual Symposium on Computational Science and Engineering 2022 (ANSCSE25)

PFD-O-3

TRANSITION METAL AND NITROGEN CO-DOPED GRAPHDIYNE AS ANCHORING MATERIALS IN LITHIUM-SULFUR BATTERIES: A FIRST-PRINCIPLES STUDY

Sirisak Singesen¹, Ittipon Fongkaew¹, Pussana Hirunsit^{2,*}, and Suwit Suthirakun^{3,*}

¹*School of Physics, Institute of Science, Suranaree University of Technology, Nakhon Ratchasima, Thailand 30000*

²*National Nanotechnology Center (NANOTEC), National Science and Technology Development Agency (NSTDA), Pathum Thani, Thailand 12120*

³*School of Chemistry, Institute of Science, Suranaree University of Technology, Nakhon Ratchasima, Thailand 30000*

*(E-mail: suthirak@sut.ac.th (S.S.), pussana.hirunsit@gmail.com (P.H.))

Lithium-sulfur (Li-S) batteries are among the next generation of rechargeable energy storage technologies due to their high theoretical specific capacity and energy density. However, critical problems inhibit their commercialization, including the shuttle effect of lithium polysulfide (LiPS) and the difficult kinetics of phase transformation during charge/discharge process. A search for novel host cathode materials has challenged to improve these problems. In this work, density functional theory and *ab initio* molecular dynamic simulations were employed to explore the role of transition metal and nitrogen-doped graphdiyne (TMN₂@GDY, TM = Co or Fe) as a cathode material in Li-S batteries. Our computations reveal that TM and N doping induces the change of electronic structures of GDY host from semiconductor to metallic. The shuttle effect is efficiently suppressed owing to strong chemical interaction between LiPS and the doped substrates with the TM-N anchoring. The electronic structures of GDY host are still metallic upon LiPS adsorption, resulting in high acceleration to redox reaction. The dynamic simulations suggest that LiPS molecules are easily dissoluble in solvents due to chemical binding between soluble LiPS and electrolyte molecules. Moreover, the analysis of catalytic LiPS decomposition reveals that both CoN₂@GDY and FeN₂@GDY reduce the dissociation energy barrier during charging, which promotes fast phase transformation. Overall, our results suggest that the co-doped GDY is an efficient anchoring cathode in Li-S batteries.

Keyword: lithium-sulfur batteries; graphdiyne; density functional theory; first-principles method; polysulfide solubility

Abstract submitted in The 9th Annual Research Chemical Engineering Graduate
Student Association Symposium (ChEGSA9)

The 9th Annual Research Chemical Engineering Graduate Student Association Symposium (ChEGSA9)

**Transition metal and nitrogen co-doped graphdiyne as a single-atom catalyst
to achieve strong anchoring effect in lithium-sulfur batteries**

Sirisak Singesen[†], Ittipon Fongkaew[†], Pussana Hirunsit^{‡,*1}, Suwit Suthirakun^{#,*2}

[†]School of Physics, Institute of Science, Suranaree University of Technology, Nakhon Ratchasima, Thailand 30000

[‡]National Nanotechnology Center (NANOTEC), National Science and Technology Development Agency (NSTDA), 111 Thailand Science Park, Pathum Thani, Thailand 12120

[#]School of Chemistry, Institute of Science, Suranaree University of Technology, Nakhon Ratchasima, Thailand 30000

*¹E-mail: pussana@nanotec.or.th, *²E-mail: suthirak@sut.ac.th

Abstract

Lithium-sulfur (Li-S) batteries are among the next generation of rechargeable energy storage technologies because of their high theoretical specific capacity and energy density. However, the critical problems inhibit their commercialization, including the shuttle effect of lithium polysulfide (LiPS) and the difficult kinetics of phase transformation during charge/discharge process. A search of novel host cathode materials has challenged to improve these problems. In this work, density functional theory and ab initio molecular dynamic simulations were employed to explore the role of transition metal and nitrogen-doped graphdiyne (TMN₂@GDY, TM = Co or Fe) as a cathode material in Li-S batteries. Our computations reveal that the presence of TM and N doping induces the change of electronic structures of GDY host from semiconductor to metallic. The shuttle effect is efficiently suppressed owing to strong chemical interaction between LiPS and the doped substrates, due to the TM-N anchoring effect. The electronic structures of GDY host are still metallic upon LiPS adsorption, resulting in high acceleration to redox reaction. The dynamic simulations suggest that LiPS molecules are easily dissoluble in solvents due to chemical binding between soluble LiPS and electrolyte molecules. Moreover, the analysis of catalytic LiPS decomposition reveals that both CoN₂@GDY and FeN₂@GDY reduce the dissociation energy barrier during discharging, which promotes fast phase transformation. Overall, our results may suggest the co-doped GDY with the synergistic role of TM-N dopants as an anchoring cathode in Li-S batteries.

Keyword: lithium-sulfur batteries, graphdiyne, density functional theory, first principles method, polysulfide solubility

CURRICULUM VITAE

Sirisak Singesen was born on October 10th, 1997 in Si Sa Ket, Thailand. He received his B.Sc. in Physics (first-class honors) in 2020 from the Department of Physics, Faculty of Science, Khon Kaen University, Thailand. He has granted the scholarship from the Development and Promotion of Science and Technology Talents Project (DPST, THAILAND) since 2017. During his senior year in bachelor's degree, he started research in condensed matter physics dealing with density functional theory under the supervision of Assoc. Prof. Dr. Thanayut Kaewmaraya. In 2021, he continued to pursue the master's degree program in the School of Physics, Suranaree University of Technology, Thailand with DPST scholarship and National Research and Innovation Information System (NRIIS, THAILAND) under the supervision of Asst. Prof. Dr. Suwit Suthirakun and Dr. Ittipon Fongkeaw. In 2022, He was a research scholar at Chemical Engineering Department, Texas A&M University (TAMU), USA with DPST and TAMU sponsor funds under the supervision of Prof. Dr. Perla B. Balbuena. He has published articles in international journals and participated in the international conferences (listed in APPENDIX B) during the course of his master program.

มหาวิทยาลัยเทคโนโลยีสุรนารี